2D3V Particle-in-cell simulations of Electron Cyclotron Drift Instability and anomalous electron transport in E × B plasmas

A Thesis Submitted to the
College of Graduate and Postdoctoral Studies
in Partial Fulfillment of the Requirements
for the degree of Master of Science
in the Department of Physics & Engineering Physics
University of Saskatchewan
Saskatoon

By
Marilyn Jimenez

Permission to Use

In presenting this thesis in partial fulfillment of the requirements for a Postgraduate degree from the University of Saskatchewan, I agree that the Libraries of this University may make it freely available for inspection. I further agree that permission for copying of this thesis in any manner, in whole or in part, for scholarly purposes may be granted by the professor or professors who supervised my thesis work or, in their absence, by the Head of the Department or the Dean of the College in which my thesis work was done. It is understood that any copying or publication or use of this thesis or parts thereof for financial gain shall not be allowed without my written permission. It is also understood that due recognition shall be given to me and to the University of Saskatchewan in any scholarly use which may be made of any material in my thesis.

Requests for permission to copy or to make other use of material in this thesis in whole or part should be addressed to:

Head of the Department of Computer Science
176 Thorvaldson Building
110 Science Place
University of Saskatchewan
Saskatoon, Saskatchewan
Canada
S7N 5C9

Or

Dean
College of Graduate and Postdoctoral Studies
University of Saskatchewan
116 Thorvaldson Building, 110 Science Place
Saskatoon, Saskatchewan S7N 5C9
Canada

Abstract

This thesis is devoted to nonlinear physics of plasmas investigated with kinetic modeling. The emphasis is on the characterization of waves, instabilities, and anomalous electron transport. The main topic is related to partially magnetized plasmas immersed in crossed $\mathrm{E}\times\mathrm{B}$ fields with magnetized electrons and unmagnetized ions. Such plasmas are abundant in many applications such as Hall thrusters devices for space propulsion and material processing. The nonlinear evolution of the Electron Cyclotron Drift Instability (ECDI) driven by the electron $\mathrm{E}\times\mathrm{B}$ drift in partially magnetized plasmas and anomalous electron transport in two dimensions are studied using particle-in-cell (PIC) simulations. PIC simulations were performed for the parameters typical of the Hall-effect thruster in two-dimensional azimuthal-radial geometry to investigate the role of the boundaries conditions, electric and magnetic field magnitudes, sheath losses and finite-length on the mode development and anomalous electron current. The turbulence and the induced anomalous electron current are studied. Nature of the anomalous current and contribution of different wavelength are investigated. It is shown that the magnitude of the anomalous current can be explained as a $\mathrm{E}\times\mathrm{B}$ drift of magnetized electrons in fluctuating fields. The same PIC code was used for a benchmark project in simulations of a similar radial-azimuthal configuration of a Hall thruster. Seven different groups using independently developed codes were able to capture the same physics, both for ECDI and Modified Two-Stream Instability (MTSI) modes. An additional study related to the role of noise in kinetic plasma simulations is presented. It confirmed that statistical particle noise could distort some Buneman-type instabilities to be identified in the linear regime.

Acknowledgements

I would like to thank members of my Advisory Committee: Prof. Michael Bradley, Prof. Chijin Xiao, Prof. John Tse, and external exterminator Prof. Alexey Shevyakov for the guidance and suggestions during my Master studies. I want to thank Dr. Salomon Janhunen and Dr. Dmytro Sydorenko for initial guidance and advice with numerical implementations; to my supervisor Prof. Andrei Smolyakov for giving me the opportunity to study in the University of Saskatchewan. I also greatly appreciate the contributions of my friends and colleagues, Nathan Nelson and Andy Sabo. Special thanks to Oleksandr Chapurin for all his support and fruitful discussions.

Finally, I want to express all my gratitude to my God, Jesus Christ, and my family, without whom I wouldn't be.

Dedication

I dedicate this thesis first to God, Jesus Christ the center of my life, and to my family. They are my constant source of strength and wisdom, my motivation and to whom I owe success in my life.

Contents

List of Tables

List of Figures

1 Introduction

1.1 Introduction to plasma and general definitions

Plasma is a quasineutral gas of charged particles which move in self-consistent electric and magnetic fields. The electromagnetic interaction among the charged particles defines the plasma's behavior that is governed by collective effects. The potential energy of particles interacting locally is lower than their kinetic energy [1]. Thus, the equation of state of gas (of charged particles) can still be considered as an ideal gas. A sufficiently large plasma volume can be characterized by local plasma parameters such as density and temperature [2]. An important condition (criterion) for plasma state is defined as macroscopic neutrality and quasi-neutrality, which is related to the Debye shielding.

The macroscopic neutrality means that under equilibrium conditions, the net (total) electric charge is zero. Locally plasma remains neutral on length scales larger than the Debye length (quasineutrality). This length is the distance over which the electric field of an individual charged particle is felt by the other charged particles inside the plasma, and which is given by:

$$\lambda_{De} = \sqrt{\frac{\varepsilon_0 k_B T_e}{n_e q_e^2}}, \tag{1.1}$$

where subscript e denote electron specie, ε_0 is the vacuum permittivity, n_e is particle density, q_e is the particle charge, T_e is the temperature, and k_B the Boltzmann constant. The plasma frequency is a natural frequency of electrostatic oscillations that characterizes the collective motion of charged particles within the plasma due to an instantaneous disturbance from the equilibrium condition. The electron plasma frequency is defined by:

$$\omega_{pe} = \sqrt{\frac{n_e q_e^2}{m_e \varepsilon_0}}, \tag{1.2}$$

where m_e is the mass of the electron particle. On average, over times longer than $2\pi/\omega_{pe}$, the plasma is neutral. Hence, quasineutrality is the absence of charge and electric fields on large length scale system $L > \lambda_{De}$, and on long time scales, $T > 2\pi/\omega_{pe}$. Similarly, the ion dynamics has a characteristic frequency of $\omega_{pi} = \sqrt{n_i q_e^2/m_i \varepsilon_0}$. The ions move only ω_{pi} length scale. Consequently, the relation between ion and electron plasma frequency is $\sqrt{m_e/m_i}$ for the two plasma components. Accordingly, there is a large time scale separations (typically few orders) which may lead to computational difficulties in simulations. Among the two main types of plasma models, fully fluid and fully kinetic models, one can construct a hybrid method, that may be used to alleviate the problem of distinct time scales.

The fluid simulations describe the system by solving numerically the fluid equations of plasma, while the kinetic simulation models involve detailed particle descriptions (statistically, using the distribution func-

tion); both approaches use a self-consistent electromagnetic field. Hybrid simulations, in the simplest case, merge the two approaches mentioned above to represent each species. Hybrid fluid-kinetic plasma simulations allow a wider range of plasma conditions. For instance, if we are more interested in modeling the ion dynamics (low-frequency dynamics), one can use particle-in-cell method (PIC), which is a kinetic method, to simulate ion species and a fluid approach to simulate electrons. Often, for simplicity, electron dynamics can be approximated with the Boltzmann density distribution. Thus, the hybrid approach gives us a coupling of fluid and kinetic modeling techniques.

An important consideration when developing a computer code is using an appropiate description of the kinematics of a continuum. Two classical descriptions of motion are the Lagrangian description, also called the "particle based approach", and the Eulerian description "field approach". In the Lagrangian approach where the individual particles are tracked, we typically have to utilize a lot of computational resources. The Lagrangian step describes time-continuous equations of motion for the particles. The advantages include relatively simple equations of motion of individual particles and the independence of the other particles motion dynamics. In the Eulerian approach, we seek the evolution of plasma quantities in a fixed spatial position, this is a fluid passes through that fixed point in space. This description allows the fields to be calculated on stationary grid points using Maxwell equations. The combination of the Lagrangian step and the Eulerian step particle motion is an advantage of the PIC method. Lagrangian and Eulerian approaches exist in pure fluid models as well. For a quantitative analysis of a large number of particles in a system, such as in plasma, it is common to use a statistical method. The plasma kinetic theory takes into account the motion of all particles. The Klimontovich equation together with Maxwell's equations gives an exact description of plasma [1] which could be difficult to solve for a realistic plasma setup. In plasma physics one of the most important equation is the Vlasov equation, that arises from the Klimontovich equation, by averaging over a small space volume, assuming it contains large number of particles so the distribution function is introduced. The particle distribution function that defines the system evolution (kinetic method) evolves according to the Vlasov equation (or Boltzmann equation, when collision operator is included).
The thesis is structured as follows: the study will begin with an introduction of relevant plasma devices description, and a general kinetic characterization of plasmas. In this work, plasma studies (simulations and theory) are based on a kinetic approach. The purpose of this thesis is to analyze a possible candidate for the anomalous electron transport (higher than predicted by classical theory) in a Hall thruster device, using a numerical tool, a 2D3V PIC code. This code was written by D. Sydorenko. I participated in initial tests of various code subroutines, and then used the code for physics studies described in Chapters 4-5. Experiments show this anomalous transport with values to be orders of magnitude larger than those that classical (collisional) theory predicts. Introduction ends with a classification of plasma waves and instabilities in plasma. Thus in Chapter 2, the derivation and a more detailed explanation of some instabilities, such as the Electron Cyclotron Drift Instability (ECDI) and ion-sound modes are presented. In Chapter 3, a brief description of the 2D3V PIC code I used to model and investigate the correlation between the electron

anomalous transport and the ECDI development for the configuration of the Hall thruster. All my results suggest a possible answer to the question on study: What can be a possible source for the electron anomalous transport? Chapter 4. shows a comprehensive study with various simulations cases where plasma parameters and/or boundary conditions were changed. All of them confirm that there exist a strong correlation between the observed electron anomalous transport and the current induced by the fluctuating electric field (evolved from the nonlinear ECDI development). For all plasma simulations the nonlinear evolution of the ECDI and anomalous transport are shown. At the end of Chapter 4 the results from the scaling study are given. Finally, two different benchmark projects are reviewed. Chapter 5 describes the benchmark project I was involved, were the results were compared between seven plasma simulations groups. This work is related to the nonlinear coupling of ECDI and the Modified Two-Stream Instability (MTSI) for a similar Hall thruster configuration as in Chapter 4. Additionally, a second benchmark project conducted in our research group about the significance of noise in PIC simulations is presented in Chapter 6.

1.2 Plasma devices: Hall thruster and sputtering magnetron

Among various plasma devices, Hall thruster and magnetron exhibit similar fluctuations and anomalous transport. Thus, despite very different applications, Hall thruster in some ways has similar physics to a planar magnetron discharge. They are based on the same physical phenomena of maintaining a large electric field by using a magnetic field. Hall thrusters are competitive electric propulsion plasma devices for spacecraft missions, while, magnetron discharges are used for industrial applications as a deposition technology. In a Hall thruster and sputtering magnetron the applied axial electric field $\mathbf{E}$ is orthogonal to the radial magnetic field $\mathbf{B}$. Typical value of the magnetic field is large enough to confined the electrons but not ions (its gyroradius is larger than the system size). It leads to a high azimuthal drift for the electrons. Thus, these conditions permit efficient thrust and sputtering operations for the respective devices [3]. Magnetron sputtering is a process that involves a cascade of collisions between the incident particles and the target surface (material), see Fig. 1.1a. This collision cascade process with the target is due to a high negative voltage applied between the anode and cathode together with a magnetic field applied behind the target surface. Ions, in this case argon, are accelerated to collide with the target, producing the material(target) to be detached and deposited on the substrate surface. A constant magnetic field created by magnets allows a high rate of ionization as electrons will be magnetized (trapped) near the target surface. Another important process beyond the sputtering is the emission of secondary electrons from the target surface.

All magnetrons consist of an anode and cathode block, heater, output coupling loop and permanent magnets. In magnetron operation, the ions are created by a plasma discharge and are accelerated by the electric field. These ions bombarding the cathode plate lead to the neutral atoms detachments that once they reach the substrate, condense as a thin film. Different magnetic field configurations and power supplies are used for various regimes of magnetron sputtering.

Hall thruster operation is as follows: the radial magnetic field obstructs electron motion in the axial

direction. Electrons are emitted from the cathode, as they have a Larmor radius much smaller than the characteristic length of the device, they are magnetized. Electrons drift in the azimuthal direction due to the $\mathbf{E} \times \mathbf{B}$ drift [4]. While they slowly move toward the anode as a result of electron-wall collisions and waves, they also ionize neutrals before they reach the anode. The trust is produced by the resulting ions (leaving the channel) accelerated by the axial electric field. The resulting ions leave the channel, accelerated by the axial electric field and they create thrust.

The components of the Hall-effect-thruster (HET) are: two concentric cylinders with one of the cylinder sides closed and the other side open, a magnetic core or electromagnets, and the flow of the propellant for ionization in the thruster channel. Between the inner and outer walls, an open area inside the inner cylinder is filled with a dielectric or metal material [4]. Outside the open side of the HET, a cathode (the electrons source) is placed, while the positively charged electrode, the anode, is located on the closed side. The discharge ignition and the charged particles acceleration occur in the discharge-chamber.

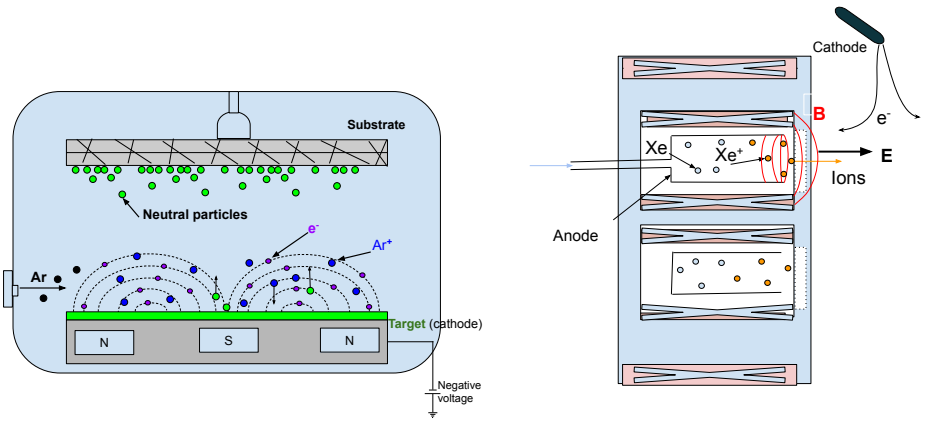

(a) Planar magnetron scheme.

(b) Hall-thruster, with axial electric field E, and applied radial magnetic field B.

Figure 1.1: A schematic representation of plasma devices.

Turbulent fluctuations and related anomalous transport and plasma structures are factors to take into account for the plasma device performance and lifetime.

1.3 Kinetic description of plasmas

Kinetic model is the most complete approach for plasma description. One can derive an exact equation for the evolution of a plasma, known as the Klimontovich equation.

$$\frac{D}{Dt} N_\alpha(\mathbf{x}, \mathbf{v}, t) = 0, \tag{1.3}$$

This equation together with the Maxwell's equations establishes exact description of plasma. In the absence of collisions, this equation arises by taking the total time derivative of the particle density N_α in the six-dimensional phase space $(\mathbf{x}, \mathbf{v})$ [1]

where the subscript α denotes a specie kind (e.g. electrons, ions), with the operator

$$\frac{D}{Dt} = \frac{\partial}{\partial t} + \mathbf{v} \cdot \frac{\partial}{\partial \mathbf{x}} + \mathbf{a} \cdot \frac{\partial}{\partial \mathbf{v}}, \tag{1.4}$$

where $\mathbf{v}$ represents particle position change in time, and $\mathbf{a}$ – the particle velocity change. These particle orbits in phase space are described by equations of motion for individual particles in microscopic fields (found via Maxwell equations). Thus, the expression (1.3) defines the conservation of the number of particles in the phase space. The Klimontovich equation (1.3) gives a detailed information of every single particle trajectory. The particle density distribution N_α is expressed in the following form

$$N_\alpha = \sum_{k=1}^{N_0} \delta(\mathbf{x} - \mathbf{x}_k(t))\delta(\mathbf{v} - \mathbf{v}_k(t)), \tag{1.5}$$

where N_0 is the total number of particles. However, for our purpose in particle-based simulations, we are looking for averaged plasma properties instead of fully detailed information of every particle in a plasma. Therefore, a particle distribution function $f = f(\mathbf{x}, \mathbf{v}, t)$ is defined in six-dimensional phase space $(\mathbf{x}, \mathbf{v})$ to describe and model the evolution of plasma. The distribution function is defined as an averaged number of point particles per unit volume in phase space. The Vlasov equation is used to describe the evolution of the distribution function in time, in the absence of collisions it is written as

$$\frac{\partial f_\alpha}{\partial t} + \mathbf{v} \cdot \frac{\partial f_\alpha}{\partial \mathbf{x}} + \frac{q_\alpha}{m_\alpha}(\mathbf{E} + \mathbf{v} \times \mathbf{B}) \cdot \frac{\partial f_\alpha}{\partial \mathbf{v}} = 0, \tag{1.6}$$

which needs to be combined with Maxwell equations to determine the evolution of electromagnetic fields

$$\nabla \cdot \mathbf{E} = \frac{\rho}{\epsilon_0}, \tag{1.7}$$

$$\nabla \cdot \mathbf{B} = 0, \tag{1.8}$$

$$\nabla \times \mathbf{E} = -\frac{\partial \mathbf{B}}{\partial t}, \tag{1.9}$$

$$\nabla \times \mathbf{B} = \mu_o \mathbf{J} + \mu_o \epsilon_0 \frac{\partial \mathbf{E}}{\partial t}, \tag{1.10}$$

where charge density ρ and electric current $\mathbf{J}$ are given with

$$\rho = \sum_\alpha \int q_\alpha f_\alpha \mathrm{d}^3 v, \tag{1.11}$$

$$\mathbf{J} = \sum_\alpha \int q_\alpha \mathbf{v}_\alpha f_\alpha \mathrm{d}^3 v. \tag{1.12}$$

The Vlasov-Maxwell (VM) system of time-dependent partial differential equations (1.6-1.10) is the full kinetic model for the evolution of the collisionless magnetized plasma.

The fundamental idea of particle-based methods is to solve the kinetic equation by using particle trajectories (characteristics of the kinetic equation) instead of resolving the Vlasov equation as PDE. In other words, the simulation solves the Vlasov equation characteristics, $\mathbf{x}(t)$ and $\mathbf{v}(t)$, given by the classical

equations of motion

$$\frac{d\mathbf{x}(t)}{dt} = \mathbf{v}(t), \tag{1.13}$$

$$\frac{d\mathbf{v}(t)}{dt} = \frac{q}{m}\left(\mathbf{E} + \mathbf{v} \times \mathbf{B}\right). \tag{1.14}$$

The coupling between Newton's and Maxwell's equations is the following: the electric and magnetic fields are required for Newton's equations in order to compute the force and to advance the particles. The fields from the Maxwell's equations are recalculated based on the density and current due to the particle position. Particles follow characteristic lines, and the fields are computed on the grid. This is the essence of Particle-in-Cell methods.

1.4 Particle motion and drifts in plasma

Here we briefly review some types of charged particle motion in the **E** and **B** fields. The equation of motion for a particle of charge q, under the influence of the Lorentz force **F** due to electric **E** and magnetic **B** fields, can be written as:

$$\frac{d\mathbf{P}}{dt} = \mathbf{F}, \quad \text{or} \tag{1.15}$$

$$m\frac{d\mathbf{v}}{dt} = q\mathbf{E} + q(\mathbf{v} \times \mathbf{B}), \tag{1.16}$$

where $\mathbf{P} = m\mathbf{v}$ and motion is considered as the non-relativistic, with particle charge q and mass m. For a charged particle in a constant uniform magnetic field **B**, with $\mathbf{E} = 0$ with charge q, mass m, and velocity **v**, the equation of motion becomes

$$m\frac{d\mathbf{v}}{dt} = q(\mathbf{v} \times \mathbf{B}). \tag{1.17}$$

We can represent the velocity **v** in terms of parallel and perpendicular components. For motion in the plane perpendicular to **B**, from Eq. (1.17) the perpendicular component is expressed as

$$\frac{d\mathbf{v}_\perp}{dt} = \mathbf{\Omega}_c \times \mathbf{v}_\perp, \tag{1.18}$$

where $\mathbf{v}_\perp = \mathbf{\Omega}_c \times \mathbf{r}_\perp$ and $\mathbf{\Omega}_c$ denotes the cyclotron frequency, $\mathbf{\Omega}_c = q\mathbf{B}/m$. Circular motion of a charged particle about a guiding center, in a uniform magnetostatic field will be in the plane normal to **B**. Due to the superposition of parallel component and circular motion the particle trajectory will be a helix. We assume that the direction of the magnetic field is along the z-axis, then Eq. (1.17) could be expressed in terms of its components $\dot{\mathbf{v}}_x = \Omega_c \mathbf{v}_y, \dot{\mathbf{v}}_y = -\Omega_c \mathbf{v}_x$, $\dot{\mathbf{v}}_z = 0$, resulting in the particle velocity components

$$v_x = v_0 \cos(\Omega_c t + \alpha), \tag{1.19}$$

$$v_y = v_0 \sin(\Omega_c t + \alpha), \tag{1.20}$$

where $\Omega_c = qB/m$ is magnitude of the cyclotron frequency, v_0 is the speed of particle in the plane perpendicular to **B**, and α is the phase that defined by the initial conditions as $\alpha = \tan^{-1}\left[v_x(0)/v_y(0)\right]$. Then, the

particle coordinates

$$x = x_0 + \frac{v_0}{\Omega_c}\sin(\Omega_c t + \alpha), \tag{1.21}$$

$$y = y_0 - \frac{v_0}{\Omega_c}\cos(\Omega_c t + \alpha), \tag{1.22}$$

where x_0, y_0 are the guiding center coordinates, $x_0 = x(0) - (v_0/\Omega_c)\sin(\alpha)$ and $y_0 = y(0) + (v_0/\Omega_c)\cos(\alpha)$.

For a constant uniform electric field $\mathbf{E}$ along y-direction, for a charged particle with charge q, mass m and velocity $\mathbf{v}$, and without a magnetic field, particle motion will be in the xy-plane. The equations of motion Eq (1.15) become:

$$\frac{dP_y}{dt} = e\mathbf{E}, \quad \frac{dP_x}{dt} = 0, \tag{1.23}$$

leading to the expression for the particle position as a function of time:

$$\mathbf{r} = \frac{q\mathbf{E}}{2m}t^2 + \mathbf{v}_0 t + \mathbf{r}_0. \tag{1.24}$$

After integrating Eq (1.23), we find the charged particle trajectory in the $x - y$ plane is the parabola

$$y = y_0 + \frac{v_{0y}}{v_{0x}}(x - x_0) + \frac{qE_y}{2m}\left(\frac{x - x_0}{v_{0x}}\right)^2. \tag{1.25}$$

Now considering a particle motion in a constant uniform electric and magnetic field, where we choose the direction of the magnetic field $\mathbf{B}$ to be along the z-axis and defining the plane passing through $\mathbf{E}$ and $\mathbf{B}$ as the $y - z$ plane, the particle velocities become:

$$\begin{aligned} v_x &= v'_\perp \cos(\Omega_c t + \alpha) - \frac{E_y}{B}, \\ v_y &= -v'_\perp \sin(\Omega_c t + \alpha) + \frac{E_x}{B}, \end{aligned} \tag{1.26}$$

where $v'_\perp$ and α are integration constants. Then, the coordinates are:

$$\begin{aligned} x &= \frac{v'_\perp}{\Omega_c}\sin(\Omega_c t + \alpha) - \frac{E_y t}{B} + x_0, \\ y &= -\frac{v'_\perp}{\Omega_c}\cos(\Omega_c t + \alpha) + \frac{E_x t}{B} + y_0, \end{aligned} \tag{1.27}$$

where x_0, y_0 defined as previously but with $v'_\perp$.

Now we consider a drift motion adding an external force, the equation of motion (1.15) becomes

$$\frac{d\mathbf{P}}{dt} = q(\mathbf{v} \times \mathbf{B}) + \mathbf{F}. \tag{1.28}$$

Therefore, this force $\mathbf{F}$ produces a drift which has a component perpendicular to $\mathbf{B}$. Thus, the drift velocity v_F is described by:

$$\mathbf{v}_F = \frac{\mathbf{F} \times \mathbf{B}}{qB^2}. \tag{1.29}$$

Being the electric field $\mathbf{E}$, a force acting on the particle, the $\mathbf{E} \times \mathbf{B}$ drift is one of the most common forms of motion for a single-particle in plasma. Charged particle velocity in an electromagnetic field is composed of three components. Parallel velocity $v_\parallel$, where particle moves parallel to $\mathbf{B}$ with constant acceleration $q\mathbf{E}_\parallel/m$, gyration velocity v_L, the rotation in the plane perpendicular to $\mathbf{B}$, and the cross-field drift velocity $\mathbf{v}_d$, the drift velocity in electromagnetic fields [2], is:

$$\mathbf{v}_d = \frac{\mathbf{E} \times \mathbf{B}}{B^2}. \tag{1.30}$$

Particles follow cycloid trajectories in general, where the initial magnitude of the electric and magnetic fields determine the particle trajectories. Assuming that the electric field $\mathbf{E}$ varies with time, we obtained a

polarization drift, we can rewrite the Eq (1.30) as:

$$\dot{\mathbf{v}}_d = \frac{\dot{\mathbf{E}} \times \mathbf{B}}{B^2}. \tag{1.31}$$

A drift velocity is necessary to produce a magnetic force equal to $m\dot{\mathbf{v}}_d$:

$$q\ (\mathbf{v}_p \times \mathbf{B}) = m\dot{\mathbf{v}}_d = m\frac{\dot{\mathbf{E}} \times \mathbf{B}}{B^2}, \tag{1.32}$$

where a resulting polarization drift velocity $\mathbf{v}_p$ is described as

$$\mathbf{v}_p = \frac{\dot{\mathbf{E}}(\mathbf{t})}{\Omega_c B}. \tag{1.33}$$

1.5 Plasma waves, instabilities and anomalous transport

Plasma oscillations represent very complex phenomena both in linear and nonlinear regimes. Wave propagation, diffusion, wave growth and damping can be involved. Schematically, and in the linear regime, one can view these phenomena represented by the partial differential equation in time and space [5]:

$$\nabla^2\psi = \frac{1}{c^2}\psi_{tt} + g\psi_t + b\psi. \tag{1.34}$$

Eq. (1.34) describes waves that depend on time and space for a quantity $\psi(x, y, z, t)$. Depending on the coefficients c, g, b, this partial differential equation characterizes the properties of the wave propagation, diffusion, and growth/damping, respectively. In the simplest stable case, it can be reduced to the wave equation

$$\frac{\partial^2\psi}{\partial t^2} = c^2\nabla^2\psi. \tag{1.35}$$

A linear wave that satisfies Eq. (1.34) has a phase $\theta(\mathbf{x}, t)$ as a linear function, e.g. it can be represented as time and spatial dependence in the form $\sim\exp(i\mathbf{k}\cdot\mathbf{x} - i\omega t)$ for small amplitude modes, according to the linear theory. The relationship between frequency ω and wave vector k is called the dispersion relation

$$D(\omega, \mathbf{k}) = 0\ \equiv D_r + iD_i, \tag{1.36}$$

with the real wave vector $\mathbf{k}$, and the complex frequency $\omega = \omega_r + i\gamma$. For the equations of the types (1.34), the dispersion relation is algebraic but in the kinetic models, it can be in the transcendental form.

The specific nature of particular waves is determined by various factors, such as the external magnetic and electric fields. The following scheme shows a general classification of plasma waves in basic configurations:

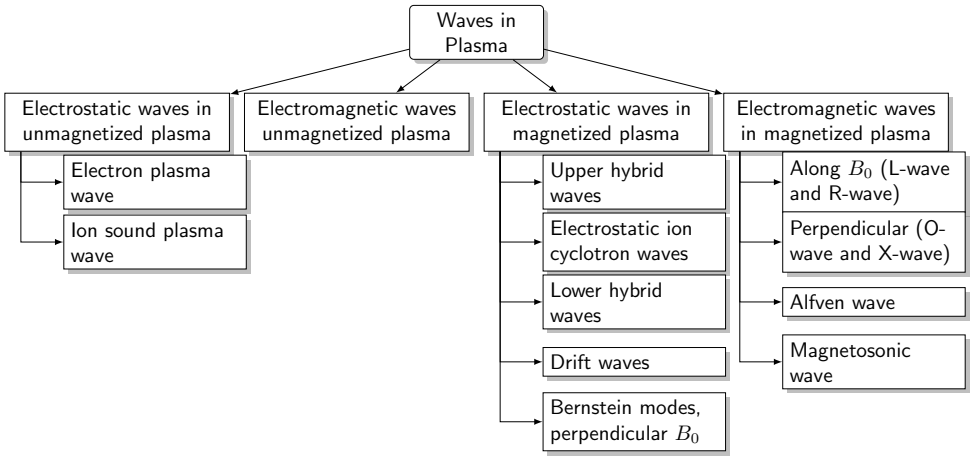

An oscillatory motion of a single particle generates waves which interact with other particles, leading to variations in quantities like density and electromagnetic fields.

Different waves can be classified by some properties, whether the plasma is magnetized or unmagnetized, by the direction of the wave vector $\mathbf{k}$ with respect to the external magnetic field B_0, and the direction of the induced electric field E_1 (wave polarization). Under certain conditions, these variations lead to unstable waves, i.e. instabilities in plasma, which may produce turbulence and anomalous transport. Plasma can deviate from the thermodynamic equilibrium, and a small deviation becomes the cause of further deviations. Free energy in the plasma is exponentially converted into fluctuating electromagnetic field energy. This process is called an instability [6]. The presence of beams of charged particles, resonances between particles and waves, and anisotropy of the distribution function are all possible causes for instabilities to arise in plasma [7]. Instability occurs when the mode frequency acquires a positive imaginary part, $\mathrm{Im}(\omega) > 0$. In this thesis, I will show a derivation for the Bernstein modes (magnetized plasma with propagation perpendicular to the magnetic field) and ion sound waves which form a basis for the ECDI (Chapter 2).

Instabilities in plasma can be classified as microinstabilities and macroinstabilities. Microinstabilities are due to velocity space non-equilibrium, and macroinstabilities are due to coordinate space non-equilibrium [1]. They can be explained using two different approaches: fluid or kinetic. In this work, a kinetic approach is used since the ECDI is an instability due to microscopic gyro-motion of particles in a plasma. The long-range electromagnetic interaction that exhibits collective effects and leads to various nonlinear wave and turbulent phenomena, defines the complex behavior of plasmas. Modes that grow in space and time characterize the unstable plasma behavior. If perturbations in the magnetic field are neglected, a "potential" instability may arise. Furthermore, development of a "potential" or "non-potential" instability depends on the presence of an external magnetic field. Linearly unstable instabilities may occur when the dispersion relation Eq. (1.36) has a solution with a positive imaginary part. The following table summarizes the main dispersion relations for wave phenomena in plasma:

PLASMA WAVE	DISPERSION RELATION
Electron plasma	$\omega^2 = \omega_{pe}^2 + \frac{3}{2}k^2 v_{Te}^2$
Ion Sound	$\omega^2 = k^2 c_s^2 / \left(1 + k^2 \lambda_D^2\right)$
Upper hybrid	$\omega^2 = \omega_{pe}^2 + \Omega_e^2 + \frac{3}{2}k^2 v_{Te}^2$
Lower hybrid	$\omega^2 = k_x^2 c_s^2 + \lvert\Omega_i \Omega_e\rvert$
Electromagnetic	$\omega^2 = \omega_{pe}^2 + k^2 c^2$
Alfven	$\omega^2 = k_z^2 V_A^2$
Magnetosonic	$\omega^2 = k^2 V_A^2$
Bernstein modes	$1 + \sum_j \frac{1}{k^2 \lambda_{Dj}^2} \left\{ 1 + \sum_{-\infty}^{\infty} I_n(k\rho_j) e^{-k\rho_j} \left(\frac{\omega}{k_\parallel v_{Tj}} \right) Z \left(\frac{\omega - n\Omega_{cj}}{k_\parallel v_{Tj}} \right) \right\} = 0$
Ion cyclotron waves	$\omega^2 = k^2 c_s^2 + \Omega_i^2$

The notation used in the table unfolds as the following: $v_{Te}^2 = 2T_e/m_e$ is the electron thermal velocity,

$c_s^2 = T_e/m_i$ is the ion sound velocity, Ω_e and Ω_i are the electron and ion gyro-frequencies, c is the speed of light, $V_A^2 = B/\mu_0 m_i n_i$ is the Alfven velocity, j is the specie kind, $\rho = v_T/\Omega_c$ is the gyroradius. The external magnetic field with the magnitude B is assumed along z-direction, thus the wave vector k_z denotes the parallel direction, while k_x stands for the perpendicular.

Before proceeding further with the anomalous current description in kinetic plasma simulations, it is necessary to recall the classical transport in devices of Hall thruster type. Classical transport is a result of electron-neutral or electron-ion collisions. These collisions cause momentum to be exchanged between particles. The effective electron collision frequency ν_e is described by the known Hall Parameter

$$\Omega_H = \frac{\Omega_c}{\nu_e}, \tag{1.37}$$

where $\Omega_c = eB/m$ is the cyclotron frequency. Hall Parameter defines how effective the particle is magnetized, or roughly how many rotations it performs in magnetic field before a collision occurs. Collisional transport due to a random-walk process is affected by the presence of a magnetic field. Therefore, for a magnetized plasma, $\nu_e \ll \Omega_c$, the motion of charged particles is determined by the magnetic field, rather than the collisions. Each charged particle in a plasma is subjected to the Lorentz force perpendicular to their velocities. Charged particles within a straight and constant magnetic field retain a constant velocity $v_\perp$ and velocity $v_\parallel$, since the kinetic energy is conserved. The gyration radius does not change, but the phase of the particle with respect to B changes continuously. Thus, particle diffusion across magnetic field leads to a helix trajectory. Particle transport across the field is due to a shift in the guiding-centre position because of a change in the vector velocity caused by collisions [8]. A higher charged particle diffusion generates an electrostatic turbulence. This turbulent electric field yields a random drift velocity of the electron guiding centers. The general diffusion equation is given by:

$$\frac{\partial n}{\partial t} = \nabla \cdot (D \nabla n). \tag{1.38}$$

A theoretical explanation for a higher charged particle diffusion rate in a plasma is given by Bohm diffusion that considers the random-walk process due to turbulent fluctuations in the plasma. According to Bohm diffusion, an estimate for the particle diffusion coefficient is described by [9]:

$$D_e = \frac{(\Delta x)^2}{\tau}, \tag{1.39}$$

where Δx is the mean free path, and τ is the inverse of collision frequency.

In a Hall thruster, one can refer to anomalous current, to the observed current that is much larger than predicted by classical collisional theory. There exist various mechanisms to explain the anomalous electron transport in Hall thruster devices. One well known mechanism is the near-wall transport, where the electron-wall collisions determine the electron transport. Another mechanism is the fluctuation-induced transport, where plasma oscillations have an effect in cross-field electron diffusion. Instabilities such as the ECDI, lead to fluctuations in both the electric field and in the number of plasma density. These instabilities in the azimuthal direction are candidates to enhance anomalous cross-field transport in the axial direction.

In this work, the partially magnetized plasma simulations are modeled in the absence of electron-neutral or ion-electron collisions. In spite of this, the simulation results still show the aforementioned anoma-

lous current. The electron current density J_z (in axial direction) is obtained as follows:

$$J_z = q_e n_e V_z = q_e \int v_{ez} f_e \mathrm{d}^3 v, \tag{1.40}$$

where v_{ez} is the microscopic axial electron velocity. In order to obtain the total anomalous current density $J_z(x, y)$ along the z-axis (that corresponds to the axial direction in my setup) the averaged velocities (in each node) along the z-axis $V_z(x, y)$ were used, along with the respective electron density $n_e(x, y)$. The anomalous electron current density averaged in space is written as:

$$\langle J_z \rangle = \frac{q_e}{L_x L_y} \int n_e V_z \mathrm{d}x \mathrm{d}y. \tag{1.41}$$

Electron current density J_z can be calculated directly from a kinetic simulation, since it contains the distribution functions output. Also, the current density in Eq. (1.41) can be expressed via the Hall parameter as:

$$\langle J_z \rangle = \frac{q_e^2 n_0}{m_e \nu_e} E_z \Omega_H. \tag{1.42}$$

The response of the plasma to a perturbed field can be calculated based on the fluid equations: continuity equation, equation of motion and energy balance equation [2]. Plasma fluid equations describe time evolution and conservation of macroscopic variables, such density, momentum, energy, etc. Assuming collisionless plasma, they can be derived as the moments of the Vlasov equation (2.1). In the plasma kinetic simulation, one can calculate the macroscopic quantities from the distribution function itself and check if it conforms with the fluid equations. Therefore, a balance can be checked to identify the major terms that play a significant role in the electron transport. One can write the electron momentum conservation as following:

$$\frac{\partial}{\partial t}(m n_e \mathbf{V}_e) + \nabla \cdot (m n_e \mathbf{V}_e \mathbf{V}_e) = q n_e (\mathbf{E} + \mathbf{V}_e \times \mathbf{B}) - \nabla p_e, \tag{1.43}$$

where the generalized viscosity tensor and drag forces are neglected. This expression can be represented in the conservative form as [10]

$$\frac{\partial}{\partial t}(m n_e \mathbf{V}_e) + \nabla \cdot (m n_e \mathbf{V}_e \mathbf{V}_e + p_e \mathbf{I}) = \mathbf{f}_b \tag{1.44}$$

where $\mathbf{f}_b$ is an external force per unit volume. The electric field in the two-dimensional simulation is $\mathbf{E} = \mathrm{E}_x \hat{x} + \mathrm{E}_y \hat{y} + \mathrm{E}_{z,ex} \hat{z}$, where $\mathrm{E}_x, \mathrm{E}_y$ are self-consistent fields, and $\mathrm{E}_{z,ex}$ is the applied field in the axial direction; $\mathbf{B} = \mathrm{B}_y \hat{y}$ is the applied magnetic field (in radial direction). Eq. (1.43) in components is written in the non-conservative form as

$$m n_e \left[\frac{\partial}{\partial t}(V_{ex}) + V_{ex} \frac{\partial V_{ex}}{\partial x} + V_{ey} \frac{\partial V_{ex}}{\partial y} \right] = q n_e (\mathrm{E}_x - V_{ez} \mathrm{B}_y) - \frac{\partial p_e}{\partial x}, \tag{1.45}$$

$$m n_e \left[\frac{\partial}{\partial t}(V_{ey}) + V_{ex} \frac{\partial V_{ey}}{\partial x} + V_{ey} \frac{\partial V_{ey}}{\partial y} \right] = q n_e \mathrm{E}_y - \frac{\partial p_e}{\partial y}, \tag{1.46}$$

$$m n_e \left[\frac{\partial}{\partial t}(V_{ez}) + V_{ex} \frac{\partial V_{ez}}{\partial x} + V_{ey} \frac{\partial V_{ez}}{\partial y} \right] = q n_e \left(\mathrm{E}_{z,ex} + V_{ex} \mathrm{B}_y \right), \tag{1.47}$$

where each term in Eqs. (1.45-1.47) can be computed using the output from the simulation. For example, it is easy to show that there is a net drift in x-direction when one neglects the unsteady ($\partial \mathbf{V}/\partial t$) and inertia ($\mathbf{V} \cdot \nabla \mathbf{V}$) terms, also assuming the internal electric field and pressure are negligible. Then, the Eq. (1.47) is written as

$$0 = q n_e \mathrm{E}_{z,ex} + \omega_{ce} V_{ex}, \tag{1.48}$$

and thus $V_{ex} = \mathrm{E}_{z,ex}/\mathrm{B}_y$. Similarly, one could expect that in the steady state the electron current in z-direction can be driven with the drift velocity $V_{ez} = \mathrm{E}_x/\mathrm{B}_y$, i.e. by the fluctuating internal azimuthal electric field. Later, in Chapter 4, a good agreement will be shown between the simulation results and this $\widetilde{\mathbf{E}}_\theta \times \mathbf{B}$ current.

2 Ion Sound mode and ECDI

2.1 Ion sound waves

Ion sound modes are low frequency plasma waves, characterized by plasma frequency $\omega \leq \omega_{pi}$, where ω_{pi} is the ion plasma frequency in an unmagnetized plasma. Further, in the coming sections, dispersion relations equations for specific modes/waves that arise in the simulations will be presented. Recalling that the simulations performed are fully kinetic, one can derive the general kinetic dispersion equation from the Vlasov equation described in the previous Chapter 1. Starting with the one-dimensional Vlasov equation

$$\frac{\partial f}{\partial t} + v\frac{\partial f}{\partial x} + \frac{q_\alpha}{m_\alpha}\mathrm{E}\frac{\partial f}{\partial v} = 0, \tag{2.1}$$

where $\alpha = (i, e)$ denote ions or electrons, and the electric field E must be obtained self-consistently from the Poisson equation. We would like to consider the distribution function in the form $f(x, v, t) = f_{0\alpha} + \widetilde{f_\alpha}$, and the electric field $\mathrm{E}(x, t) = \widetilde{E}(x, t)$, which can be represented with the expression $\widetilde{E} = -\nabla_x\widetilde{\phi}$. The wavelike solutions are intended in the form $\widetilde{f_\alpha} \sim \exp(-i(\omega t - kx))$, where in Fourier space we find $\widetilde{f_\alpha}$ from Eq. (2.1)

$$\widetilde{f_\alpha} = \frac{q_\alpha}{m_\alpha}\frac{\phi\partial f_{0\alpha}/\partial v}{\omega - vk}. \tag{2.2}$$

If we integrate Eq. (2.2) over velocity space we obtain the perturbed density

$$\widetilde{n}_\alpha = \frac{q_\alpha\widetilde{\phi}kn_\alpha}{m_\alpha}\int_{-\infty}^{\infty}\frac{\partial f_{0\alpha}/\partial v}{\omega - vk}dv, \tag{2.3}$$

where $n_{0\alpha}$ is the equilibrium density. Due to the electrostatic approximation, the fluctuating electric field is given by the linearized Poisson equation. Substituting Eq. (2.3) into the Poisson equation:

$$\frac{\partial^2\widetilde{\phi}}{\partial x^2} = -4\pi\sum_\alpha e_\alpha\widetilde{n}_\alpha, \tag{2.4}$$

we obtain the general dispersion relation

$$1 + \sum\frac{\omega_{p\alpha}^2}{k^2}\int_{-\infty}^{\infty}\frac{\partial f_{0\alpha}/\partial v}{\omega - vk}dv = 0, \tag{2.5}$$

where, $\omega_{p\alpha}$ is the plasma frequency $\omega_{p\alpha} = \sqrt{4\pi n_\alpha q_\alpha/m_\alpha}$. For the stationary distribution function in the Vlasov equation, ions and electrons are defined by the Maxwellian distribution function in one-dimensional case

$$f_M = \frac{n_\alpha}{\pi^{3/2}v_{T\alpha}^3}e^{-v^2/v_{T\alpha}^2}, \tag{2.6}$$

where $v_{T\alpha}^2 = 2T_\alpha/m_\alpha$, and T_α (in J) the isotropic temperature. The dispersion relation (2.5) involves a non-trivial plasma dispersion function appendix B

$$Z(\zeta) = \pi^{-1/2}\int_{-\infty}^{\infty}\frac{e^{-t^2}}{t - \zeta}dt. \tag{2.7}$$

We now can transform Eq. (2.3) with the assumption that $f_{0\alpha}$ is Maxwellian and by utilizing the definition of the plasma dispersion function, the macroscopic density is found to be

$$\widetilde{n}_\alpha = \frac{q_\alpha \phi n_{0\alpha}}{m_\alpha v_{T_\alpha}} \int_{-\infty}^{\infty} \frac{(d/dt)(e^{-t})}{t-\zeta} dt, \tag{2.8}$$

where $\zeta_\alpha = \omega/(k v_{T\alpha})$. As mentioned, in order to obtain the general dispersion for one-dimensional longitudinal waves, we substitute the Eq. (2.8) into the Poisson equation (2.4). Using the definition of the first derivative of the plasma dispersion function $\mathrm{Z}'(\zeta) = -2\,(1+\zeta \mathrm{Z})$, the density perturbation is written as:

$$\widetilde{n}_\alpha = -\frac{Z'(\zeta) q_\alpha \widetilde{\phi} n_{0\alpha}}{2T_\alpha}. \tag{2.9}$$

Now Eq. (2.9) can be substituted into the general Eq. (2.5), hence the general dispersion relation for these longitudinal modes is

$$1 - \sum_\alpha \frac{\omega_{p\alpha}^2}{k^2 v_{T_\alpha}^2} \mathrm{Z}^{'}(\zeta_\alpha) = 0 \quad \text{or} \tag{2.10}$$

$$-1 = -\frac{1}{k^2 \lambda_D^2} Z'(\zeta_e) - \frac{w_{pi}^2}{k^2 v_{T_i}^2} Z'(\zeta_i), \tag{2.11}$$

where $\lambda_D^2 = T_e/4\pi n_{0e} q_e^2$ is the electron Debye length. The equation (2.11) is a very general expression and contains solutions to a multitude linear phenomena in unmagnetized electrostatic plasma of various scale, such as electron plasma waves, ion sound waves, and Landau damping effects. The following assumptions (simplifications) allow a simple derivation of the low frequency ion-sound modes. For ion sound waves the electron damping can be neglected. As we seek for low frequencies, $\zeta_e \ll 1$ and $Z'(\zeta_e) \approx -2$, which also corresponds to the (linearized) Boltzmann relation for density $\widetilde{n}_e = n_\alpha e\widetilde{\phi}/T_e$. For ions we have $\zeta_i \gg 1$, with the first real term in the expansion $Z'(\zeta_i) = 1/\zeta_i^2 + 3/2\zeta_i^4$ (Eq. (B.5)), and substituting it into the Eq. (2.11) we obtain the ion sound dispersion relation:

$$\omega^2 = \frac{k^2 c_s^2}{k^2 \lambda_D^2 + 1}. \tag{2.12}$$

The expansion of the plasma dispersion function also contains the imaginary term, responsible for Landau wave-particle resonance effects. Including it into Eq. (2.11) we obtain the dispersion relation

$$-1 = \frac{1}{k^2\lambda_D^2} - \frac{\omega_{pi}^2}{k^2 v_{T_i}} \left(-2i\pi^{1/2} \zeta_i e^{-\zeta_i^2} + \frac{1}{\zeta_i^2} + \frac{3}{2\zeta_i^4} \right), \tag{2.13}$$

this equation will be solved for the lowest order, thus in such approximation we can neglect the imaginary term

$$-1 = \frac{1}{k^2\lambda_D^2 2} - \frac{\omega_{pi}^2}{k^2 v_{T_i}^2} \left(\frac{1}{\zeta_i^2} + \frac{3}{2\zeta_i^4} \right) \text{or} \tag{2.14}$$

$$-k^2\lambda_D^2 = 1 - \frac{T_e}{2T_i} \left(\frac{1}{\zeta_i^2} + \frac{3}{2\zeta_i^4} \right), \tag{2.15}$$

where the term $k^2\lambda_D^2$ is also neglected, assuming a weak dispersion, $k\lambda_D \ll 1$, it becomes

$$\frac{1}{\zeta_i^2} \left(1 + \frac{3}{2\zeta_i^2} \right) = 2\frac{T_i}{T_e}, \tag{2.16}$$

which is simplified and solved using $1/\zeta_i^2 \approx 2T_i/T_e$, giving

$$\zeta_i^2 = \frac{1 + 3T_i/T_e}{2T_i/T_e}, \tag{2.17}$$

which represents the lowest order solution to Eq. (2.13). It expresses the dispersion equation for ion-sound waves with electron thermal effects, and it can be described in the form

$$\frac{\omega^2}{k^2} = \frac{T_e + 3T_i}{m_i}, \tag{2.18}$$

with $\omega = kc_s$, and ${c_s}^2 = (T_e + 3T_i)/m_i$. While the dispersion relation $\omega = kc_s$ is an approximation in the weak dispersion case (we neglected the $k^2\lambda_D^2$ term), we could obtain a more accurate expression for the ion sound velocity, by including the next order term in Z′ expansion. Finally, we substitute it into Eq. (2.13) seeking for a more precise solution (with Landau resonance effects)

$$-2i\pi^{1/2}e^{-\zeta_i^2} + \frac{1}{\zeta_i^2} + \frac{3}{2\zeta_i^4} = 2\frac{T_i}{T_e}, \tag{2.19}$$

and taking again the approximation $1/\zeta_i^2 \approx 2T_i/T_e$, one can rewrite it as

$$\zeta_i \approx \left(\frac{1 + 3T_i/T_e}{2T_i/T_e}\right)^{1/2}\left(1 - \frac{i}{2}\frac{T_e}{T_i}\sqrt{\pi}\zeta_i e^{-\zeta_i^{-2}}\right), \tag{2.20}$$

which describes the dispersion relation for the ion-sound waves with the Landau damping effects (the imaginary component is negative). It can be seen that the temperature ratio T_e/T_i plays a determining role in the Landau damping rate. We present the damping rate is as follows:

$$-\frac{\mathrm{Im}(\zeta_i)}{\mathrm{Re}(\zeta_i)} = \sqrt{\frac{\pi}{8}}\sqrt{\frac{1 + 3T_i/T_e}{(T_i/T_e)^3}}e^{-\left(1+3\frac{T_i}{T_e}\right)/2\frac{T_i}{T_e}}. \tag{2.21}$$

According to this damping rate, the ion sound waves do no exist for comparable ion and electron temperatures, $T_i/T_e \approx 1$, due to much higher Landau damping compared to a lower ion temperatures ratio, as shown in Fig. 2.1. This increased damping will not allow the ion sound waves to propagate.

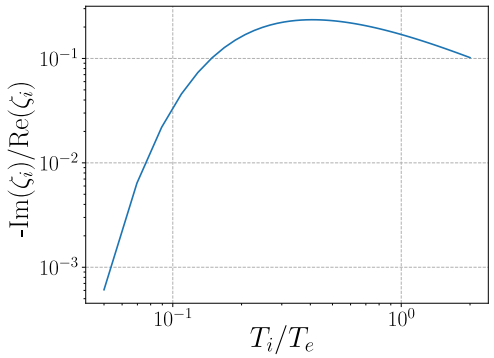

Figure 2.1: Damping rate as a function of temperatures ratio, an approximate solution (2.21) to the dispersion Eq. (2.13) with ion Landau damping.

The idea illustrated in Fig. 2.2 shows an ion Maxwellian velocity distribution with two different ion thermal velocities and the corresponding phase velocities ω/k obtained from Eq. (2.18). The resonant velocity ω/k corresponds to $\zeta_i \simeq -1$ when there are many particles moving near the phase speed of the wave, this is a strong wave-particle interaction. In contrast, when $\zeta_i \gg 1$ the wave is moving faster than almost all particles, this corresponds to the non-resonant case. The interaction between the wave and the associated species is illustrated by the intersection of the dashed lines and the particle distribution functions.

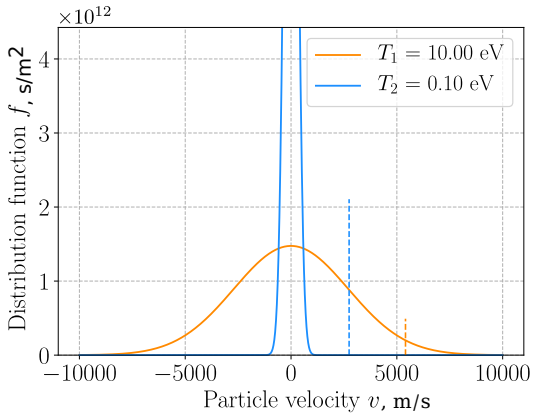

Figure 2.2: Illustration of warm (T_1) and cold (T_2) ion distribution functions for the ion sound waves with the appropriate phase velocities (dashed lines with the same color). Note that there is practically no resonant interaction in the case of cold ions. Electron temperature $T_e = 10$ eV is assumed.

It is shown that the interaction of the associated ion sound wave with the 10 eV species is stronger than that of the wave interaction with a lower temperature species. The overall result of a strong interaction is characterized by a higher Landau damping, then when $T_i/T_e \approx 1$ the ion sound wave will not propagate.

2.2 Bernstein modes

In addition to the waves modes presented in the previous subsection, the kinetic theory states that there are modes that can appear for a basic problem involving plasma particle motion in an applied magnetic field. Accordingly, for a given magnetic field, particles move in the parallel direction and perform a gyro motion with the radius $\rho = v_\perp/\omega_c$ perpendicularly to the magnetic field ($\omega_c = qB/mc$, the cyclotron frequency, c the speed of light). Particles in the parallel direction can move in the same way as without the applied magnetic field (free streaming). In the perpendicular direction the so-called Bernstein modes appear [11]. The short derivation of these modes is following, under the following assumptions

A. A homogeneous magnetized plasma

B. Electrostatic perturbation, i.e. $\mathbf{E} = -\nabla\phi$

C. $\mathbf{k}$ vector in x, z plane

D. Uniform magnetic field along z direction, $\mathbf{B} = B_0\hat{z}$

The distribution function $f(\mathbf{x}, \mathbf{v}, t)$ can be represented in the form

$$f = f_0(\mathbf{v}) + \widetilde{f}(\mathbf{x}, \mathbf{v}, t), \tag{2.22}$$

where $f_0(\mathbf{v})$ is the equilibrium part and $\widetilde{f}(\mathbf{x}, \mathbf{v}, t)$ is the perturbed term. Similarly, a linear perturbation $\widetilde{\mathbf{E}}$ in the self-induced electric field expansion, $\mathbf{E} = \mathbf{E}_0 + \widetilde{\mathbf{E}}$ with $\mathbf{E}_0 = 0$, or $\phi(\mathbf{x}, t) = \widetilde{\phi}(\mathbf{x}, t)$. It is assumed that the perturbed terms are given in the form of harmonic waves, $\widetilde{\phi},\ \widetilde{f} \sim e^{i\mathbf{k}\cdot\mathbf{x} - i\omega t}$.

Substituting Eq. (2.22) into Eq. (1.6), and integrating over the orbit characteristics, one can obtain the

kinetic equation for the perturbed distribution function $\widetilde{f}(\mathbf{x},\mathbf{v},t)$

$$\widetilde{f}(\mathbf{x},\mathbf{v},t) = -q\frac{f_{maxw}}{T}\left\{\widetilde{\phi} + i\omega\int_{-\infty}^{t} dt'\widetilde{\phi}(x',t')\right\}, \tag{2.23}$$

where x' and t' are the instantaneous orbit and the present time respectively, and $f_{maxw} = n_0\left(m/2\pi T\right)^{3/2}$ $\exp\left(-mv^2/2T\right)$ is the Maxwellian velocity distribution function (m is the particle mass, T is the particles temperature). The integral in the second term in Eq. (2.23) is called the history integral. This is, one must integrate along the moving gyro orbits form many time ago until the present time. The history integral can be represented in the following way:

$$\int_{-\infty}^{t} dt'\widetilde{\phi}(x',t') = \int_{-\infty}^{t} dt'\hat{\widetilde{\phi}}e^{i\mathbf{k}\cdot\mathbf{x}'-i\omega t'}, \tag{2.24}$$

where $\hat{\widetilde{\phi}}$ is the amplitude of $\widetilde{\phi}$ linear mode. Now, using the new variables t^* and $\mathbf{x}^*$, defined as

$$t^* = t' - t,\ \mathbf{x}^* = \mathbf{x}' - \mathbf{x}, \tag{2.25}$$

we may represent this integral as

$$\int_{-\infty}^{t} dt'\hat{\widetilde{\phi}}e^{i\mathbf{k}\cdot\mathbf{x}'-i\omega t'} = \widetilde{\phi}(x,t)\int_{-\infty}^{0} dt^* e^{i\mathbf{k}\cdot\mathbf{x}^*-i\omega t^*}. \tag{2.26}$$

Recall that the charged particle motion in presence of an applied magnetic field, as explained in Section 1.3, follows the next orbits

$$x = x_0 - \rho\left(\cos(-\omega_c t + \phi) - \cos\phi\right), \tag{2.27}$$

$$y = y_0 + \rho\left(\sin(-\omega_c t + \phi) - \sin\phi\right), \tag{2.28}$$

$$z = z_0 + v_\parallel t, \tag{2.29}$$

where $\rho = v_\perp/\omega_c$ is the gyroradius and ϕ is the gyro angle. Then, after plugging the particle coordinates into the perturbed distribution function (2.23) and taking the average over gyro angle we get:

$$\widetilde{f}(\mathbf{x},\mathbf{v},t) = -q\widetilde{\phi}\frac{f_{max}}{T}\left\{1 + \sum_{-\infty}^{\infty}\frac{\omega J_n^2\left(k_\perp v_\perp/\omega_c\right)}{n\omega_c + k_\parallel v_\parallel - \omega}\right\}, \tag{2.30}$$

where the following convenient identity of the Bessel function was used:

$$e^{\pm iZ\sin\alpha} = \sum_{-\infty}^{\infty} J_n(Z)e^{\pm in\alpha}, \tag{2.31}$$

As the goal here is to derive the Bernstein modes dispersion relation, the perturbed density $\widetilde{n}$ is found as follows

$$\widetilde{n} = \int_{-\infty}^{\infty}\widetilde{f}d^3v = \int_0^{2\pi} d\theta\int_0^{\infty} dv_\perp\int_{-\infty}^{\infty}\widetilde{f}dv_\parallel. \tag{2.32}$$

To reformulate the second term in Eq. (2.30), we use the next integral identity

$$\int_0^{\infty} 2xe^{-x^2}J_n(sx)dx = e^{-s^2/2}I_n(s^2/2), \tag{2.33}$$

where $s = v_\perp/v_T$, and I_n is the modified Bessel function. Thus, one can end up with the following expression

$$\widetilde{n}(\mathbf{x},t) = -q\widetilde{\phi}(\mathbf{x},t)\frac{n_0}{T}\left\{1 + \sum_{n=-\infty}^{\infty} I_n(b)e^{-b}\left(\frac{\omega}{k_\parallel v_T}\right)Z\left(\frac{\omega - n\omega_c}{k_\parallel v_T}\right)\right\}, \tag{2.34}$$

where $b = s^2/2 = k_\perp^2 v_T^2/2w_c^2 = k_\perp^2\rho^2/2$. Once we obtained the perturbed density we can calculate the dispersion relation. From the Poisson equation, Eq. (1.7) we have

$$\nabla\cdot\mathbf{E} = -4\pi\rho \rightarrow k^2\widetilde{\phi}^2 = 4\pi\sum_j \widetilde{n}_j q_j, \tag{2.35}$$

where the Poisson equation was linearized and converted to the Fourier space. Thereby, substituting the

perturbed density (for plasma species $j = e, i$) into the linearized Poisson equation, we end up with the electrostatic perturbed dielectric constant

$$\epsilon(\omega, \mathbf{k}) = 1 + \sum_{j=e,i} \mu^j(\omega, \mathbf{k}) = 1 + \sum_{j=e,i} \frac{1}{k^2 \lambda_{Dj}^2} \left\{ 1 + \sum_{n=-\infty}^{\infty} I_n(b_j) e^{-b_j} \left(\frac{\omega}{k_\parallel v_{Tj}} \right) Z \left(\frac{\omega - n\omega_{cj}}{k_\parallel v_{Tj}} \right) \right\}, \quad (2.36)$$

where μ^e and μ^i are the electron and ion susceptibilities, $\lambda_{Dj}^2 = T_j / 4\pi n_0 q^2$. Finally, the kinetic dispersion relation for a magnetized plasma in a constant magnetic field B_0 can be obtained as $\epsilon(\omega, \mathbf{k}) = 0$. Note that when $B_0 \to 0$ the dispersion relation becomes equivalent to the unmagnetized plasma dispersion relation

$$\epsilon(\omega, \mathbf{k}) = 1 + \sum_{j} \frac{1}{k^2 \lambda_{Dj}^2} \left\{ 1 + \frac{\omega}{k v_{Tj}} Z \left(\frac{\omega}{k v_{Tj}} \right) \right\}. \quad (2.37)$$

The major differences between the unmagnetized and magnetized dispersion relations lie in:

1) The presence of cyclotron harmonics.

2) The weighting factor of $J_n^2(k_\perp v_\perp / w_c)$, which can be expanded for a large or small argument limit, depending on the ratio $k_\perp v_\perp / w_c$, i.e., the ratio of gyroradius to the wavelength.

In the special case of taking $k_\parallel \to 0$, when waves propagate in the perpendicular direction only, $\mathbf{k} = k_\perp$, the plasma dispersion function Z in Eq. (2.36) expands as:

$$\lim_{k_\parallel \to 0} Z \left(\frac{\omega - n\omega_{cj}}{k_\parallel v_{Tj}} \right) = -\frac{k_\parallel v_{Tj}}{\omega - n\omega_{cj}}, \quad (2.38)$$

and the Eq. (2.36) becomes

$$\epsilon(\omega, \mathbf{k}) = 1 + \sum_{j} \frac{1}{k^2 \lambda_{Dj}^2} \left\{ 1 + \omega e^{-b_j} \sum_{n=-\infty}^{\infty} \frac{I_n(b_j)}{n\omega_{cj} - \omega} \right\}. \quad (2.39)$$

Note that the infinite summation in this equation can be slightly simplified as $I_n = I_{-n}$, we can split the sum as the following

$$-\frac{I_0(b_j)}{\omega} + \sum_{n=1}^{\infty} I_n(b_j) \left(\frac{1}{-n\omega_{cj} - \omega} + \frac{1}{n\omega_{cj} - \omega} \right) = -\frac{I_0(b_j)}{\omega} - \sum_{n=1}^{\infty} I_n(b_j) \frac{2\omega}{\omega^2 - n^2 \omega_{cj}^2}, \quad (2.40)$$

and the one-dimensional dispersion relation takes the form

$$\epsilon(\omega, \mathbf{k}) = 1 + \sum_{j} \frac{1}{k^2 \lambda_{Dj}^2} \left\{ 1 - I_0(b_j) e^{-b_j} - 2\omega^2 \sum_{n=1}^{\infty} \frac{I_n(b_j)}{\omega^2 - n^2 \omega_{cj}^2} \right\}. \quad (2.41)$$

Typically, in low-temperature plasma, when magnetic field is too high, the ion susceptibility μ_i can be simplified to

$$\mu_i = -\frac{\omega_{pi}^2}{\omega^2}, \quad (2.42)$$

where the cold limit $T_i \to 0$ is assumed. In this case, the dispersion relation (2.39) will describe the Bernstein modes (perpendicular to the magnetic field). If electrons are considered cold $T_e \to 0$ (which is similar to $k \to 0$), the electron susceptibility from Eq. (2.39) can be significantly simplified. Before this, the electron susceptibility can be written as

$$\mu_e = 1 + \frac{\omega_{pe}^2}{b\omega_{ce}^2} \left\{ 1 - I_0(b) e^{-b} - 2\omega^2 e^{-b} \sum_{n=1}^{\infty} \frac{I_n(b)}{\omega^2 - n^2 \omega_{ce}^2} \right\}, \quad (2.43)$$

where $b = k_\perp^2 \rho_e^2 / 2$, $\rho_e = v_{Te} / \omega_{ce}$. In the cold limit $k \to 0$ we have $b \to 0$, and $I_1(b)/b \to 1/2$, only $n = 1$ resonance is left over ($I_n(b)/b \to 0$ for $n > 1$). Also, $I_0(b) e^b = 1$, giving

$$\mu_e = 1 - \frac{\omega_{pe}^2}{\omega^2 - \omega_{ce}^2}. \quad (2.44)$$

Thus, in the cold limit the dispersion relation (2.39) simplifies to

$$1 - \frac{\omega_{pi}^2}{\omega^2} - \frac{\omega_{pe}^2}{\omega^2 - \omega_{ce}^2} = 0, \tag{2.45}$$

which is the Buneman magnetized dispersion relation. One can see that neglecting low-frequency ion component gives $\omega^2 = \omega_{pe}^2 + \omega_{ce}^2 = \omega_{uh}$, the upper hybrid frequency.

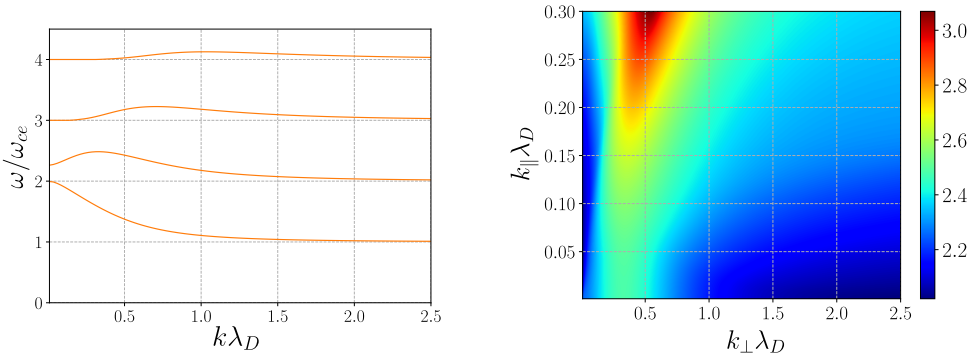

(a)

(b) Colour bar represents the ω/ω_{ce} values.

Figure 2.3: (a) One-dimensional ($k_\parallel \to 0$) and (b)two-dimensional (finite $k_\parallel$) solutions to the electron Bernstein wave dispersion relation (for $\omega_{pe}/\omega_{ce} = 2$), where ions are taken in the cold limit. The two-dimensional image demonstrates the solution for the 2^{nd} branch that starts with $\omega = \omega_{uh} \approx 2.2\omega_{ce}$.

Now, to demonstrate the behaviour of solutions for the electron Bernstein waves, we can solve the one-dimensional kinetic dispersion relation (2.41), where the ions are taken cold, μ_i given with Eq. (2.42). We choose parameters so the ratio $\omega_{pe}/\omega_{ce} = 2$. The solution in terms of ω/ω_{ce} as a function of $k\lambda_{De}$ is demonstrated in Fig. 2.3a, where the first four branches are shown. Note that the cold limit solution with $\omega = \omega_{uh}$ (when $k_\perp \to 0$) is present in the 2^{nd} branch (from below), where $\omega_{uh} \approx 2.2\omega_{ce}$. Additionally, to show the dependence on parallel wavenumber $k_\parallel$, the solution of the two-dimensional dispersion relation (2.36) (also with cold ions) is shown in Fig. 2.3b, where only this 2^{nd} branch is depicted. Note that for low values of $k_\parallel$ it does not change, and it corresponds to the previous one-dimensional solution.

2.3 Electron Cyclotron Drift Instabilities (ECDI)

The Electron Cyclotron Drift Instability is an example of a resonant instability. The ECDI happens in a plasma due to the resonance of a Doppler-shifted Bernstein mode and ion-sound wave [2]. From the previous subsection, the Bernstein modes dispersion relation was derived. The derivation of the ECDI dispersion equation is quite similar to the derivation of the Bernstein modes dispersion relation (2.36), only an equilibrium electric field is added, $\widetilde{\mathbf{E}}(\mathbf{x}, t) = \mathbf{E}_0 + \widetilde{\mathbf{E}}(\mathbf{x}, t)$, where $\mathbf{E}_0$ is the constant applied electric in the axial direction. The difference between the dispersion relations lies in the Doppler-shifted frequency $\omega \to \omega - k_y \mathbf{v}_E$ due to $\mathbf{E} \times \mathbf{B}$ electron drift velocity $\mathbf{v}_E = v_E \hat{y}$, as a consequence of the presence of the

external electric field.

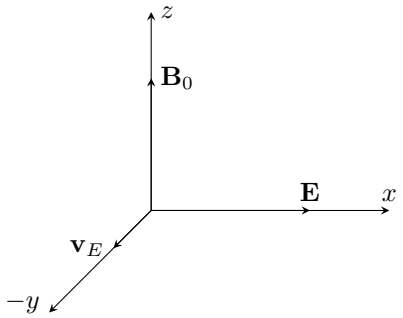

Figure 2.4: ECDI configuration with $\mathbf{B_0}$ along radial direction (z), the applied electric field $\mathbf{E}$ in axial direction (x), and the resulting drift velocity $\mathbf{v_E}$ in azimuthal direction ($-y$).

The theoretical kinetic dispersion equation that will be used for comparison with the numerical simulations is determined as follows: we consider electrostatic waves with a drift velocity $\mathbf{v_0} = \mathbf{E} \times \mathbf{B}$ streaming electrons across a uniform magnetic field $\mathbf{B}$ with unmagnetized ions. Vlasov equation for ions and electrons is written as

$$\frac{\partial f_i}{\partial t} + \mathbf{v} \cdot \frac{\partial f_i}{\partial \mathbf{x}} + \frac{q_i \mathbf{E}}{m_i} \cdot \frac{\partial f_i}{\partial \mathbf{v}} = 0, \tag{2.46}$$

$$\frac{\partial f_e}{\partial t} + \mathbf{v} \cdot \frac{\partial f_e}{\partial \mathbf{x}} + \frac{q_e}{m_e} (\mathbf{E} + \mathbf{v} \times \mathbf{B}) \cdot \frac{\partial f_e}{\partial \mathbf{v}} = 0. \tag{2.47}$$

We assume the distribution function (2.22), and seeking wavelike solutions $\widetilde{f} \sim \exp(-i(\omega t - \mathbf{k} \cdot \mathbf{x}))$. Eqs. (2.46, 2.47) in the perturbed and linear form, combined with the Poisson equation (2.4), result into the linear dispersion relation [3]

$$\epsilon(\omega, \mathbf{k}) = 1 + \mu^i(\omega, \mathbf{k}) + \mu^e(\omega, \mathbf{k}) = 0, \tag{2.48}$$

where the ions μ^i and electrons μ^e susceptibilities are

$$\mu^i = -\frac{1}{2k^2\lambda_{Di}^2} \mathrm{Z}' \left(\frac{\omega}{\sqrt{2} k v_{Ti}} \right), \tag{2.49}$$

$$\mu^e = \frac{1}{k^2 \lambda_{De}^2} \left[1 + \frac{\omega - \mathbf{k} \cdot \mathbf{v}_E}{\sqrt{2} k_z v_{Te}} \sum_{n=-\infty}^{\infty} \exp\left(-k_\perp^2 \rho_e^2\right) \mathrm{I}_n \left(k_\perp^2 \rho_e^2\right) \mathrm{Z} \left(\frac{\omega - \mathbf{k} \cdot \mathbf{v}_E + n\omega_{ce}}{\sqrt{2} k_z v_{Te}} \right) \right], \tag{2.50}$$

with $\mathrm{v}_E = |\mathbf{v}_E|$, $\lambda_{De}^2 = T_e/4\pi n_0 e^2$, $\lambda_{Di}^2 = T_i/4\pi n_0 e^2$, $v_{Te} = (2T_e/m_e)^{1/2}$, $v_{Ti} = (2T_i/m_i)^{1/2}$, $\omega_{ce} = eB/m_e c$, $\rho_e = v_{Te}/\omega_{ce}$, n_0 is the plasma density (assumed quasineutral), $Z(\xi)$ is the plasma dispersion function, $I_n(x)$ is the modified Bessel function.

In the Hall thruster device ions are effectively cold, with temperature $T_i \approx 0.1$ eV, therefore applying the condition $k v_{Ti} \ll \omega$, the derivative of the plasma dispersion function in Eq. (B.5) can be simplified as $Z'(\zeta) \approx 1/\zeta^2$, where $\zeta = \omega/\sqrt{2} k v_{Ti}$ (fluid limit, see appendix B). Then ions susceptibility becomes

$$\mu^i = -\frac{\omega_{pi}^2}{\omega^2}. \tag{2.51}$$

The ECDI is an instability as a consequence of the resonance $\omega - \mathbf{k} \cdot \mathbf{v}_E = n\omega_{ce}$.

For one-dimensional case, with $k_z \to 0$, Eq. (2.48) can be simplified by using the plasma dispersion

function $\mathrm{Z}(\xi) = 1/\xi$ ($\xi \gg 1$) for the electron component; additionally assuming cold ions, $\mathrm{Z}' \approx 1/\xi^2$, the dispersion relation corresponds to

$$1 = \frac{\omega_{pi}^2}{\omega^2} - \frac{1}{k^2\lambda_D^2}\left[1 - \exp\left(-k_y^2\rho_e^2\right)\mathrm{I}_0\left(k_y^2\rho_e^2\right) - 2\left(\omega - k_y v_E\right)^2 \sum_{m=1}^{\infty} \frac{\exp\left(-k_y^2\rho_e^2\right)\mathrm{I}_m\left(k_y^2\rho_e^2\right)}{\left(\omega - k_y v_E\right)^2 - m^2\omega_{ce}^2}\right]. \quad (2.52)$$

2.4 Cold plasma limits

A brief description of the cold plasma limits of the ECDI kinetic dispersion relation will be given here. In this limit we typically obtain dispersion relations that predict larger structures development and they can be found from the kinetic dispersion equation by taking low-wavenumber limit $\mathbf{k} \to 0$ or low-temperature limit $T \to 0$.

2.4.1 Buneman magnetized plasma instability

Plasma is formed by two or more kinds of particles moving with distinct velocities. The thermal motion of the particles reduces hydrodynamic mechanisms that drive instabilities in plasma. However, due to resonance between the particles and waves in a plasma (for high thermal values), not always the plasma evolves into a stable state. Buneman magnetized plasma instability is a current-driven instability. This instability is due to a coupling of upper hybrid mode with the short wavelength ion oscillations [12]. In the limit of cold electron temperature $T_e \to 0$ ($k_y\rho_e \ll 1$), and when higher cyclotron resonant particles effects are negligible, $(\omega - k_y v_E) > \omega_{ce}$, only the $m = 1$ contribution is accounted, the two-dimensional kinetic dispersion equation (2.48) yields to

$$1 - \frac{\omega_{pi}^2}{\omega^2} - \frac{\omega_{pe}^2 k_z^2}{(\omega - k_y v_{0e})^2 k^2} - \frac{\omega_{pe}^2 k_y^2}{((\omega - k_y v_{0e})^2 - \omega_{ce}^2)k^2} = 0, \quad (2.53)$$

which is the dispersion relation for Modified Buneman Two-Stream Instability (MBTSI). In the one-dimensional limit $k_z \to 0$, this relation takes the form

$$1 - \frac{\omega_{pi}^2}{\omega^2} - \frac{\omega_{pe}^2}{(\omega - k_y v_E)^2 - \omega_{ce}^2} = 0, \quad (2.54)$$

which is the dispersion relation for the modified Buneman instability [13].

2.4.2 Modified Two-Stream Instability (MTSI)

The Modified Two-Stream Instability (MTSI) is a fluid like, non-resonant electrostatic instability caused by the $\mathrm{E} \times \mathrm{B}$ drift between unmagnetized ions and magnetized electrons. The MTSI has a component along the magnetic field (finite k_z value) [7]. We employ the assumption $\omega - k_y v_{0e} \ll \omega_{ce}$ and we get the MTSI dispersion relation

$$1 - \frac{\omega_{pi}^2}{\omega^2} - \frac{\omega_{pe}^2 k_z^2}{(\omega - k_y v_{0e})^2 k^2} + \frac{\omega_{pe}^2 k_y^2}{\omega_{ce}^2 k^2} = 0. \quad (2.55)$$

The main difference between the MTSI and the standard Buneman instability lies in the threshold value for MTSI is $v_{0e} \gtrsim v_{Ti}$, where $v_{Ti} = \sqrt{T_i/m_i}$; while the Buneman instability threshold is $v_{0e} \gtrsim v_{Te}$, with $v_{Te} = \sqrt{T_e/m_e}$. The MTSI is known for leading an effective electron heating in parallel direction [7].

Regarding the radial-azimuthal simulations performed in this work, this heating means that radial losses most likely would be more significant during the MTSI development. Another distinct feature of the MTSI is the comparable electron and ion heating.

2.5 Numerical solutions of the kinetic dispersion relation

The dispersion relation (2.48) with simplified ions contribution (2.51) cannot be solved analytically, but numerical solutions are well studied. They are based on a fixed point iteration technique, and a detailed description of this approach is proposed in Ref. [14]. I used the same method to obtain the numerical solutions (short explanation provided below). Note that the dispersion equation is two-dimensional, where frequency ω depends on wave vector k_z and k_y. Other values that should be used for a solution include: plasma density n_0, the electron temperature T_e, applied radial magnetic field B_0, and the drift velocity v_D (calculated from the applied axial electric field E_0; the electric field here only defines the drift velocity). The numerical solution is shown in Figs. 2.5,2.6, with $n_0 = 10^{17}\,\mathrm{m}^{-3}$, $v_D = 10^6\,\mathrm{m/s}$, $\mathrm{B}_0 = 200\,\mathrm{G}$, $T_e = 10\,\mathrm{eV}$. The wavenumbers here are normalized on the $k_0 = \omega_{ce}/v_D$, an estimate for the 1^{st} cyclotron resonance mode corresponds to $k_0 v_D \approx \omega_{ce}$. The distinct cyclotron modes are shown, as well as the less pronounce MTSI mode (in low-k region). The important characteristic of this solution is that the maximum growth rate values are observed for the lowest k_z values, thus, depending on the radial length if the system allows low k_z-values, larger growth rate are expected. The "effect" of various k_z values is shown in Fig. 2.6. Low k_z-values are grouped more distinctly (with higher amplitudes), while for larger k_z values solutions are more smoothly (merged together) and with lower growth rate values. It is also important to mention that in the limit $k_z \to 0$ the MTSI mode does not exist; it requires the radial dimension. We see that for a Hall thruster configuration in radial-azimuthal domain both radial and azimuthal lengths can play a role: the radial extent can change the instability strength, while a short azimuthal length may fail to resolve the MTSI instability.

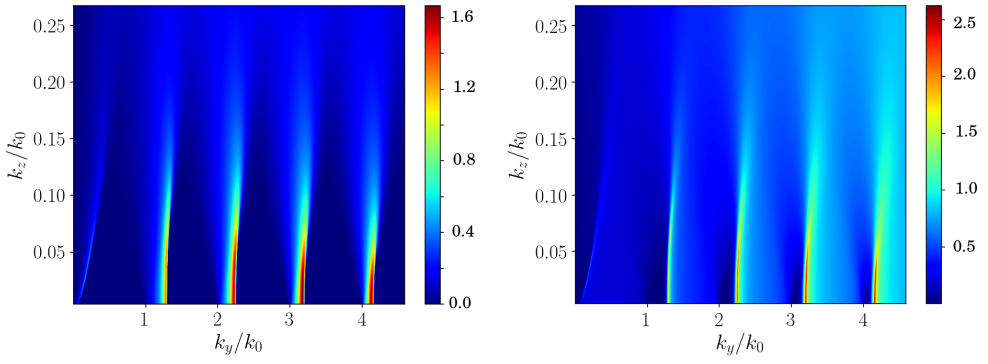

Figure 2.5: Plot of growth rate $\gamma(k_z, k_y)/\omega_{pi}$ (a) and frequency $\omega(k_z, k_y)/\omega_{pi}$ (b) for the full dispersion relation (2.48), solved numerically.

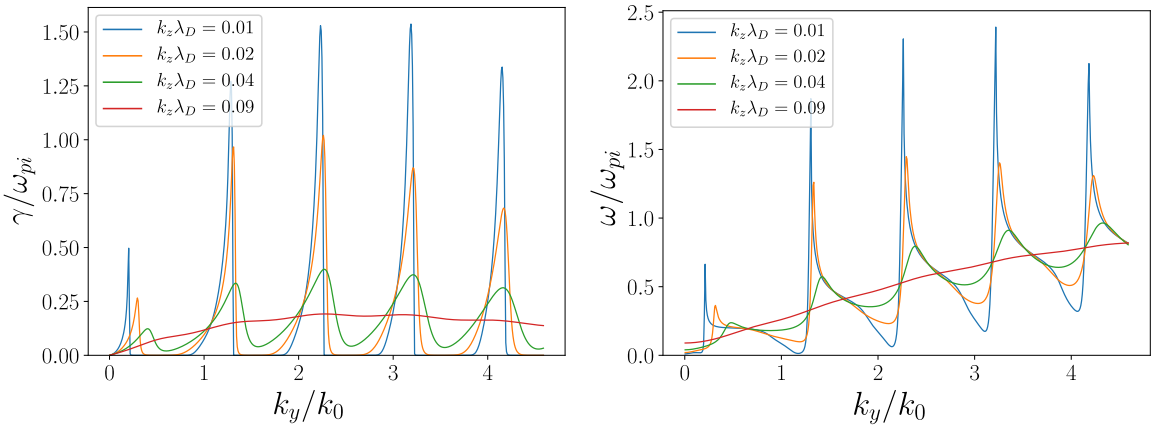

(a) Growth rate of instabilities for various k_z.

(b) Frequency for various k_z.

Figure 2.6: Numerical solution for dispersion equation (2.48) for fixed $k_z\lambda_{De}$ values, set to 0.01, 0.02, 0.04, and 0.09, respectively.

Following the procedure in Ref. [14], the ECDI dispersion relation (2.48) with the cold ions (2.51) can be represented in the form

$$1 + k^2\lambda_{De}^2 + g\left(\frac{\omega - k_y v_0}{\omega_{ce}}, k_y^2\rho_e^2, k_z^2\rho_e^2\right) - \frac{k^2\lambda_{De}^2\omega_{pi}^2}{\omega^2} = 0, \tag{2.56}$$

where $g(\Omega, X, Y)$ is the Gordeev function

$$g(\Omega, X, Y) = \frac{\Omega}{\sqrt{2Y}} e^{-X} \sum_{m=-\infty}^{\infty} \mathrm{Z}\left(\frac{\Omega - m}{\sqrt{2Y}}\right) \mathrm{I}_m(X), \tag{2.57}$$

with $\Omega = (\omega - k_y v_0)/\omega_{ce}$, $X = k_y^2\rho_e^2$, $Y = k_z^2\rho_e^2$. One can express ω from Eq. (2.56) as

$$\omega^2 = \frac{k^2\lambda_{De}^2}{1 + k^2\lambda_{De}^2 + g(\Omega, X, Y)} \equiv \mathrm{F}(\omega, k_z, k_y, ...). \tag{2.58}$$

The dispersion equation (2.48) with cold ions is written in the normalized form

$$\omega^{*2} = \frac{k^{*2}}{1 + k^{*2} + g(\Omega^*, X^*, Y^*)}, \tag{2.59}$$

where $\Omega^* = \left(\omega^* - k_y^* v_0^*\right)/\omega_{ce}^*$, $X^* = k_y^{*2} M/\omega_{ce}^*$, $Y^* = k_z^{*2} M/\omega_{ce}^*$, and $M = m_i/m_e$. All frequencies are normalized to ω_{pi}, spatial variables to λ_{De}, and thus the velocities are normalized to the ion sound velocity $c_s = (T_e/m_i)^{1/2}$. As noted in Ref. [14], the frequency ω in the right hand side (RHS) of Eq. (2.58) in the term $(\omega - kv_0)$ is low, $\omega \ll kv_0$, so the iteration process can start with the initial condition $\omega = 0$ on the RHS and obtain the next value of ω evaluating it into Eq. (2.58). In each consecutive iteration, one can substitute a new estimate for ω into the RHS until it converges (with a given tolerance).

3 Particle-in-cell modeling

3.1 General PIC algorithms

The general analytical solutions for the Vlasov-Maxwell system (1.6-1.10) using the kinetic theory of plasma are often difficult to solve. Nevertheless, development of high-performance computing allows a progress in many research areas, including kinetic plasma simulations using the PIC methods. In simple words, PIC method solves for particle trajectories that move in self-consistent electromagnetic fields. Many problems do not require induced magnetic fields (e.g., if they are negligible in comparison to existing external magnetic field), and PIC method in this approximation is called the electrostatic PIC method. In this case only the Poisson's equation (1.7) needs to be solved at every time step, then particles trajectories are updated and the process is repeated.

The common scheme of the electrostatic PIC method consists of the following steps first, loading a particle distribution and using a scatter operation that allows the extrapolation from every particle position to the grid to evaluate the number density and solve the Poisson equation. Next, a particle interpolation using a gather operation, this is, obtaining the force produced by the electric and magnetic field. Last, applying this force to the particles in order to move them (solving the particle equation of motion). This procedure is repeated at every time step.

Major parts of PIC codes are well suitable for parallelization, e.g., a particle integration procedure is an independent task. A field solver generally can also be parallelized. Output routines for highly-dimensional codes can be parallelized, as every process can write an output from its region. For realistic plasma configurations the number of simulated particles is large enough making the computational requirements arduous or impossible to achieve (typical laboratory plasma would require 10^{11} particles in 1 cm^3). For this reason one of the PIC approximations is to use macroparticles, representing a specific number of real particles, with the mass and the charge proportional to the number of particles it represents. The major steps of PIC algorithm can be shortly described as following:

1. **Compute charge density**: We compute the charge density ρ at the mesh nodes at (indexes) $X_j = j\Delta x$, $Y_k = k\Delta y$, using particle weighting, that depends on the continuous positions of the charged particle (x_i, y_i)

$$\rho_{j,k} = \rho(X_j, Y_k) = \frac{1}{\Delta V} \sum_{i}^{N_p} q_i S_{pg}(X_j - x_i) S_{pg}(Y_k - y_i), \tag{3.1}$$

where $S_{pg}(X)$ is a particle-to-mesh interpolation function, q is the particle charge, ΔV is the cell

volume, N_p is the total number of the macroparticles. Indices j, k represent the discretized spatial coordinates. Charge of the particle is distributed among the nodes of the cell where the particle is located, by any weighting [15].

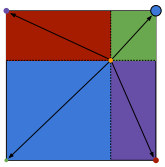

Figure 3.1: Schematic of the bilinear scatter operation on one cell.

From the exact (continuous) particles position the charge density is sampled on the grid using zero-, first-, or higher-order interpolation techniques. Typically, the first-order (linear) weighting is used as a good compromise between calculation time and accuracy; its interpolation scheme for a two-dimensional configuration (called bilinear) is illustrated in Fig. 3.1. The idea is to interpolate some value existing at the macroparticle's position indicated by the orange point to the four grids nodes. The fraction to be accumulated is given by the ratio of the area diagonally opposite (relative to the orange point) from the node to the total area $S_i = A_i/A_{tot}$.

2. **Compute electric potential**: In the same way as the charged density $\rho_{j,k}$, the electric potential is defined on spatial grid at points $X_j = j\Delta x$, $Y_k = k\Delta y$. In order to get the plasma potential, only the Poisson's equation (in two dimensions with domain $\Omega \subset \mathbb{R}^2$) is resolved due to the electrostatic approximation

$$\nabla^2\phi(x,y) = -\frac{\rho(x,y)}{\epsilon_0} \tag{3.2}$$

where the general boundary condition on the domain boundary $\partial\Omega$ has the form

$$\alpha\phi + \beta\frac{\partial\phi}{\partial n} = a \quad \text{on} \quad \partial\Omega, \tag{3.3}$$

where $\partial\phi/\partial n$ represents the rate of change normal to the boundary.

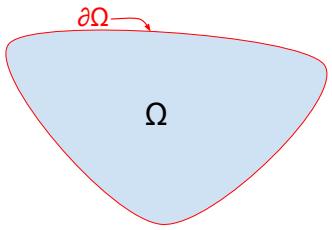

Figure 3.2: Boundary value problem.

The condition (3.3) may reduce to either Dirichlet ($\beta = 0$) or Neumann ($\alpha = 0$) boundary condition. In the finite-difference form (with three-point stencil), the Poisson's equation yields

$$\frac{(\phi_{j+1} - 2\phi_j + \phi_{j-1})_k}{(\Delta x)^2} + \frac{(\phi_{k+1} - 2\phi_k + \phi_{k-1})_j}{(\Delta y)^2} = -\frac{\rho_{(j,k)}}{\epsilon_0}. \tag{3.4}$$

There are various concerns that influence the selection of methods for the solution of the field equations. That is, the implemented methods depend on the type of the equations (linearity, dimensionality) and boundary condition; whether the region is rectangular or mixed. The equation (3.4) could be solved with distinctive methods such as the Gauss Seidel (GS)method, the successive over-relaxation (SOR) method, that belong to mesh-relaxation (iterative) methods. They are commonly used for bounded system domains.

Moreover, another group of methods are called rapid elliptic solvers based on the Fourier transform.

A good approach for the periodic systems is to use the discrete Fourier transform (DFT) for all grid quantities [15]. The most efficient algorithm for performing DFT is the fast Fourier transform (FFT). In Fourier space Poisson's equation (3.2) becomes

$$k^2\phi(\mathbf{k}) = \frac{4\pi\rho(\mathbf{k})}{\epsilon_0}, \tag{3.5}$$

$$\phi(\mathbf{k}) = \frac{4\pi\rho(\mathbf{k})}{k^2\epsilon_0}, \tag{3.6}$$

where $\rho(k)$is the charge density represented in Fourier space. The sequence for solving Poisson's equation using the discrete transform follows: in the first phase, we employ the FFT of $\rho(\mathbf{x})$ its representation in the Fourier space, $\rho(\mathbf{k})$,

$$\rho(k_x, k_y) = \Delta x \Delta y \sum_j e^{-ik_x X_j} \sum_k e^{-ik_y Y_k} \rho_{j,k}, \tag{3.7}$$

next by solving Poisson's equation (3.6) we determine the $\phi(\mathbf{x})$ values in the grid points using the inverse fast Fourier transform (IFFT),

$$\phi(x) = \frac{1}{\Delta V} \sum_{N=0}^{N_{tot}-1} \phi(k) e^{-2\pi i k n / L_x}. \tag{3.8}$$

Finally, with the $\phi(x)$values on the grid, we can evaluate the electric field $\mathbf{E}(x, y)$ in every point of the system domain.

3. **Compute electric field**: The electric field is obtained from the electrostatic potential:

$$\mathbf{E} = -\nabla\phi(x, y), \tag{3.9}$$

which yields in each direction

$$\mathrm{E}_x = -\frac{\partial\phi}{\partial x},\ \mathrm{E}_y = -\frac{\partial\phi}{\partial y}. \tag{3.10}$$

Even though the electrostatic potential may have been solved in Fourier space, its solution is transformed back to real space, and there is no necessity to solve the electric field $\mathbf{E}$ in Fourier space. One usually can use the 2^{nd} order central finite-difference scheme

$$(E_x)_{j,k} = \frac{(\phi_{j-1} - \phi_{j+1})_k}{2\Delta x}, \tag{3.11}$$

$$(E_y)_{j,k} = \frac{(\phi_{k-1} - \phi_{k+1})_j}{2\Delta y}. \tag{3.12}$$

Therefore, in order to get the electric field in the x-direction E_x it is necessary to fix the index k (y-direction). The k-index represents an integer that multiply by Δy it gives the coordinates in y-axis. The j-index represents an integer that multiply by Δx it gives the coordinates in x-axis. The electrostatic potentials with different j-index are used in this case. The same procedure remains for the electric field E_y. After the electric fields are known on the grid, it is possible to compute the force acting on every particle by interpolating its values back to the particle's position. As for the scattering operation (for evaluating charge density), the first-order interpolation scheme is widely used.

4. **Move particles**: The next step is to integrate the motion Eqs. (1.13,1.14). The numerical scheme could be explicit or implicit. One of the most popular and simple explicit second-order method is the leap-frog scheme. In this scheme, velocity is integrated through the time step firstly, and then the particle position is updated. Velocity and position integration leap over each other, being displaced by

half a time step. The finite difference scheme for the Eq. (1.14) is

$$\frac{\mathbf{v}^{t+\Delta t/2}-\mathbf{v}^{t-\Delta t/2}}{\Delta t}=\frac{q}{m}\left[\mathbf{E}+\frac{\mathbf{v}^{t+\Delta t/2}+\mathbf{v}^{t-\Delta t/2}}{2}\times\mathbf{B}\right]. \tag{3.13}$$

The method used to solve the Eq. (3.13) is to separate the electric and magnetic forces completely, named the Boris scheme, introduces $\mathbf{v}^-$ and $\mathbf{v}^+$ [15]

$$\mathbf{v}^{t-\Delta t/2}=\mathbf{v}^- -\frac{q\mathbf{E}}{m}\frac{\Delta t}{2}, \tag{3.14}$$

$$\mathbf{v}^{t+\Delta t/2}=\mathbf{v}^+ +\frac{q\mathbf{E}}{m}\frac{\Delta t}{2}, \tag{3.15}$$

If we substitute it into Eq. (3.13) the electric field $\mathbf{E}$ cancels and we end up with

$$\frac{\mathbf{v}^+-\mathbf{v}^-}{\Delta t}=\frac{q}{2m}(\mathbf{v}^++\mathbf{v}^-)\times\mathbf{B}. \tag{3.16}$$

which is only the rotation of the velocity. Formally, it can be written as

$$\mathbf{v}^+=\mathbf{v}^-+(\mathbf{v}^-+\mathbf{v}^-\times\mathbf{p}))\times\mathbf{w}, \tag{3.17}$$

where $\mathbf{p}=\mathbf{B}^t q\Delta t/2m$ and $\mathbf{w}=2\mathbf{p}/(1+p^2)$. Thus, sequentially the Boris scheme proceeds as first, using (3.14) half electric field impulse is added to $\mathbf{v}^{t-\Delta t/2}$ in order to obtain $\mathbf{v}^-$; rotating it using the Eq. (3.16) to get $\mathbf{v}^+$; and then the remaining half of the electric field impulse is added (3.15) to obtain $\mathbf{v}^{t+\Delta t/2}$ [15]. The finite difference scheme for the Eq. (1.13) is $\mathbf{x}^{t+\Delta t}=\mathbf{x}^t+\Delta t\mathbf{v}^{t+\Delta t/2}$ (leap-frog).

3.2 Numerical algorithm of the 2D3V electrostatic PIC code

The 2D3V electrostatic PIC code that has been tested and will be described in this work, allows a configuration with a rectangular domain, either periodic along the x-direction and bounded along y-direction (semi-periodic domain), or bounded in all directions. The particle load balancing involves the Message Passing Interface (MPI) processes (or CPU cores) where a domain decomposition is used. The code allows to divide the domain in different blocks or cores to apply the parallelization. The MPI computation is a sequence of communications of processes through messages. Accordingly, for instance in the code, the 2D structure of MPI processes is used to solve the Poisson's equation with the iterative successive over-relaxation (SOR) method. A brief explanation of the general PIC algorithm sequence was described above. Below, the particular discretization and specific methods used in the 2D3V code for the particle-integrator and Poisson's solver schemes are presented.

For computational purposes the following dimensionless scale values are used

$$\Delta t,\ \Delta x, v_{sc}=\frac{\Delta x}{\Delta t},\ B_{sc}=\frac{m_e}{e\Delta t},\ \Phi_{sc}=\frac{en_{sc}\Delta x^2}{\epsilon_0}. \tag{3.18}$$

With the defined scale values, we represent our variables in the dimensionless form: $\tau\equiv t/\Delta t$, $\mathbf{V}_\alpha\equiv\mathbf{v}_\alpha/v_{sc}$, $\boldsymbol{\epsilon}\equiv\mathbf{E}/E_{sc}$, $\boldsymbol{\beta}\equiv\mathbf{B}/B_{sc}$, and $\boldsymbol{\chi}\equiv\mathbf{r}_\alpha/\Delta x$. The equations of motion (1.13-1.14) are written then as

$$\frac{\partial\mathbf{V}_\alpha}{\partial\tau}=\frac{q_\alpha m_e}{em_\alpha}(\boldsymbol{\epsilon}+\mathbf{V}_\alpha\times\boldsymbol{\beta}), \tag{3.19}$$

$$\frac{\partial\boldsymbol{\chi}_\alpha}{\partial\tau}=\mathbf{V}_\alpha, \tag{3.20}$$

where α is the notation for the species type (ions or electrons). The equations (3.19-3.20) computed in finite differences are solved using the explicit Boris scheme [16]. Boris scheme for electrons in dimensionless form is described by

$$\begin{aligned} \mathbf{V}_e^- &= \mathbf{V}_e^{n-1/2} - \frac{1}{2}\boldsymbol{\epsilon}^n, \\ \mathbf{V}_e^+ - \mathbf{V}_e^- &= a_e(\mathbf{V}_e^+ + \mathbf{V}_e^-) \times \boldsymbol{\beta}, \\ \mathbf{V}_e^{n+1/2} &= \mathbf{V}_e^+ - \frac{1}{2}\boldsymbol{\epsilon}^n, \\ \boldsymbol{\chi}_e^{n+1} &= \boldsymbol{\chi}_e^n + \mathbf{V}_e^{n+1/2}. \end{aligned} \tag{3.21}$$

and the corresponding Boris scheme for ions (the s subscript denotes ion species) reads

$$\begin{aligned} \mathbf{V}_s^- &= \mathbf{V}_s^{n'-1/2} + \frac{q_s m_e}{2e m_s}\boldsymbol{\epsilon}^{n'}, \\ \mathbf{V}_s^+ - \mathbf{V}_s^- &= a_s(\mathbf{V}_s^+ + \mathbf{V}_s^-) \times \boldsymbol{\beta}, \\ \mathbf{V}_s^{n'+1/2} &= \mathbf{V}_s^+ + \frac{q_s m_e}{2e m_s}\boldsymbol{\epsilon}^{n'}, \\ \boldsymbol{\chi}_s^{n'+1} &= \boldsymbol{\chi}_s^n + N_{sub}\mathbf{V}_s^{n'+1/2}, \end{aligned} \tag{3.22}$$

with $a_e = -1/2$ and $a_s = q_s m_e N_{sub}/2e m_s$, and where N_{sub} is an odd integer that characterizes the ion subcycling period advance in time. This is, the ions are advanced every N_{sub} electron time steps (less often than electrons advance). The second equation of (3.21) and (3.22) represents rotation in the magnetic field. Its solution is

$$V_\alpha^+ = \mathbf{k}_\alpha \cdot V_\alpha^-, \tag{3.23}$$

where $\mathbf{k}_\alpha$ is the rotational matrix. Note that in this work for every simulation in Chapter 4-5, the magnitude of the magnetic field was selected in such a way that electrons are magnetized but ions are un-magnetized. The scale electron temperature, the scale electron density, the number of cells per scale Debye length N_{De}, and the maximal velocity v_{max} are used to calculate the simulation parameters, such as time-step and cell size. Thus, Δt and Δx in (3.18) are calculated from these parameters

$$\Delta x = \frac{\lambda_{De}}{N_{De}}, \tag{3.24}$$

$$\Delta t = \frac{\Delta x}{v_{max}}. \tag{3.25}$$

The 2D Poisson equation to be solved numerically is

$$\frac{\partial^2 \phi}{\partial x^2} + \frac{\partial^2 \phi}{\partial y^2} = -\rho/\epsilon_0. \tag{3.26}$$

In dimensionless variables $X \equiv x/\Delta x,\ Y = y/\Delta y$ and $F \equiv \phi/\phi_{sc}$ the equation (3.26) becomes

$$\frac{\partial^2 F}{\partial X^2} + \frac{\partial^2 F}{\partial Y^2} = -\varrho, \tag{3.27}$$

where the normalized total charge density ϱ in the grid position (X_j, Y_j) is calculated as follows

$$\varrho = \frac{1}{N_{part}} \sum_\alpha \frac{q_\alpha}{e} \sum_p f(X_{\alpha,p}, X_j) f(Y_{\alpha,p}, Y_j), \tag{3.28}$$

where f is the function that defines the weighting of the charge of each particle to the simulated grid, and we sum over all particles p of specie α.

In the semi-periodic rectangular domain, where periodic direction is along the x-direction and bounded walls along the y-direction, Eq. (3.27) is solved with a combination of spectral Fourier method and the SOR method. If we have a total points N_{tot} along the x-direction: $x_k = k\Delta x, k = 0, 1, 2, 3.., N_{tot} - 1$ and $f_k \equiv f(x_k)$. Being f a periodic function, then the inverse discrete Fourier transformations for F_k and ϱ_k are [17] (note that the Y-direction is not discretized yet and $k_n = 2\pi n/L_\theta$)

$$\begin{aligned} F_k &= \frac{1}{N_{tot}} \sum_{n=0}^{N_{tot}-1} F_n(Y) e^{-2\pi i k n/N_{tot}}, \\ \varrho_k &= \frac{1}{N_{tot}} \sum_{n=0}^{N_{tot}-1} \varrho_n(Y) e^{-2\pi i k n/N_{tot}}. \end{aligned} \tag{3.29}$$

Substituting (3.29) into the Poisson's equation (3.27) the next differential equations connecting the n-th Fourier harmonics of the potential and the charge density are obtained

$$\left[-4\pi \left(\frac{n}{N_{tot}} \right)^2 + \frac{\partial^2}{\partial Y^2} \right] F_n(Y) = -\varrho_n(Y), \quad n = 0, 1, 2, .., N_{tot} - 1 \tag{3.30}$$

Then the three-point finite-difference scheme for $\partial^2/\partial Y^2$ operator results in

$$F_{n,j-1} - \left(2 + 4\pi^2 \frac{n^2}{N_{tot^2}} \right) F_{n,j} + F_{n,j+1} = -\varrho_{n,j}. \tag{3.31}$$

The right hand side of the Eqs. (3.30-3.31) are the direct discrete Fourier transformation of the charge density

$$\varrho_{n,j} = \sum_{k=0}^{N_{tot-1}} \varrho_{k,j} e^{2\pi i k n/N_{tot}}. \tag{3.32}$$

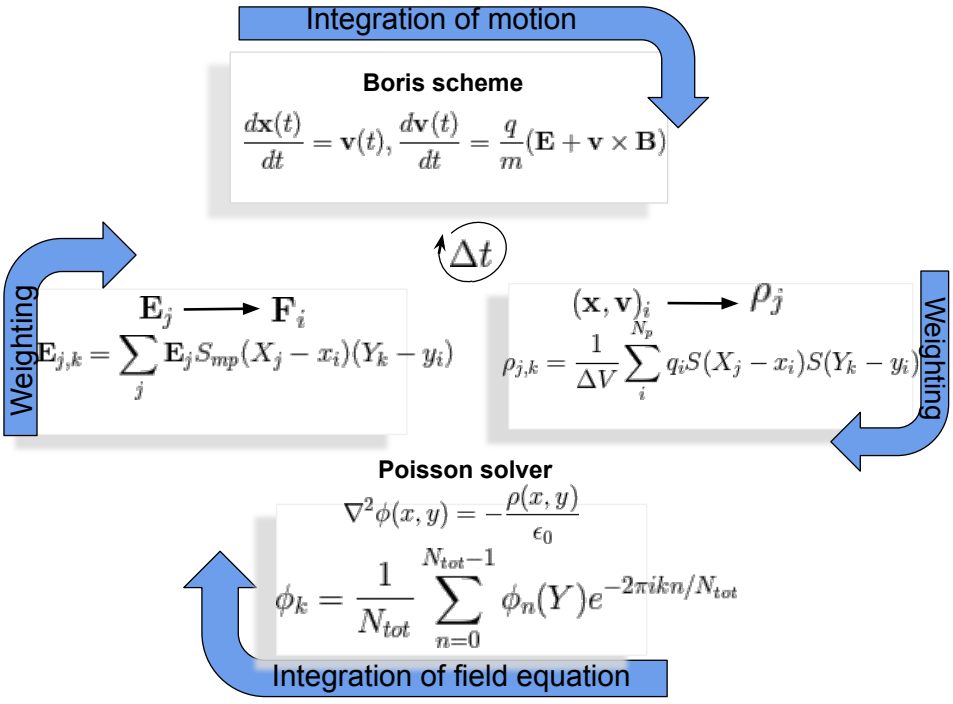

Figure 3.3: Particle-in-cell scheme.

Then Eq. (3.31) is solved for every harmonic (n) with a proper boundary condition in y-direction. The SOR method [18] is utilized for finding the unknown spectral components $F_{n,j}$ in the whole semi-periodic domain. Currently the PETSc -based solver is also added to this 2D3V code Then IFFT is used to obtain the real values of the electric potential $F_{k,j}$. The electric field is found with the second order central difference scheme (3.11-3.12).

3.3 Tests of various code subroutines

Satisfying physical constraints such as conservation of energy and momentum conservation are essentials properties for the validation of a physics code. Therefore, several testing regimes for 2D3V PIC code were performed in ascending order of complexity. My first task for this work was using this 2D3V code for testing various subroutines, during the code development by D. Sydorenko.

3.3.1 Evaluation of particle motion and drifts

Charged particle in a magnetic field moves in a circular trajectory with angular velocity Ω_c and Larmor radius r_L. In presence of magnetic field only Boris algorithm is known to save the particle's orbit, and energy error is bounded for all time-steps. Boris scheme conserves phase-space volume; that is one of the characteristics of a symplectic method. Even though the Boris algorithm is not symplectic, it has this distinctive property and its performance allows an effective scheme for the multi-scale dynamics of plasma. Fig. 3.4 just shows that the electron trajectory agrees with the analytical trajectory. I performed a test on an electron particle in the presence of magnetic field with a long period of simulation time, 30000 gyro-periods. The result is shown in Fig. 3.5, where the full trajectory is plotted; it can be seen that electron orbit is conserved, as well as the kinetic energy.

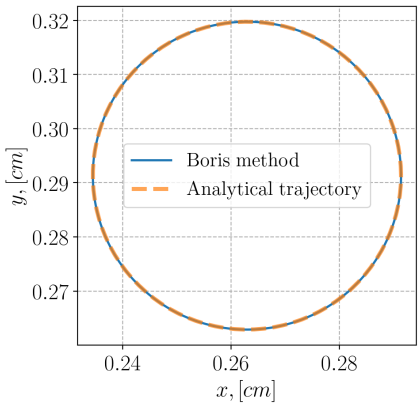

Figure 3.4: Analytical and numerical comparison for uniform magnetostatic field along z-axis, B_z = 100 G. Initial particle velocity only contains y-component, $v_y = 5 \times 10^5$ m/s, and the initial particle position is $(x_0, y_0) = (0.291, 0.291)$ cm.

Boris algorithm preserves the same orbit for the electron trajectory in an external uniform magnetic field even for a large time step. In this test the time step corresponds to $\Delta t = 0.178$ ns, which represents the

1/20 of the gyro-period. In Fig. 3.5 it is shown the kinetic energy and the particle trajectory with a static magnetic field along z-axis, $B_z = 100$ G, and initial particle position $(x_0, y_0) = (22.22, 22.22)$ cm.

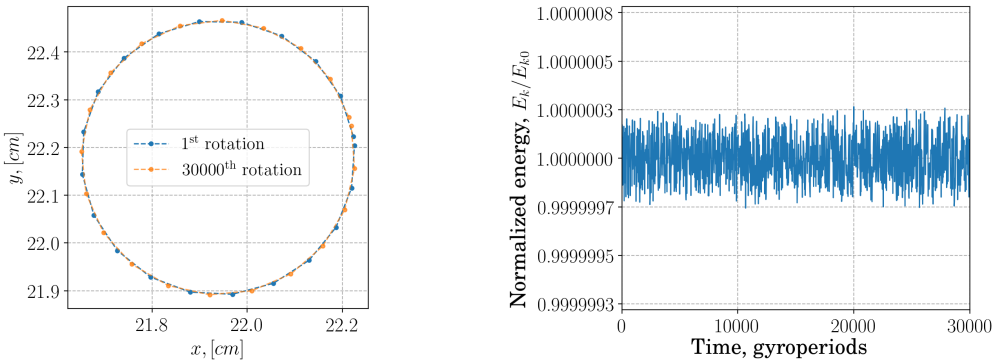

Figure 3.5: Particle trajectory (left) and kinetic energy E_k over time for electron particle (right).

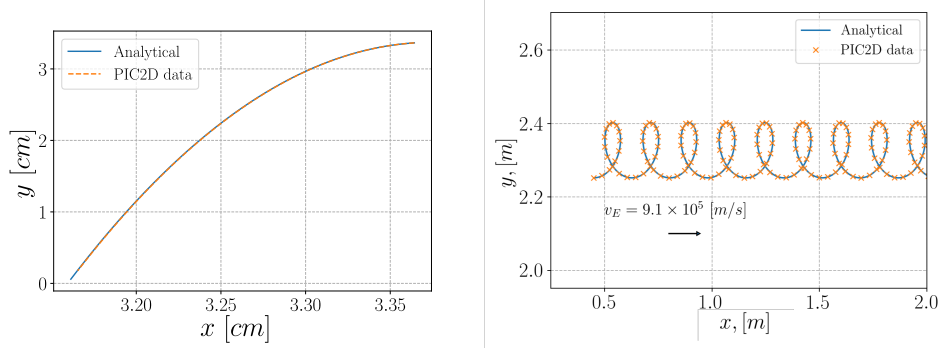

Figure 3.6: Analytical and numerical comparison in uniform electrostatic field along y-axis, $E_y = 100$ V/cm. Particle's velocity components are $v_{0x} = -3.47 \times 10^5$ m/s and $v_{0y} = -5.27 \times 10^5$ m/s. Initial particle position is $(x_0, y_0) = (3.36, 3.36)$ cm (a). **B** is along z-direction and the electric field **E** along y-direction (b).

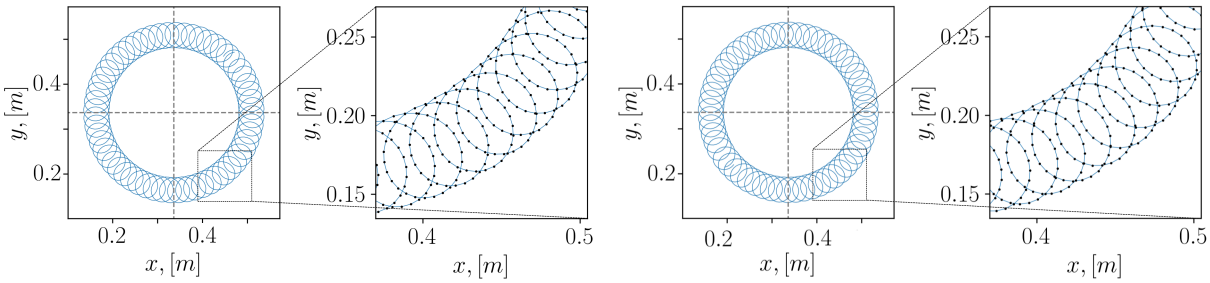

Figure 3.7: Initial (a) and final (b) particle trajectory with external radial electric field and perpendicular magnetic field (along z-direction).

From Figs. 3.7a-3.7b it is seen the $\mathbf{E} \times \mathbf{B}$ drift at the beginning and later stage of the numerical simulation, with applied radial electric field E_r, and magnetic field $\mathrm{B}_z = 150$ G along z-direction. Using one block with 512 cells in both direction. Initial velocity $v_x = -5 \times 10^8$ m/s. Initial particle position $x_0 = y_0 = 0.47$ m, system length $L = 0.67$ m.

3.3.2 Poisson equation (field solver)

Numerical solution for Poisson's equation and analytical solution of the Green's function are presented in this section. Firstly, for these tests only one particle was used in order to compare its electric potential distribution in a given system with an analytical solution of the Green's function.

Generally, when we have a linear partial differential equation such as Poisson's equation (3.26) that presents a boundary value problem, the Green's function (with localized source term) is used to obtain the full solution. Green's function $G(\mathbf{x}, \mathbf{x}_0)$ for the Poisson's equation reads

$$\nabla^2 G(\mathbf{x}, \mathbf{x}_0) = \delta(\mathbf{x} - \mathbf{x}_0), \tag{3.33}$$

where $\mathbf{x} = (x, y)$ are coordinate variables, and $\mathbf{x}_0 = (x_0, y_0)$ represents the impulse source location. Eq. 3.33 is a boundary value problem, specified in two-dimensional domain $\Omega \subset \mathbb{R}^2$ with the boundary $\partial\Omega$. The values $G(\partial\Omega)$ depend on a boundary condition type which defines its solution. Function $G(\mathbf{x}, \mathbf{x}_0)$ expresses the response at $\mathbf{x}$ coordinate as a result of impulse source at $\mathbf{x}_0$, and its solution depends on boundary conditions. The solution for an arbitrary source term (charge density) for the Poisson equation is then found by integrating (summing) over all localized solutions, using the linear property [19]

$$\phi = 4\pi \int\int \rho(\mathbf{x}_0) G(\mathbf{x}, \mathbf{x}_0) dA_0. \tag{3.34}$$

However, in our case with one particle, we assume that the charge density $\rho(\mathbf{x})$ is expressed via the delta function $\rho(\mathbf{x}) = q\ \delta(\mathbf{x})$, therefore only Green's function solution is necessary to compute a solution for the Poisson equation. For the analytical solution of Green's function with all metal walls boundaries I used a direct solution (3.35) while for the analytical solution of Green's function in semi-periodic boundaries, I employed Fourier series to compute my solution.

In the case with all metal walls, we have to solve the Eq. (3.33) with the Dirichlet boundary conditions, $G(0, 0) = G(L_x, L_y) = 0$ (or arbitrary constant). One can obtain the following direct solution of Green's function [19]

$$G(\mathbf{x}, \mathbf{x}_0) = \sum_{n=1}^{\infty} \frac{2 \sin \pi n x_0 / L_x \sin \pi n x / L_x}{n\pi \sinh \pi n L_y / L_x} \begin{cases} \sinh \dfrac{\pi n (y_0 - L_y)}{L_x} \sinh \dfrac{\pi n y}{L_x}, & y < y_0, \\ \sinh \dfrac{\pi n (y - L_y)}{L_x} \sinh \dfrac{\pi n y_0}{L_x}, & y > y_0. \end{cases} \tag{3.35}$$

On the other hand, the Poisson equation for a charged particle that is placed in $\boldsymbol{x}_0 = (x_0, y_0)$ corresponds to

$$\nabla^2 \phi(\boldsymbol{x}, \boldsymbol{x}_0) = 4\pi Q \delta(\boldsymbol{x} - \boldsymbol{x}_0). \tag{3.36}$$

Therefore, to obtain the electric potential, the solution of Green's function needs to be multiplied by a constant $4\pi Q$ to be scaled in Statvolts, or by Q/ε_0 to be scaled in Volts, where Q is the macroparticle charge. In my case it is scaled in Volts.

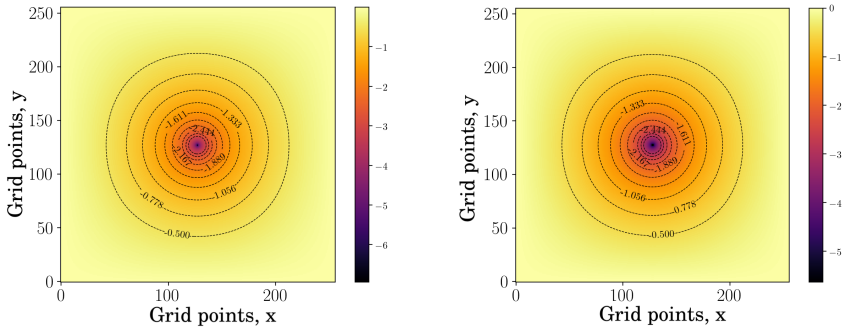

(a) (b)

Figure 3.8: (a) Equipotential field (in Volts) found from numerical solution (b) analytical solution from Green's function, with Dirichlet boundary conditions for a rectangular domain using Eq. (3.35).

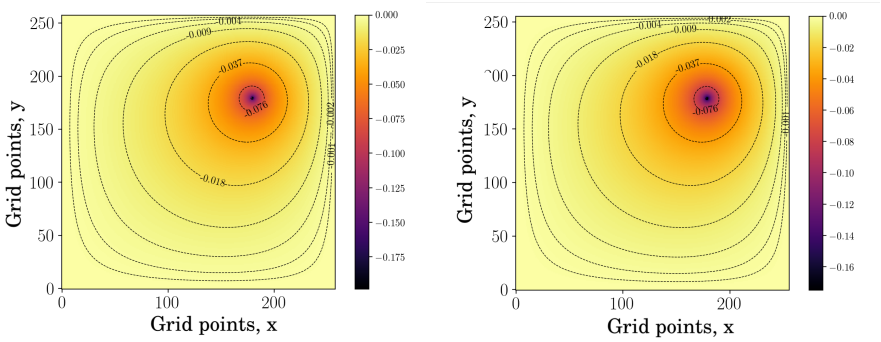

(a) (b)

Figure 3.9: (a) Equipotential field (in Volts) found form numerical solution, with all metal walls boundary condition. (b) analytical solution form the Green's function with Dirichlet boundary conditions for a rectangular domain using Eq. (3.35).

The potential distribution with equipotential lines due to the particle-wall interaction, in a configuration with all metal walls boundary condition is shown in Figs. 3.8a, 3.9a. I compare this result with the analytical solution of Green's function for the Dirichlet boundary conditions, given by Eq. (3.35). The analytical plots are presented in Figs. 3.8b, 3.9b.

Now I would like to obtain the solution for the Green's function (3.33) for the semi-periodic domain, with the Dirichlet boundary condition in y-direction ($G(x,0) = G(x,L_y) = 0$) and periodic in x-direction ($G(x,y) = G(x+L_x,y)$). We seek a solution in the following form

$$G(x,y,x_0,y_0) = \sum_{n=0}^{\infty} G_{1n}(y,x_0,y_0)\cos(2\pi nx/L_x) + G_{2n}(y,x_0,y_0)\sin(2\pi nx/L_x), \tag{3.37}$$

where functions G_{1n}, G_{2n} needs to be evaluated. Note that the Eq. (3.37) satisfy the periodic boundary

condition in x. Substituting it into the Eq. (3.33) with $k_n = 2\pi n/L_x$, we get

$$\sum_{n=0}^{\infty}\left(\frac{\mathrm{d}^2 G_{1n}}{\mathrm{d}y^2} - \left(\frac{2\pi n}{L_x}\right)^2 G_{1n}\right)\cos k_n x + \left(\frac{\mathrm{d}^2 G_{2n}}{\mathrm{d}y^2} - \left(\frac{2\pi n}{L_x}\right)^2 G_{2n}\right)\sin k_n x = \delta(\mathbf{x}-\mathbf{x}_0). \tag{3.38}$$

Multiplying the equation above on $\cos(2\pi m x/L_x)$, where $m \in \mathbb{N}$, and integrating over x (orthogonality property) we obtain

$$\frac{\mathrm{d}^2 G_{1m}}{\mathrm{d}y^2} - \left(\frac{2\pi m}{L_x}\right)^2 G_{1m} = \frac{2}{L_x}\cos(k_m x_0)\delta(y-y_0). \tag{3.39}$$

Then similarly, multiplying the equation (3.38) on $\sin(2\pi m x/L_x)$, where $m \in \mathbb{N}$, and integrating over x (orthogonality property)

$$\frac{\mathrm{d}^2 G_{2m}}{\mathrm{d}y^2} - \left(\frac{2\pi m}{L_x}\right)^2 G_{2m} = \frac{2}{L_x}\sin(k_m x_0)\delta(y-y_0). \tag{3.40}$$

Those equations need to be solved with the Dirichlet boundary conditions $G_{1m}(0) = G_{1m}(L_y) = 0$, $G_{2m}(0) = G_{2m}(L_y) = 0$. They can be found in the form

$$G_{1m} = \sum_{k=1}^{\infty} c_{1mk}\sin\left(\pi k y/L_y\right), \tag{3.41}$$

$$G_{2m} = \sum_{k=1}^{\infty} c_{2mk}\sin\left(\pi k y/L_y\right), \tag{3.42}$$

which automatically satisfy the boundary conditions. Substituting Eq. (3.41) into Eq. (3.39), we obtain

$$\sum_{k=1}^{\infty}\left[-c_{1mk}\left(\frac{\pi k}{L_y}\right)^2 - c_{1mk}\left(\frac{2\pi m}{L_x}\right)^2\right]\sin\left(\pi k y/L_y\right) = \frac{2}{L_x}\delta(y-y_0)\cos(2\pi m x_0/L_y), \tag{3.43}$$

which we can simplify using the orthogonality property for the sin function, i.e., multiply the Eq. (3.43) on $\sin\left(\pi l y/L_y\right)$, and integrating it from 0 to L_y,

$$-\left(\frac{\pi l}{L_y}\right)^2 c_{1ml} - \left(\frac{2\pi m}{L_x}\right)^2 c_{1ml} = \frac{4}{L_y L_x}\sin(\pi l y_0/L_y)\cos(2\pi m x_0/L_y), \tag{3.44}$$

$$c_{1ml} = \frac{-4}{L_x L_y}\frac{\sin(\pi l y_0/L_y)\cos(2\pi m x_0/L_x)}{\left(\frac{\pi l}{L_y}\right)^2 + \left(\frac{2\pi m}{L_x}\right)^2}. \tag{3.45}$$

In the same way I proceed for c_{2ml}. Substituting Eq. (3.42) into Eq. (3.40) we obtain

$$c_{2ml} = \frac{-4}{L_x L_y}\frac{\sin(\pi l y_0/L_y)\sin(2\pi m x_0/L_x)}{\left(\frac{\pi l}{L_y}\right)^2 + \left(\frac{2\pi m}{L_x}\right)^2}. \tag{3.46}$$

Finally, the solution for the semi-periodic problem will have the form

$$\begin{aligned} G(x,y,x_0,y_0) \quad = \quad & \sum_{m=0}^{\infty}\sum_{l=1}^{\infty} c_{1lm}\sin\left(\pi l y/L_y\right)\cos(2\pi m x/L_x) + \\ & c_{2lm}\sin\left(\pi l y/L_y\right)\sin(2\pi m x/L_x). \end{aligned} \tag{3.47}$$

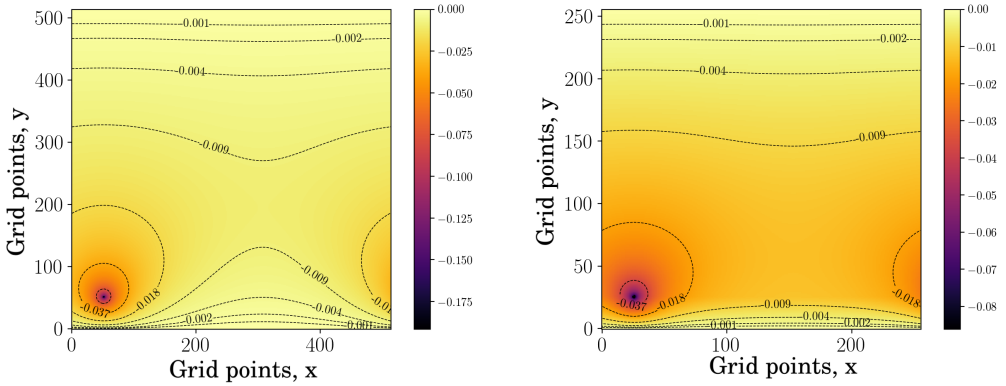

(a) (b)

Figure 3.10: (a) Potential distribution with the equipotential lines (particle coordinates: $x = 0.1\ L_x$, $y = 0.1\ L_y$), x-direction is periodic and metallic walls in y-direction. (b) Solution of the Green's function with semi-periodic boundary conditions for a rectangular domain using Eq. (3.47).

3.3.3 Parallelization using MPI

Parallelization for modern PIC codes is de-facto a necessity to achieve highly resolved calculations, e.g., reduced numerical noise can be achieved with a large number of macroparticles. Luckily, PIC algorithms are well suitable for an efficient parallelization due to its main internal computational steps, i.e., particles phase-space integration in time and solving for electromagnetic fields. Particle integrator performs time integration for each macroparticle independently, thus allowing a capable parallel implementation. A field solver, depending on configuration and numerical approach used, generally allows parallel implementation, for example via the domain decomposition etc.

The 2D3V PIC code is parallelized with the Massage Passing Interface (MPI) library which allows to run programs using the distributed memory system (e.g., large supercomputers with thousand of cores). In general, the MPI is the communication standard with the defined massage-passing operations that have various implementations, for example OpenMPI, MPICH, etc; they provide an applications programming interface (API) for a user and support C, C++, and FORTRAN languages. The MPI parallelized code could be run efficiently with an arbitrary number of processors, depending on problem size and configuration. [20]. Originally MPI was developed for programming the distributed-memory systems. It is an architecture where each processor (core) has its own memory, and thus it can operate on local data only; whenever remote data is required, some communication (sending messages) is used to access other processors data. In contrast, in shared-memory systems cores has equal access to some common memory space. Modern MPI implementations support both of these architectures as well as other and can be used on a wide variety of parallel computing architectures. A basic API in MPI provides the "send" and "receive" functions, that allow processes to communicate with each other, identifying by ranks (a unique number) in the range 0—$N_p - 1$, where N_p is the total number of processes involved in a given parallel run.

A simulation input data files are read by all processors, but the processor with rank 0 (so-called server processor) performs initial distribution over velocity space as well as a uniform distribution over coordinate space [21]. When simulation evolves in time, it is important for overall parallel efficiency to ensure that all processors operate on roughly the same number of macroparticles, thus the so-called load balancing algorithm is implemented. If simple domain decomposition would be utilized, where physical space is equally split between all processors, the latter would only have about an equal number of macroparticles initially, and later in the simulation due to inhomogeneities they would be more likely loaded with significantly different number of macroparticles. It is inefficient, therefore a load balancing technique is used. Here it is implemented with the larger scale regions in space, named clusters. All domain is equally divided to some number of clusters N_{cluster}, such that $N_{\text{cluster}} \ll N_p$. For each cluster, a master process is assigned and its task is to distribute macroparticles within clusters domain between other processes. Thus, all other processes are used as macroparticle integrators, and their number is $N_p N_{\text{cluster}}$. They can be assigned to any cluster, and all processors that assigned to one cluster (including master process) are performing macroparticle integration within the domain of this cluster. The number of processors assigned for a cluster is proportional to the total number of macroparticles in this cluster, thus load balancing is achieved.

Here I provide a short study of the parallel performance of the 2D3V code, starting with the corresponding definitions. The common measures are the speedup and the efficiency. The speedup S is defined as the ratio of time required by the serial (one processor) program T_s to the time spent by a parallel program T_p (using some number of processors p), executing the amount of tasks . Ideally, the speedup factor increases with p linearly, i.e. if its run-time $T_p = T_s/p$, then the speedup is $S \equiv T_s/T_p = p$. In reality, this can be observed for a large problems and small number of processors. However, as more processors are used, the increase in communication time reduces the speedup factor from the linear relationship. Another measure is the efficiency E, defined as the ratio of the speedup to a number of processors, $E \equiv S/p$. In other words, when the speedup do not increase linearly with p, the efficiency decreases, i.e. we are not utilizing every processor with 100% efficiency. This happens naturally for most of parallel implementations, efficiency decreases with p (for a fixed problem size N). To increase the efficiency for a given p, one can increase the system size N. Here comes the notion of the parallel scalability: the system is called scalable if increasing both p and N (proportionally) keeps the efficiency about the same, and non-scalable if this leads to drop in the efficiency. Note that the proportion in which one increases the number of processors and the problem size here may not be the same. A ratio of these numbers can be evaluated for a parallel program and then used to characterize how good is the scalability [22].

Below a few tests are performed with 2D3V code to demonstrate the parallel performance. The problem size N here is associated with the number of particles (system size, i.e. number of grid points plays a lesser role), therefore the number of macroparticles per cell N_{ppc} is used for defining the problem size. Scalability in terms of the speedup factor is demonstrated in Fig. 3.11a, where the problem size was kept fixed (800 particle per cell and 1024×1024 cells). With the number of processors increasing, communication

time increase and we do not get ideal speedup, it starts to saturate as expected. The corresponding efficiency measurements are in Fig. 3.11b, supporting this observation.

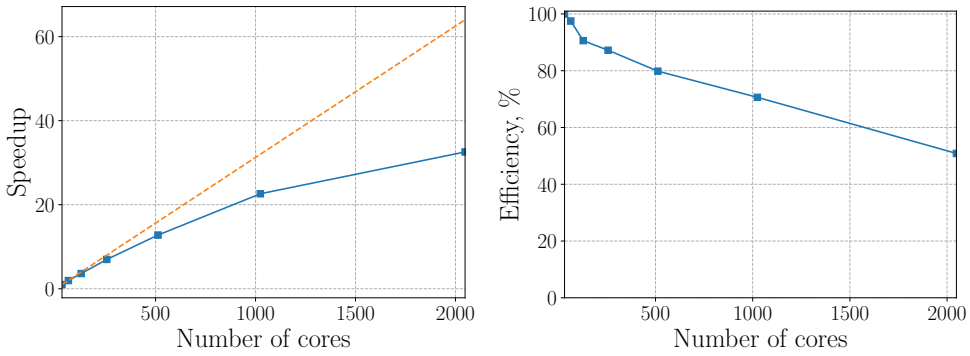

(a) **(b)**

Figure 3.11: Speedup evaluation (a), efficiency (b))

Table 3.1: Parallel scalability for varied problem size, shows time spent (min.) per 10^6 macroparticles. Number of processors is kept the same, 512.

Particles/cell	time, T (min)	t= T/part/cell (min)
400	5201	13
800	6765	8.46
1600	14635	9.15

Next, when the number of processors is kept the same ($p = 512$) but problem size varied, Tab. 3.1 shows that the time (per problem size) is the maximum for a small problem size, e.g. it is not that efficient to solve relatively small problem with a lot of processors. The best value is found for $N_{ppc} = 800$, and it is close for $N_{ppc} = 1600$.

Finally, the scalability was tested when both problem size and the number of processors were increased in the same proportion, Tab. 3.2. As mentioned above, if the efficiency stays the same during this procedure, it suggest a good overall scalability. In our case we observe a sharp drop from a small problem size, with 89% efficiency, to the values of about 55-65% for the larger problems. For these larger problems, $N_{ppc} = (200, 400, 800)$, the efficiency stays about the same, which suggest a good scalability up to these problem sizes.

Table 3.2: Parallel scalability test for increasing both the problem size and the number of processors in a linear proportion.

Particles/cell	Number of cores	time (min)	E, %
100	32	40.05	89
200	64	58.65	54
400	128	62.67	53
800	256	59.87	66
1600	512	60.57	n/a
3200	1024	80.92	n/a

4 Nonlinear development of ECDI, MTSI, and anomalous transport

Partially magnetized plasma with $\mathbf{E} \times \mathbf{B}$ configuration in devices like Hall thruster is subject to numerous instabilities. The anomalous transport (perpendicular to the magnetic field) in Hall thrusters is one of the most discussed topics. It is usually found that this transport is orders of magnitude larger than the classical (collisional) theory predicts. The cyclotron instability driven by $\mathbf{E} \times \mathbf{B}$ electron current in azimuthal direction is one of the possible reasons for developing of the anomalous transport. The ECDI instability was studied earlier in 1D configuration [23–25], 2D axial-azimuthal [26,27], and 2D radial-azimuthal configurations [12,28,29]. In this Chapter, I used the 2D3V PIC code for modeling the linear modes/waves and nonlinear instabilities in azimuthal-radial (r, θ)-plane of a Hall thruster for a simplified rectangular geometry, see Fig. 4.1. This two-dimensional setup allows to evaluate the axial current due to the evolution of all three velocity components. I will use these measurements to study the electron axial (anomalous) current. The region of interest is (r, θ)-plane near the channel exit where the strong electric field ($\sim$ 20 kV/m) creates a significant electron $\mathbf{E} \times \mathbf{B}$ drift ($\sim 10^3$ km/s). The typical magnetic field at the channel exit is $\sim$ 200 G, so the ions are effectively unmagnetized. We choose θ- and r-direction along the simulation x- and y-axis, respectively (x-direction is periodic, y-direction is bounded, either metal or dielectric wall). Typical Hall thruster plasma parameters are used for the initial state. The kinetic dispersion equation that will be used for comparison with the simulations is determined as follows: we consider electrostatic waves with $\mathbf{v_0} = \mathbf{E} \times \mathbf{B}$ streaming electrons across a uniform magnetic field $\mathbf{B}$ with unmagnetized ions. This is, using the general dispersion equation (2.11) and the respective electron and ion susceptibilities Eqs. (2.49,2.50).

The performed kinetic plasma simulations in this work differ from each other either in applied magnetic and/or electric field magnitudes, boundary conditions, initial plasma density, or system length. For a better/easier representation, based on the boundary conditions in radial direction, simulations are divided in two main classes: D-dielectric and M-metal. Each class contains a general case as a reference case, with a specific initial conditions and parameters to be compared with the rest of the cases. For simplicity, I will refer the main/general case to be "MRUN-1", using metal walls. The second general case, "DRUN-1", corresponds to the variation of the boundary condition, using dielectric walls instead of metal walls. Note, that in both metal and dielectric boundary conditions, particles are absorbed (lost) on the wall. All other simulations represent a change in one or two plasma parameters or system length. Thus, they are grouped in the following way

- Group A – varying the system length.

- Group B – varying the plasma density.
- Group C – varying the electric field E magnitude.
- Group D – varying the magnetic field B magnitude.
- Group E – varying both the electric field E and the magnetic field B magnitude.

Hence, each run name is combined from the class name and the group name. For instance, the MRUN-A2 simulation corresponds to the simulation using metal walls and varying the radial length. Additionally, one more simulation was added, with the reflecting boundary conditions for particles and metal boundary conditions for electrostatic potential ($\phi(0) = \phi(L_r) = 0$), named REF-1. The purpose of this last case was to address the problem of plasma losses with time (there is no particle source in simulations in this Chapter), its effect on values of the anomalous electron current. It was found that there is an increase in the value of the axial electron current when the particles are reflected back into the simulation once they approach the metal walls.

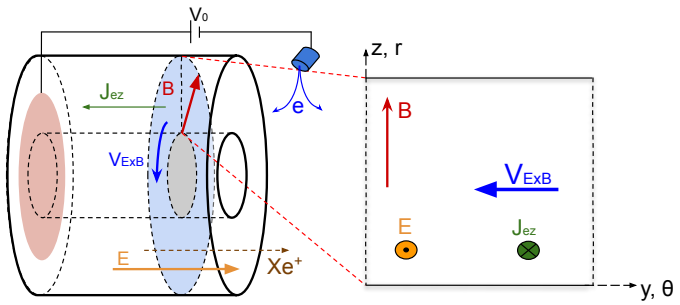

Figure 4.1: Schematic representation for the proposed simulation setup; x-direction for azimuthal coordinate (periodic), y-direction for radial (bounded).

4.1 Azimuthal-radial simulations bounded by metal walls in the radial direction

In this section the results for various runs with radial direction bounded with two metal walls with an imposed potential, $\phi\,(r = 0, \theta) = \phi\,(r = L_r, \theta) = 0$ V, are discussed. The particles are lost upon reaching the radial walls, which we call absorbing boundary conditions. The general case named MRUN-1, using metal walls as the boundary condition in the radial direction and with system size $L_{\theta 1} = 2$ cm, $L_{r1} = 2$ cm, will be taken as the reference case. Some of the main plots/descriptions provided are: temporal electron density profile, the evolution of the electron anomalous current, the electric field, electron temperature, in addition with the evolution of the ECDI and the MTSI modes. Consequently, these results/outputs will be analyzed and compared in Section 4.3. As mentioned previously, the main goal of this thesis work is the investigation on the evolution of ECDI and others possible non-linear instabilities in plasma, by varying some external parameters. Correspondingly, to associate possible candidates that could cause the electron

anomalous current in such plasma configurations.

4.1.1 MRUN-1 (general case): azimuthal length, $L_{\theta 1} = 2$ cm, radial length, $L_{r1} = 2$ cm

For this case I provide a detailed description of the physical phenomena, calculations, and analysis for this configuration. Regarding the other runs in this Chapter, we will have very similar physics (just some changes in simulations parameters), therefore less description for figures/output will be given. Table 4.1 refers to the numerical and plasma parameters for the general run. In all next simulations in this Chapter, the following numerical parameters remain the same: time step, cell size, and the number of particles per cell.

Table 4.1: Simulation parameters for the general case

Parameter	Value
Plasma density, n_0	10^{17} m^{-3}
External magnetic field **B**,	200 G
External electric field **E**,	200 V/cm
Cell size, Δx	1.954×10^{-3} m
$\lambda_D/\Delta x$	8
Time step, Δt	1.168×10^{-12} s
Number of cells in x	1024
Number of cells in y	1024
Azimuthal length, L_θ	2.0 cm
Radial length, L_r	2.0 cm
Number of particles per cell	800

I will often use the wavenumber k_0 for a normalization purpose, which is defined as $k_0 = \omega_{ce}/V_D$, and it corresponds to the 1$^{\text{st}}$ cyclotron resonance $k_0 V_D \approx \omega_{ce}$. Given the system length in the simulation, the resolved finite wavenumbers in the radial direction are defined as $k_{z,n}/k_0 = \pi n/L_r k_0 = [0.022372, \ldots, 22.887]$ with the step $\Delta k/k_0 = 0.022372$. The resolved wavenumbers in θ-direction are $k_y/k_0 = 2\pi n/L_\theta k_0 = [0.089488, \ldots, 45.729]$ with the step $\Delta k/k_0 = 0.089488$. It was observed that unstable structures are formed in azimuthal direction. Therefore, the growth rates for various wavenumbers (including the lowest and first cyclotron modes) are found from the discrete Fourier transform for the electric potential in azimuthal direction $\phi(x) = \phi(\theta, r = L_r/2)$. The DFT for the electric potential is written as

$$\phi_k = \frac{1}{N} \sum_{n=1}^{N-1} \phi_n e^{-ikn/N}, \quad k = 1, \ldots, N/2 \tag{4.1}$$

where $\phi_n = \phi(x_n)$ is discretized electrostatic potential, N - number of points in azimuthal direction, k is the discrete wavenumber. The spectral density $|\phi_k|^2$ is plotted in Fig. 4.2a as a function of time for the selected wavenumbers. The actual DFT transform was performed with FFT algorithm, using Python's Numpy library [30]. The growth rates γ for specified wavenumbers values are found (fitted lines $y = 2\gamma t + c$ in logarithmic plot) in the linear stage of the simulation. The growth rates for the first four cyclotron modes

are $\gamma_1 = 1.478$, $\gamma_2 = 1.496$, $\gamma_3 = 1.354$, $\gamma_4 = 1.624$, respectively (γ is normalized on ω_{pi}). Also, we note the growth of the small wavenumber $k = 0.357k_0$, that starts after cyclotron modes saturation, with the growth rate $\gamma_0 = 0.311$; this value is consistent with the solution of full dispersion equation, and this mode corresponds to the MTSI. In the linear stage we did not observe any structural formations in the radial direction, so we can assume that the wavenumber k_z has it lowest possible value, $k_z = \pi/L_r$. For our system it corresponds to $k_z\lambda_{De} = 0.01167$, Fig. 4.2b shows the solution of the dispersion equation (2.48) in this case, together with the growth rates calculated from the simulation. Accordingly, it can be seen that the most unstable wavenumbers appear in the simulation, in a full agreement with the dispersion equation. It is shown in Fig. 4.2a that the first ECDI mode saturates at approximately 160 ns, and it dominates during the whole simulation. The MTSI mode starts to growth after the ECDI modes saturate, and MTSI itself saturates at ~ 450 ns.

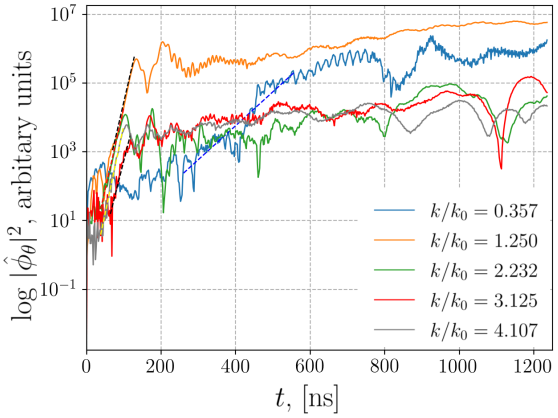

(a) Logarithmic amplitude of the azimuthal electric potential energy $|\phi_\theta|^2$.

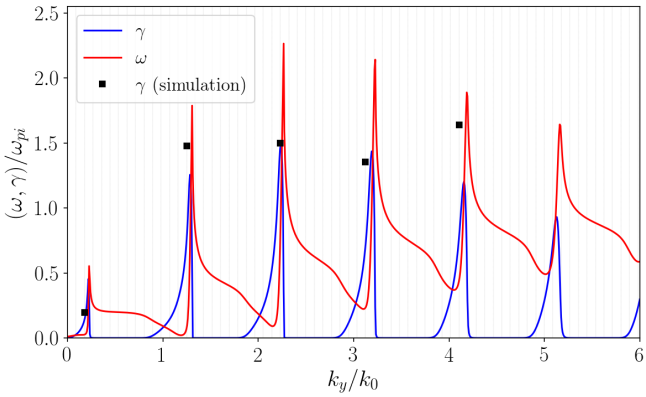

(b) Growth rate and frequencies for $k_z\lambda_{De} = 0.011$. Vertical grid lines shows the spectral resolution in azimuthal direction for a given simulation setup.

Figure 4.2: Linear growth and nonlinear saturation of the cyclotron and MTSI modes. The different dashed lines represent the respective functions $y = 2\gamma t + c$ (found by linear regression) for the first cyclotron modes; as well as for the low-k MTSI mode.

Two-dimensional power spectrum of the azimuthal electrostatic potential (in time and fixed $L_r = 1\,\text{cm}$) is shown in Fig. 4.3. A number of cyclotron (ECDI) modes can be clearly distinguished along with the lower frequency (low-k) MTSI mode. One can note that the dominate mode corresponds to the first cyclotron mode as exhibit in Fig. 4.2a. Nonlinear evolution of the electrostatic potential is presented in Figs. 4.4. For a better representation of the developed structures, these plots show the fluctuating (perturbed) variable $\widetilde{x}$, calculated as: $\widetilde{x} = x - \langle x \rangle$,

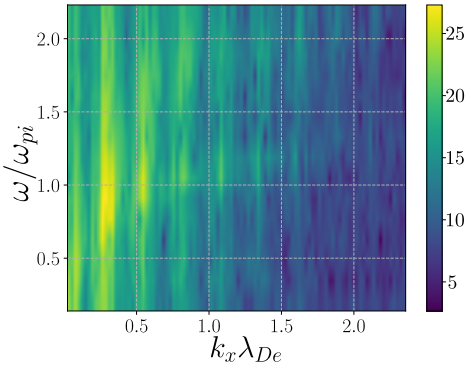

Figure 4.3: 2D FFT of the azimuthal electric potential at fixed radial position 1 cm. System size $L_\theta = 2$ cm and $L_r = 2$ cm.

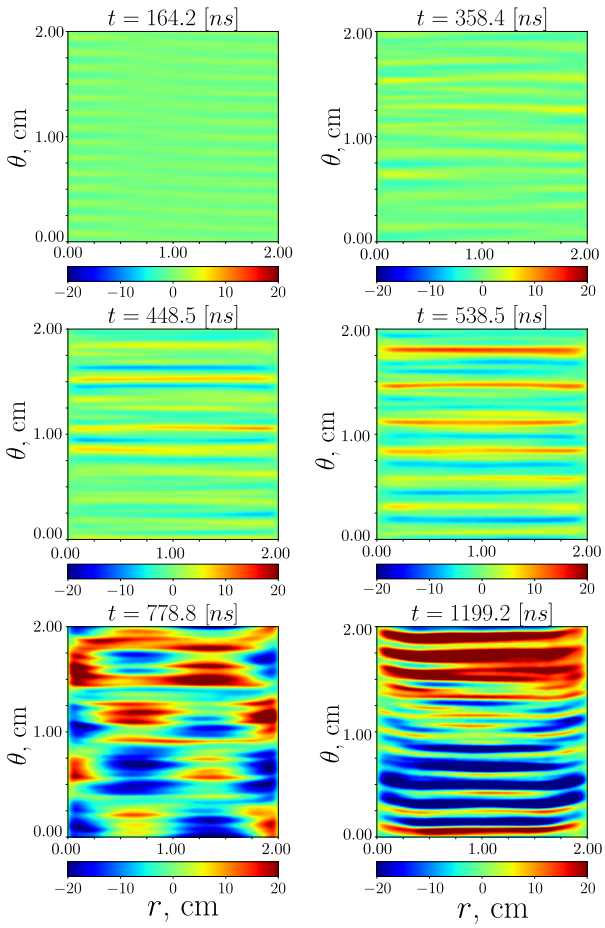

Figure 4.4: Nonlinear evolution of electrostatic potential fluctuations $\widetilde{\phi}$ in time.

where $\langle x \rangle$ is the average along θ-direction for every radial point r. It is seen that early in the nonlinear stage ECDI dominates, while, the MTSI gives some radial patterns when it reaches higher values (after its saturation). Even though the first ECDI mode is more prominent, the MTSI mode gains energy and gets closer values to the ECDI mode. Thus, a distorted image is observed by the end of the simulation and the wavelength structure in radial direction corresponds to the half system length.

Next, the analysis of the electron axial current (later referred as the anomalous current) is provided. In the previous Chapter 1, the expression to calculate the electron current J_z was given (analytically) by Eq. (1.40) as a function of space and time. The current J_z was evaluated from the simulation accordingly from the phase space particle representation. For a quantitative calculation, the axial electron current from the simulation is averaged over the whole domain (x, y) which leaves it as a function of time only

$$\langle J_z \rangle_{x,y} = q_e \langle n_e V_z \rangle_{x,y}. \tag{4.2}$$

This averaged current density is plotted in Fig. 4.5a (in blue). What can be a cause of this axial current? The most obvious candidate is the fluctuating azimuthal electric field that develops during the nonlinear instability. High enough values of this electric field can push electrons into the axial direction due to $E \times B$ force. Indeed, it is found that this current is due to the $E_x \times B$ drift. The current $J_{E_x \times B}$ can be evaluated as

$$J_{E_x \times B} = q_e \frac{\langle n_e E_x \rangle}{B_y}, \tag{4.3}$$

and it is shown in Fig. 4.5a (orange). The comparison between the mean electron current density $\langle J_z \rangle_{x,y}$ and the current $J_{E_x \times B}$ demonstrates a good agreement between each other. In Fig. 4.6a can be seen that the electron density decreases over time due to radial losses and absence of any particle source in the simulation. Fig. 4.6b shows the time evolution of the electron density azimuthal k-spectra with fixed radial coordinate $L_r/2$. Similarly to the electron anomalous current spectra, we observe the energy cascades to the long wavelengths modes. The difference is that the lowest k-mode here do not correspond to the lowest available k_y in the system.

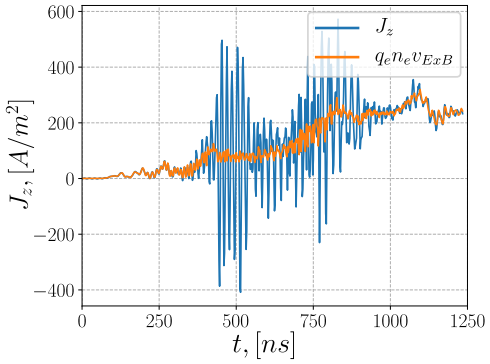

(a) Evolution of mean anomalous electron current density J_z and the current due to $\mathbf{E}_\theta \times \mathbf{B}$ drift.

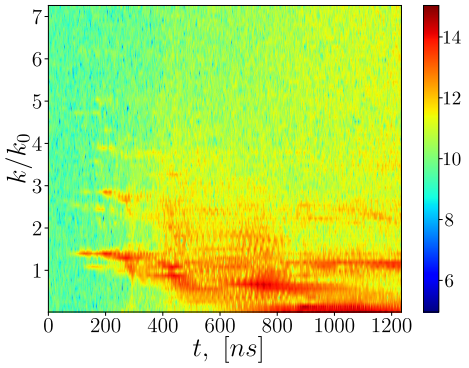

(b) Evolution of the azimuthal anomalous electron current k-spectra over time. The peaks in plot correspond to the $\omega - kv_0 = m\omega_c$ resonances.

Figure 4.5: Electron anomalous current; $L_\theta = 2$ cm, $L_r = 2$ cm, B $= 200$ G, E $= 200$ V/cm.

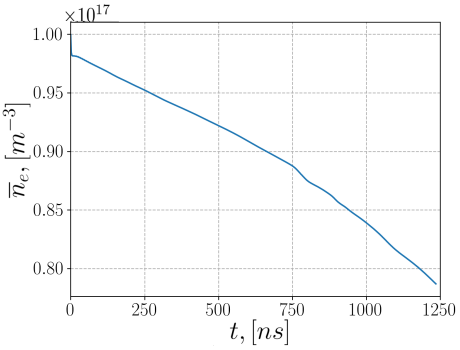

(a) Evolution of the averaged (in space) electron density $\overline{n}_e$.

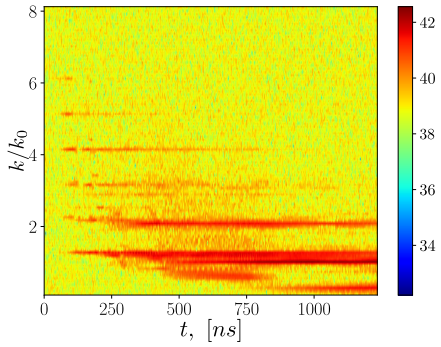

(b) Evolution of the azimuthal electron density k-spectra.

Figure 4.6: Evolution of the averaged electron density and its power spectrum.

In this Chapter, the plasma density decreases over time as there is no any particle source (e.g. due to ionization). For this case, 20% (at time $t = 1200$ ns) of the plasma density is lost through the radial metal walls (absorbing boundary). It is expected that a shorter radial length will lead to higher plasma losses due to the larger sheath area to the system area ratio. This effect is seen in the simulations of group A below. In Fig. 4.6b it is seen that the electron density cascades mostly to the first cyclotron mode, while in Fig. 4.7a, the ion density shows a more distributed energy between the first three ECDI modes. A different picture for the azimuthal electrostatic potential spectra is shown, Fig. 4.7b, it cascades to the lowest k-wavenumber during the MTSI mode saturation (at about $t = 500$ ns). Regarding the electron anomalous current an inverse cascade is observed as well, see Fig. 4.5b. The anomalous electron current evolves into the long-wavelength region (energy flow to long wavelengths).

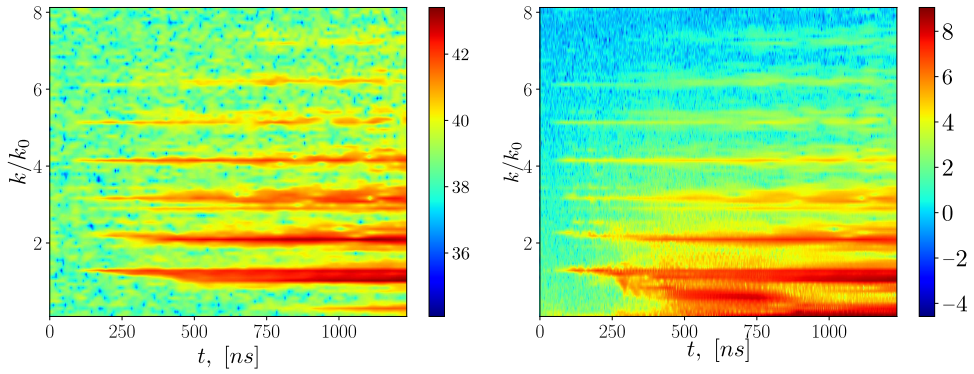

(a) Evolution of the azimuthal ion density k-spectra.

(b) Evolution of the azimuthal electrostatic potential k-spectra.

Figure 4.7: Evolution of azimuthal power spectrum.

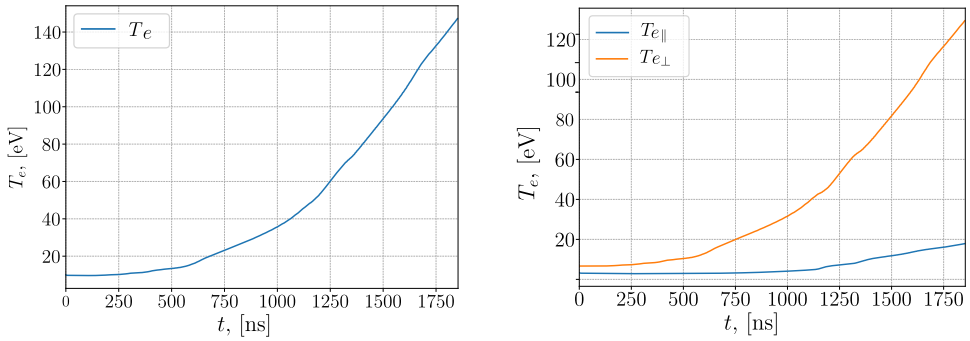

(a) Electron temperature.

(b) Electron temperature components.

Figure 4.8: Evolution of electron temperature.

Fig. 4.9a shows the evolution of the electron velocity distribution function (VDF) in azimuthal direction; it seen that an electron heating starts after the linear instabilities saturation and continues thereafter (see Fig. 4.8 for the temperature evolution). This continuous temperature growth is due to the absence of a heating saturation mechanism in the axial direction. In this setup an external field is applied in the axial direction which increases the axial energy of particles during the whole simulation. The increase of electron temperature is also seen in the electron azimuthal phase space, Fig. 4.11. In reality, the particles eventually will escape from the channel. One can employ a full 3D simulation (which is computationally expensive) or add a virtual axial coordinate (see Chapter 5). In the same time, the ion VDF suggests that there is no significant ion heating, Fig. 4.9b for the ion VDF evolution. However, one can see the ion trapping that develops later in the nonlinear regime, Fig. 4.10 show typical trapping-like patterns in the ion phase space. The electrostatic wave developed in the nonlinear regime has sufficient amplitude to trap some amount of ions, forming the ion structures similar to the electrostatic wavelength scale, Fig. 4.12b.

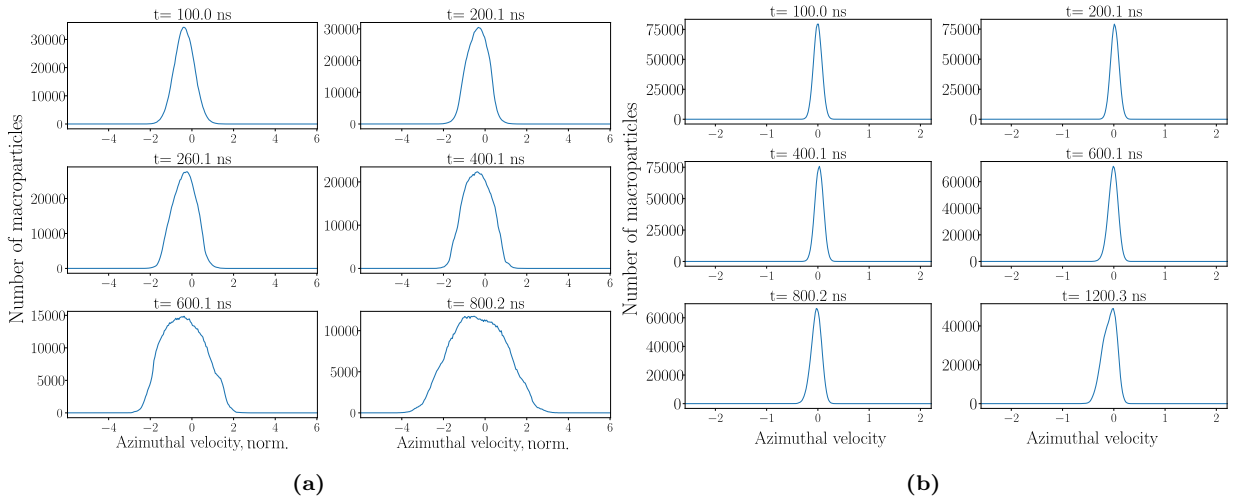

Figure 4.9: Evolution of the electron velocity distribution function in azimuthal direction, for $x, y =$ 1 cm, 1 cm (a), evolution of the ion velocity distribution (b).

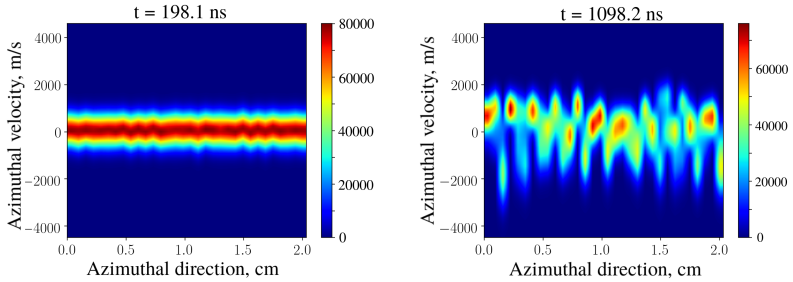

Figure 4.10: Ion phase space (azimuthal coordinate and velocity for a fixed radial position 1 cm), during the linear instability saturation, 198 ns (left), and the nonlinear stage, at 1098 ns (right), that shows trapping-like structures in an electrostatic wave.

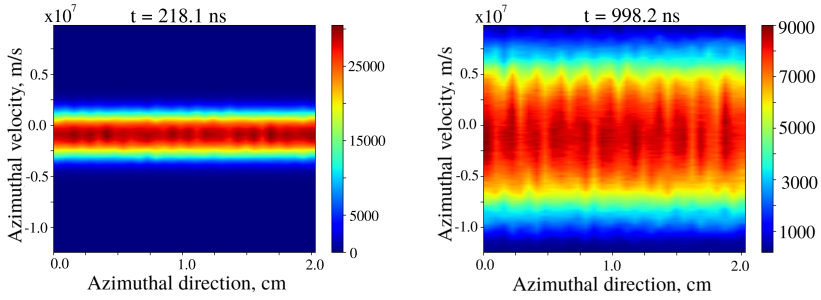

Figure 4.11: Electron phase space (azimuthal coordinate and velocity for a fixed radial position 1 cm)

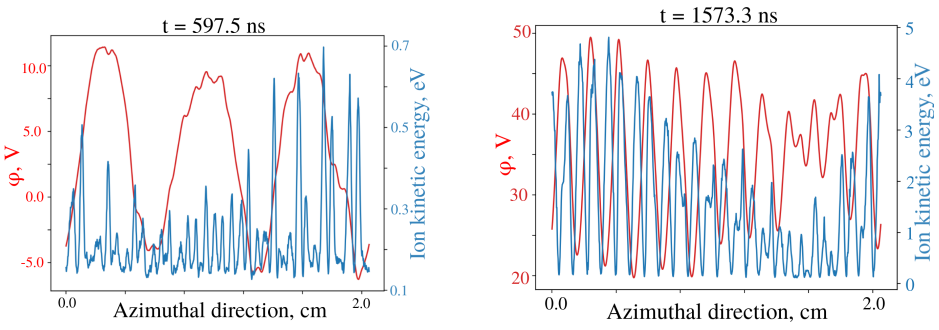

(a) **(b)**

Figure 4.12: Ion azimuthal energy (blue line) and azimuthal electrostatic potential (red line) for different time simulation.

4.1.2 MRUN-A2, azimuthal length, $L_\theta = 2$ cm, radial length, $L_r = 2$ $L_{r1} = 4$ cm.

The spectral density $|\phi_k|^2$ is plotted in Fig. 4.13a as a function of time. The growth rates for the first four cyclotron modes are $\gamma_1 = 1.383$, $\gamma_2 = 1.445$, $\gamma_3 = 1.625$, $\gamma_4 = 1.398$, respectively. Also, we note the growth of the small wavenumber $k = 0.179k_0$ that starts after the cyclotron modes saturation, with the growth rate $\gamma_0 = 0.257$; it is consistent with the solution of full dispersion equation. In the linear stage we did not observe any structural formations in the radial direction, so we can assume that the wavenumber k_z had it lowest possible value, $k_z = \pi/L_r$. For our system it is $k_z\lambda_{De} = 0.00584$, Fig. 4.13b shows the solution of the dispersion equation (2.48) in this case, with the growth rates obtained from the simulation. It can be seen that the most unstable wavenumbers appears in the simulation, in a full agreement with the dispersion equation.

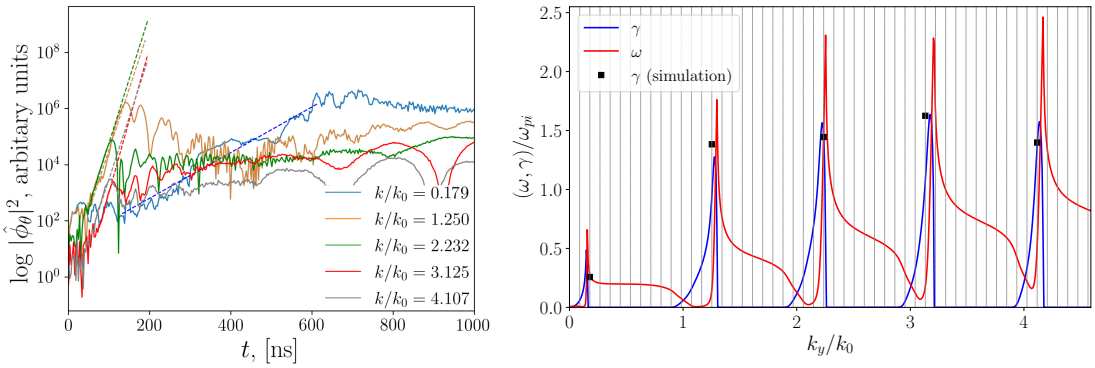

(a) Logarithmic amplitude of the azimuthal electric potential energy $|\phi_\theta|^2$.

(b) Growth rate and frequencies for $k_z\lambda_{De} = 0.00584$.

Figure 4.13: Linear growth and nonlinear saturation of the cyclotron and the MTSI modes. The different dashed lines represent the respective functions $y = 2\gamma t + c$ (found by linear regression) for the first cyclotron modes; as well as for the low-k MTSI mode.

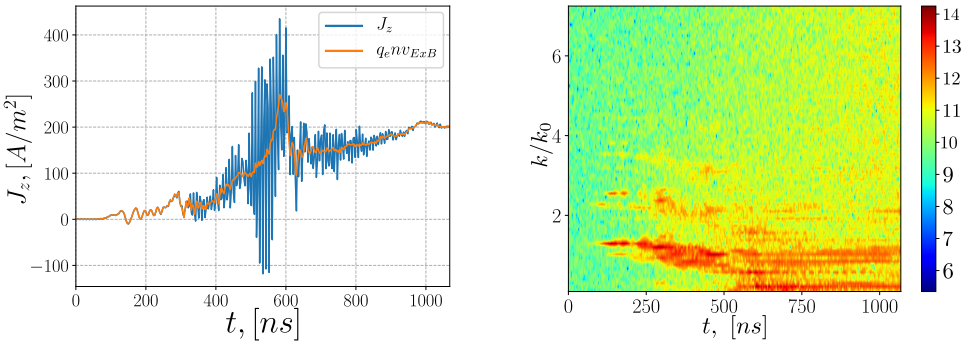

(a) Evolution of current J_z and due to $\mathbf{E} \times \mathbf{B}$ drift.

(b) Anomalous current k-spectra over time.

Figure 4.14: Electron anomalous current,; $L_\theta = 2$ cm, $L_r = 4$ cm.

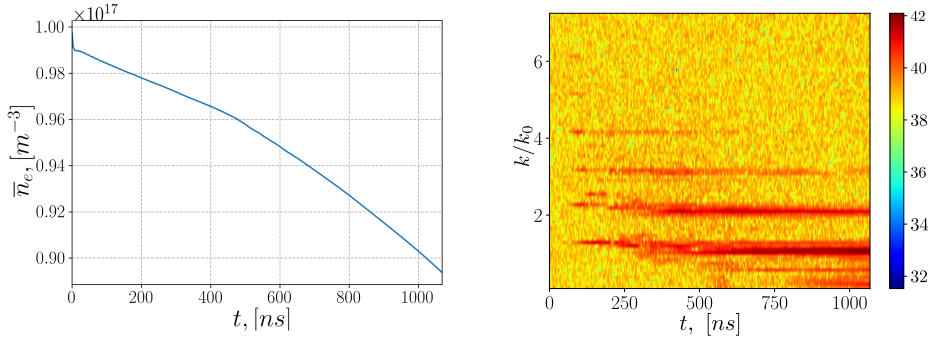

(a) Evolution of averaged (in space) electron density $\overline{n}_e$.

(b) Evolution of the azimuthal electron density k-spectra.

Figure 4.15: Electron density;, $L_r = 4$ cm.

Fig. 4.14 shows the comparison of the electron axial current and the current due to the nonlinear evolution of the ECDI. Fig. 4.15a describes the evolution of the electron density over time.

4.1.3 MRUN-A3, azimuthal length, $L_\theta = 2$ cm, radial length, $L_r = 0.5$ $L_{r1} = 1$ cm.

The growth rates for the first four cyclotron modes are $\gamma_1 = 1.482$, $\gamma_2 = 1.443$, $\gamma_3 = 1.362$, $\gamma_4 = 1.169$ respectively. Also, we note the growth of the small wavenumber $k = 0.357 k_0$, that starts after cyclotron modes saturation, with the growth rate $\gamma_0 = 0.293$; it is consistent with the solution of full dispersion equation, as shown in Fig. 4.16. However, the growth rates values for the ECDI modes obtained from simulation do not agree very well with the theoretical values. One can find the same discrepancy for the simulations using the dielectric walls as a boundary condition and the same radial system length $L_r = 1$ cm. In the linear stage we did not observe any structural formations in the radial direction, hence the ECDI modes may be developing as if in the one-dimensional case, with the growth rates that correspond to the $k_z \to 0$ solutions which was noted also in Ref. [12]. This all suggests that one can use the theoretical values for growth rates for the cyclotron modes from the one-dimensional dispersion relation (2.52) where $k_z \to 0$, while for the MTSI growth rates two-dimensional dispersion relation with the corresponding k_z value. As it is expected plasma

losses at time $t = 1000$ ns are higher for smaller radial length, about 30% of electrons lost on radial walls, while for the case of $L_r = 4$ cm just 10% of the electrons are absorbed. In fact, by the end of the simulation 80% of plasma were lost (by $t = 2000$ ns), suggesting that only early nonlinear development can be taken into account using data from this case.

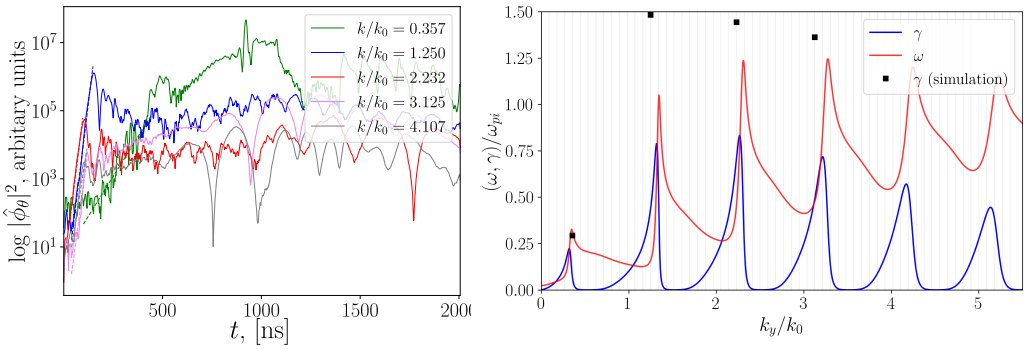

(a) Logarithmic amplitude of the azimuthal electric potential energy $|\phi_\theta|^2$.

(b) Growth rate and frequencies for $k_z\lambda_{De} = 0.0233$

Figure 4.16: Linear growth and nonlinear saturation of the cyclotron and the MTSI modes.

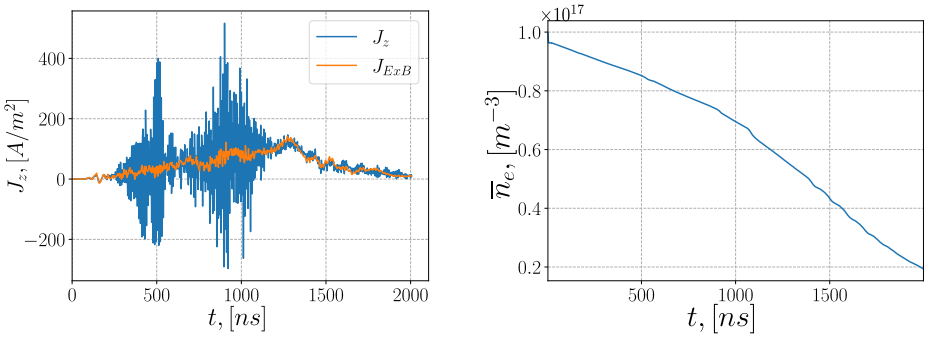

(a) Evolution of the anomalous current J_z.

(b) Evolution of averaged electron density $\overline{n}_e$.

Figure 4.17: Electron anomalous current; $L_r = 1$ cm.

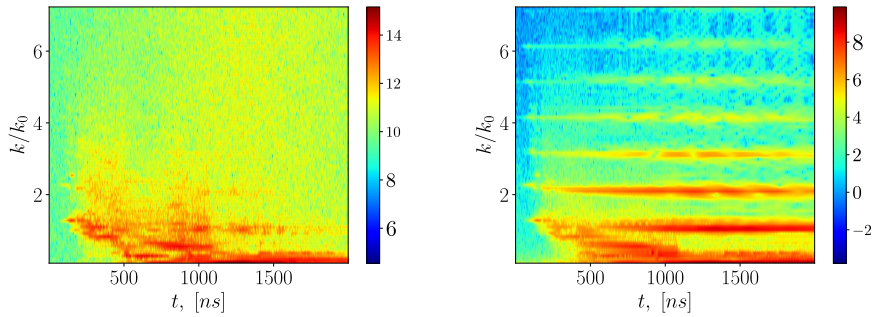

Figure 4.18: Evolution of the azimuthal electron current k-spectra (left), electrostatic potential k-spectra (right).

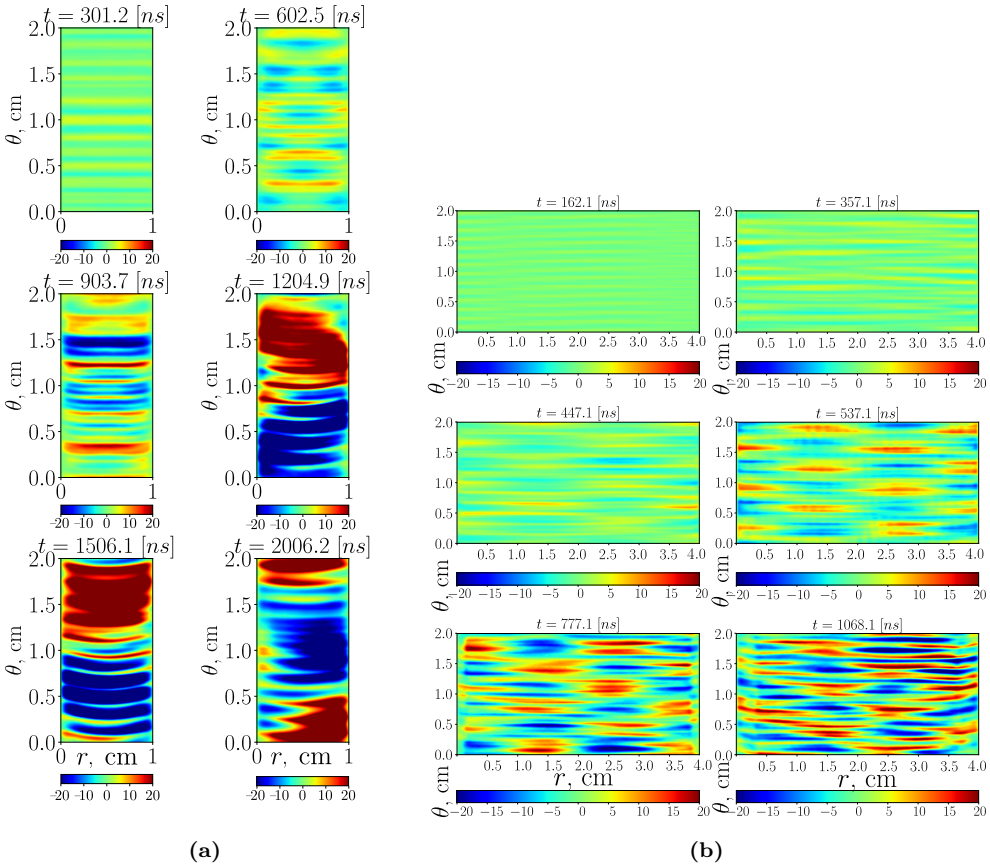

Figure 4.19: Nonlinear evolution of electrostatic potential fluctuations $\widetilde{\phi}$ for $L_r = 1$ cm (a) and $L_r = 4$ cm (b) in time.

Fig. 4.17 shows the comparison of the electron axial current and the current due to the nonlinear evolution of the ECDI. Fig. 4.18 describes the inverse cascade to low -k modes in both, the azimuthal electron current and the electrostatic potential. Overall, it is shown higher plasma losses when the radial length $L_r = 1\,\text{cm}$. In Fig 4.19a no radial structures are observe in the nonlinear evolution of electrostatic potential. For the case $L_r = 4\,\text{cm}$ radial structures appear even during the linear regime Fig 4.19b. For the formed azimuthal structures, the dominant mode drops to the lowest available wavenumber (cascades to the lowest) for $L_r = 1\,\text{cm}$, while for $L_r = 4\,\text{cm}$ it does not drop to the lowest wavenumber, but consistent to the MTSI mode.

4.1.4 MRUN-A4, azimuthal length $\mathrm{L}_\theta = 2$ $L_{\theta 1} = 4$ cm, radial length $\mathrm{L}_{r1} = 2$ cm

The growth rates for the first four cyclotron modes are $\gamma_1 = 1.204$, $\gamma_2 = 1.117$, $\gamma_3 = 1.661$, $\gamma_4 = 1.659$, respectively. Also, we note the growth of the small wavenumber $k = 0.27k_0$, that starts after cyclotron modes saturation, with the growth rate $\gamma_0 = 0.447$; it is consistent with the solution of full dispersion equation, as shown in Fig. 4.20. In the linear stage we did not observe any structural formations in the radial direction,

so we can assume that the wavenumber k_z had it lowest possible value, $k_z = \pi/L_r$. For our system it is $k_z\lambda_{De} = 0.01167$. Electron losses on radial walls in this case are slightly higher (20%) than in the base case (16%) for $t = 1000$ ns. As for the anomalous current, its value reaching a larger number, about twice higher than in the base case (400 A/m^2 vs 200 A/m^2).

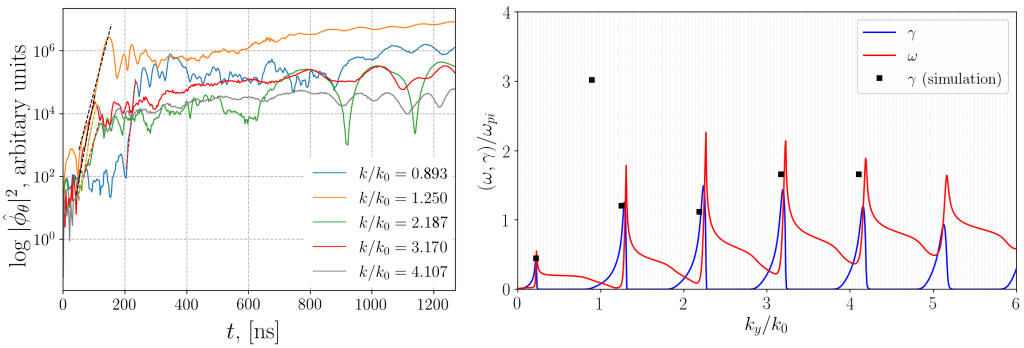

(a) Logarithmic amplitude of the azimuthal electric potential energy $|\phi_\theta|^2$.

(b) Growth rate and frequencies for $k_z\lambda_{De} = 0.011$.

Figure 4.20: Linear growth and nonlinear saturation of the cyclotron and the MTSI modes.

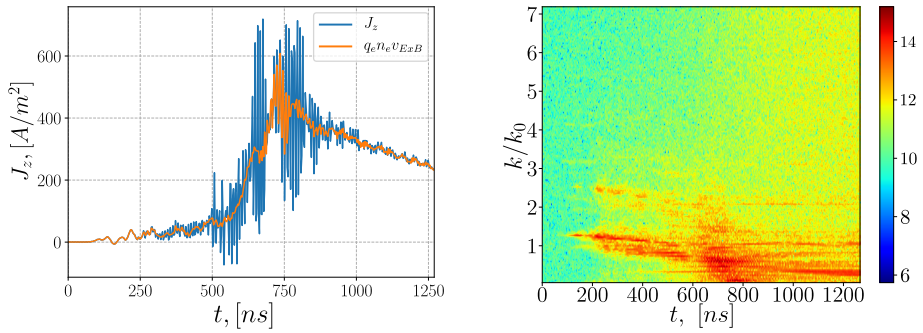

(a) Evolution of the anomalous current J_z .

(b) Anomalous current k-spectra.

Figure 4.21: Electron anomalous current; $L_\theta = 4$ cm.

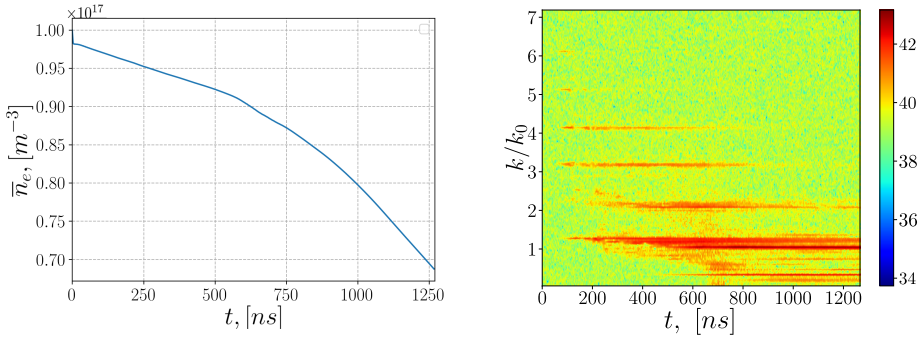

(a) Evolution of averaged electron density $\overline{n}_e$ over simulation time.

(b) Evolution of the azimuthal electron density k-spectra.

Figure 4.22: Electron density.

This result is expected for a larger azimuthal length, as the structures developed in this case are similar in physical dimensions, and the averaging over a higher total area leads to a higher value. Fig. 4.21 shows the comparison of the electron axial current and the current due to the nonlinear evolution of the ECDI.

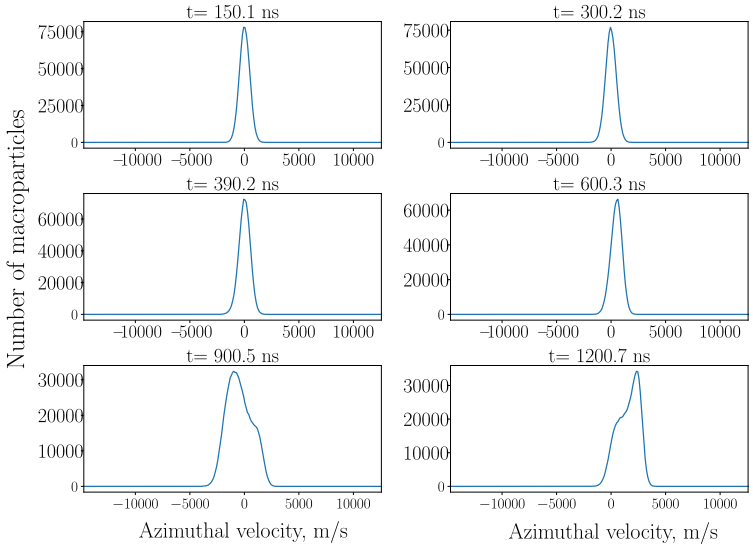

Figure 4.23: Evolution of the ion velocity distribution function in azimuthal direction, for $x, y = 2\,\text{cm}, 1\,\text{cm}$.

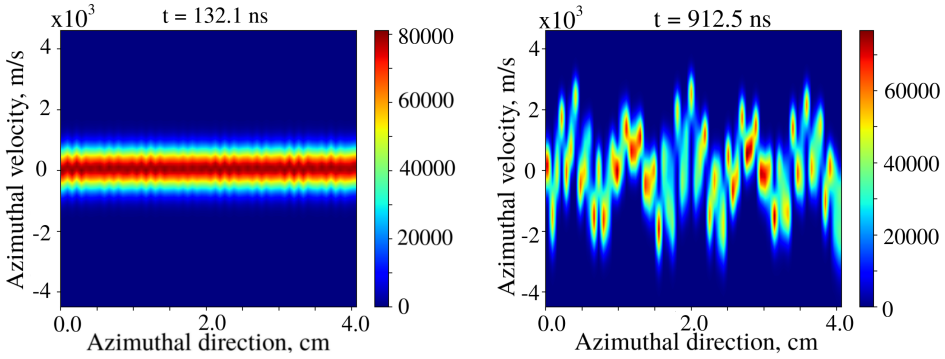

Figure 4.24: Ion phase space, trapping in an electrostatic wave, for 135 ns and 915 ns, respectively.

Fig. 4.23 illustrates the evolution of the ion distribution function for a fixed coordinate. Fig. 4.24 shows the ion trapping for two distinct simulation time.

4.1.5 MRUN-A5, azimuthal length, $\text{L}_\theta = 0.5$ $L_{\theta 1} = 1\,\text{cm}$, radial length, $\text{L}_{r1} = 2\,\text{cm}$

In this case with a shorter L_θ, the resolution in azimuthal k-space is poor compared with $L_\theta = (2, 4)$ cm, this is, some larger modes could be not captured. From Fig. 4.25a it is observed that the second cyclotron mode is dominant during the whole simulation. The anomalous current value for $L_\theta = 1\,\text{cm}$ is similar to the

general case with $L_\theta = 2$ cm. For the case of larger azimuthal length $L_\theta = 4$ cm a much higher anomalous current values are observed.

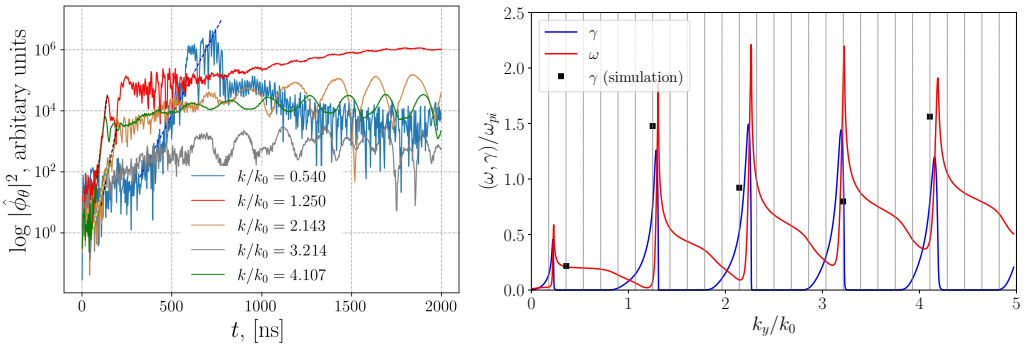

(a) Logarithmic amplitude of the azimuthal electric potential energy $|\phi_\theta|^2$.

(b) Growth rate and frequencies for $k_z\lambda_{De} = 0.01167$.

Figure 4.25: Linear growth and nonlinear saturation of the cyclotron and MTSI modes.

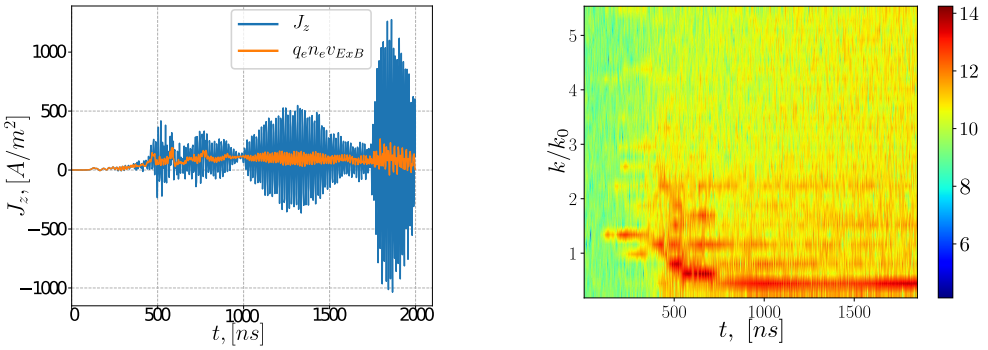

(a) Evolution of J_z and the current due to $\mathbf{E} \times \mathbf{B}$ drift.

(b) Anomalous current k-spectra over time.

Figure 4.26: Electron anomalous current; $L_\theta = 1$ cm.

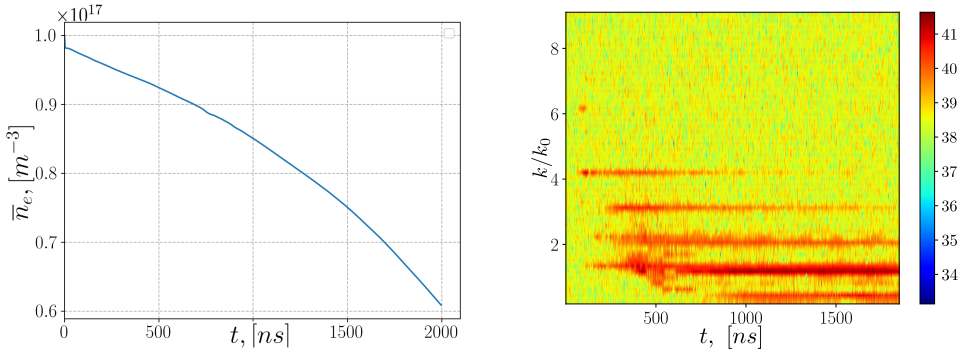

(a) Evolution of the averaged (in space) electron density $\overline{n}_e$.

(b) Electron density k-spectra over time.

Figure 4.27: Evolution of electron density.

This results is expected as the anomalous current is explained due to the perturbed azimuthal self-consistent electric field. Moreover, for a longer azimuthal extent, radial structures appear earlier that the case with smaller azimuthal extent.

Fig. 4.26 shows the comparison of the electron axial current and the current due to the nonlinear evolution of the ECDI. Fig. 4.27 illustrates the electron density evolution and how the first cyclotron mode dominates during the whole simulation.

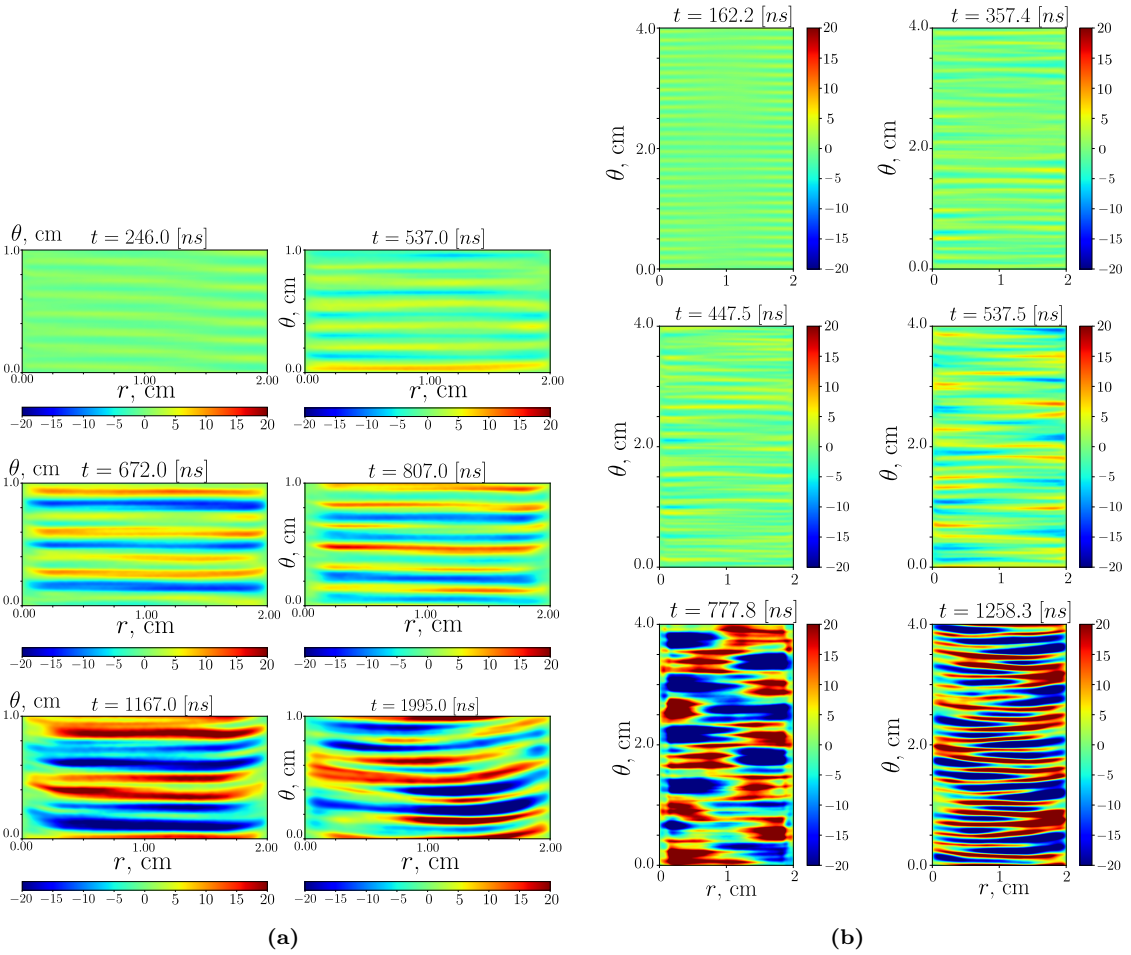

Figure 4.28: Nonlinear evolution of electrostatic potential fluctuations $\widetilde{\phi}$ for $L_\theta = 1$ cm (a) and $L_\theta = 4$ cm (b) in time.

4.1.6 MRUN-B6, plasma density: N = 0.5 $N_0 = 0.5 \times 10^{17}\,\mathrm{m}^{-3}$

Decreasing the plasma density for both cases, using metal or dielectric walls, results in a very similar behavior and a small value for the observed anomalous current. The magnitude of the anomalous current when decreasing the plasma density correspond to the smallest values (40 A/m^2), as is demonstrated in Fig. 4.29. between all the cases performed for the scaling study. Thus, as it will be shown below when increasing the plasma density it leads to the highest anomalous current value, which is expected as $J_z \sim N$.

For both cases (metal and dielectric walls) the perturbed electron density k-spectra evolves to a low-k wavenumber (inverse cascade) that corresponds to the first cyclotron mode. Plasma losses are the same compared with the base case, 15% at simulation time $t = 1000$ ns, with the initial sheath loss values of 3%, as shown in Fig. 4.30.

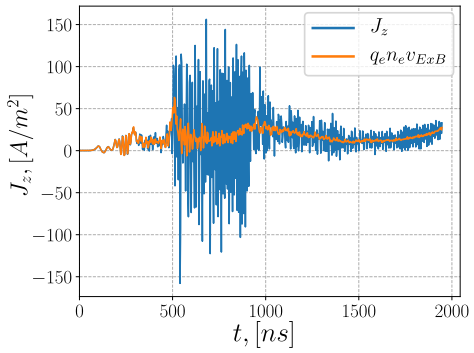

(a) Evolution of J_z and the current due to $\mathbf{E} \times \mathbf{B}$ drift.

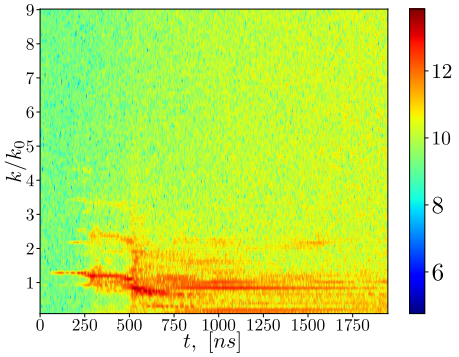

(b) Anomalous current k-spectra over time.

Figure 4.29: Electron anomalous current; $\mathrm{N} = 0.5 \times 10^{17}\,\mathrm{m}^{-3}$.

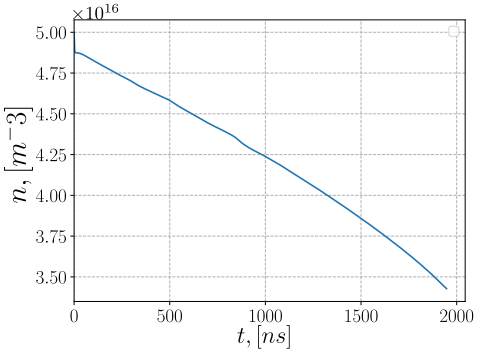

(a) Evolution of averaged electron density $\overline{n}_e$ over simulation time.

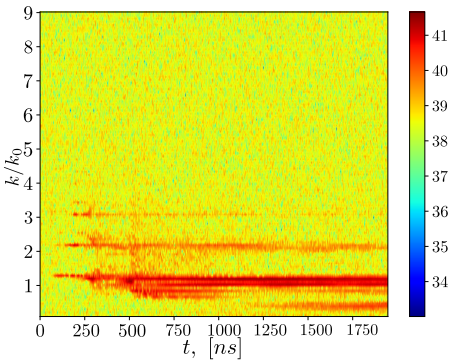

(b) Evolution of the azimuthal electron density k-spectra.

Figure 4.30: Evolution of electron density.

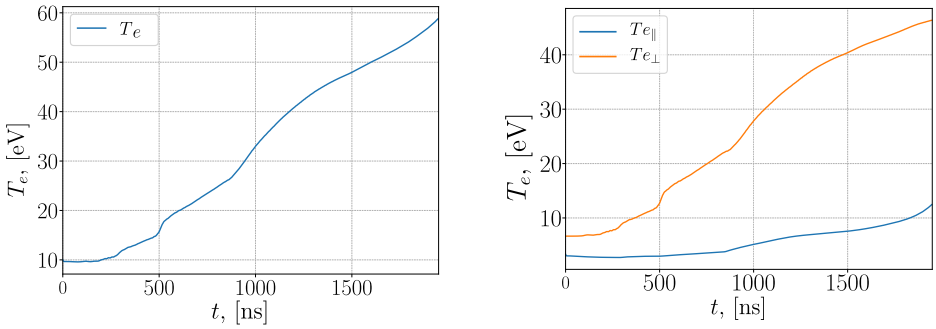

Figure 4.31: Electron temperature, $\mathrm{N} = 0.5 \times 10^{17}\,\mathrm{m}^{-3}$.

In Fig. 4.31 is plotted the electron temperature evolution, one can see that the perpendicular velocity is higher due to the absence of a heating saturation mechanism.

4.1.7 MRUN-B7, plasma density: N = 2 $N_0 = 2 \times 10^{17}\,\mathrm{m}^{-3}$

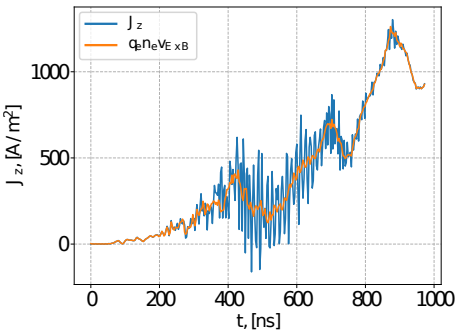

(a) Evolution of J_z and the current due to $\mathbf{E} \times \mathbf{B}$ drift.

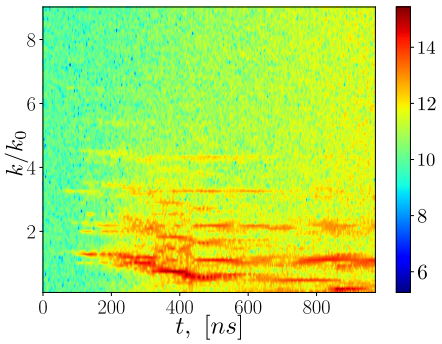

(b) Anomalous current k-spectra over tme.

Figure 4.32: Evolution of anomalous current.

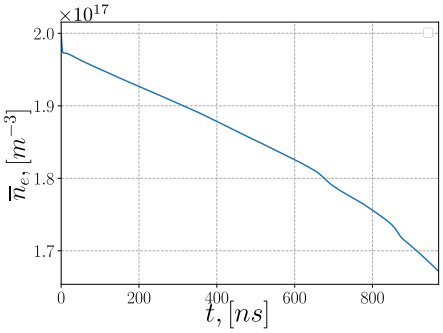

(a) Evolution of averaged electron density $\overline{n}_e$ over simulation time.

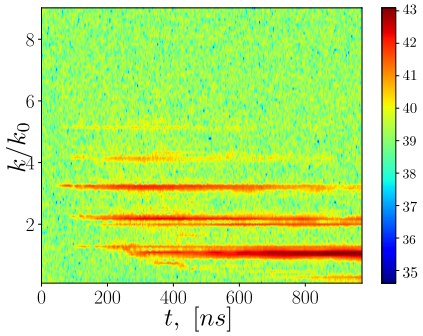

(b) Evolution of the azimuthal electron density k-spectra.

Figure 4.33: Evolution of electron density.

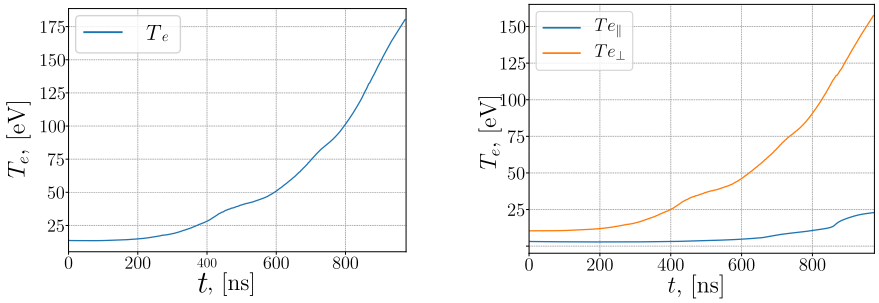

(a) **(b)**

Figure 4.34: Electron temperature; N = $2 \times 10^{17}\,\mathrm{m}^{-3}$.

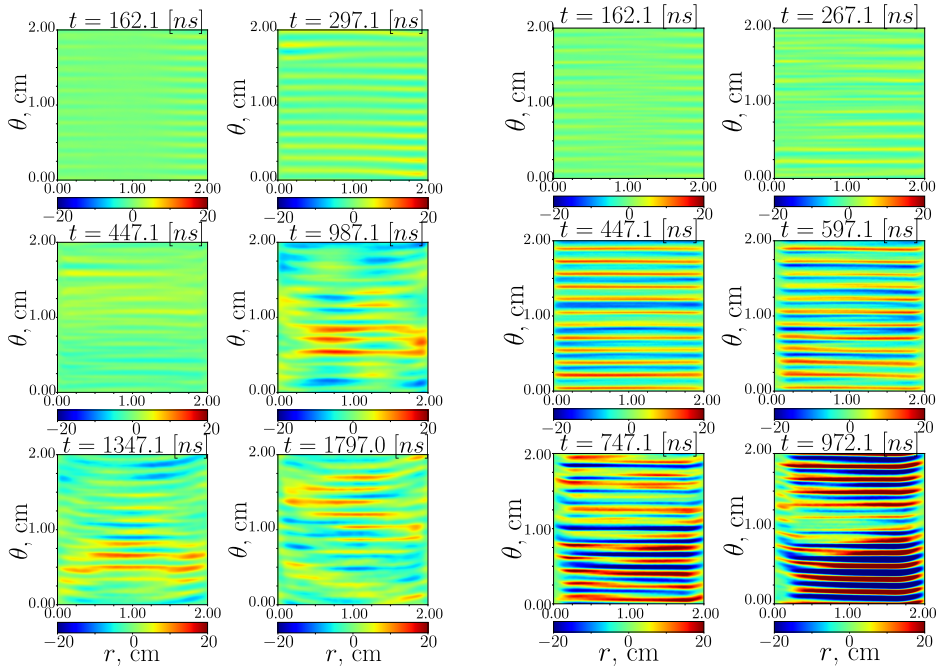

(a) **(b)**

Figure 4.35: Nonlinear evolution of electrostatic potential $\widetilde{\phi}$ in time for $\mathrm{N} = 0.5 \times 10^{17}\,\mathrm{m}^{-3}$ (a), $\mathrm{N} = 2 \times 10^{17}\,\mathrm{m}^{-3}$ (b).

Increasing the plasma density for both cases, using metal or dielectric walls, leads to a very similar behavior and to high values for the anomalous current, as shown in Fig. 4.32. The evolution of electron density shows that first cyclotron mode is dominant for the azimuthal electron density (see Fig4.33b). The electron temperature component parallel to the magnetic field (radial direction) and the electron temperature component perpendicular to the magnetic field (azimuthal and axial direction) are shown in Fig. 4.34. The nonlinear evolution of electrostatic in Fig. 4.35 shows that for the case of higher plasma density the clear dominate mode is the MTSI mode, while for the case of lower plasma density, the first cyclotron mode dominates (ECDI mode).

4.1.8 MRUN-C8, scaling electric field $\mathrm{E} = 0.5$ $E_0 = 100\,\mathrm{V/cm}$

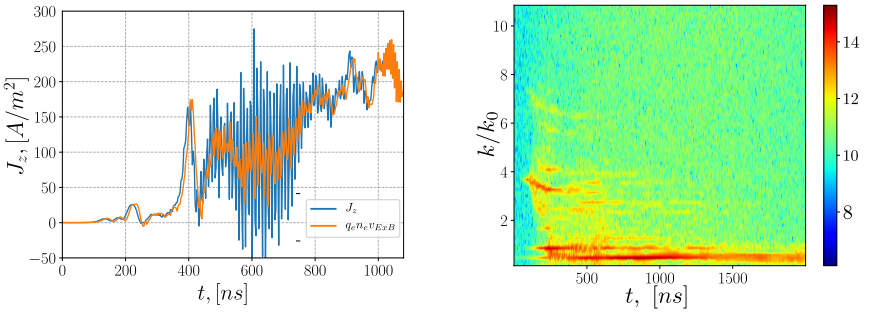

(a) Evolution of electron current J_z.

(b) Anomalous current k-spectra.

Figure 4.36: Evolution of anomalous current; $\mathrm{E} = 100\,\mathrm{V/cm}$.

Decreasing the electric field for both cases, using metal or dielectric walls leads to a very similar results. The anomalous current values are shown in Fig. 4.36. It is found that the first cyclotron mode is dominant for the azimuthal electron density (see Fig. 4.37b). The electron temperature values are lower than those for the general case ($\mathbf{E} = 200\,\mathrm{V/cm}$).

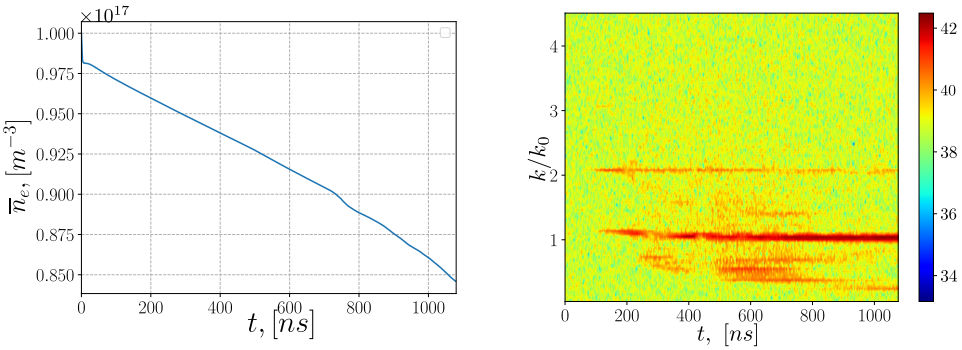

(a) **(b)**

Figure 4.37: Evolution of electron density.

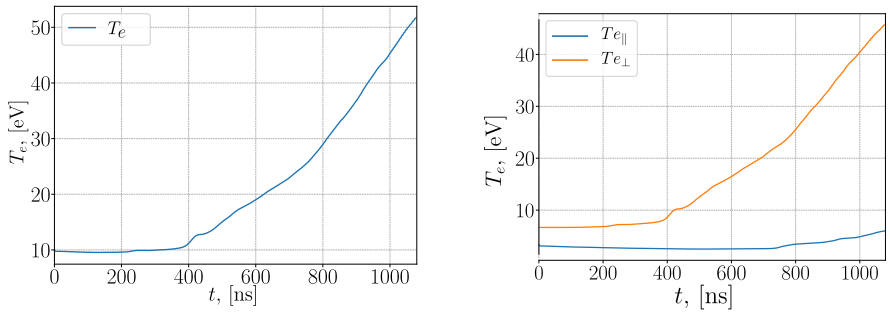

(a) **(b)**

Figure 4.38: Electron temperature; $\mathrm{E} = 100\,\mathrm{V/cm}$.

4.1.9 MRUN-C9, scaling electric field $\mathrm{E} = 2\ E_0 = 400\,\mathrm{V/cm}$

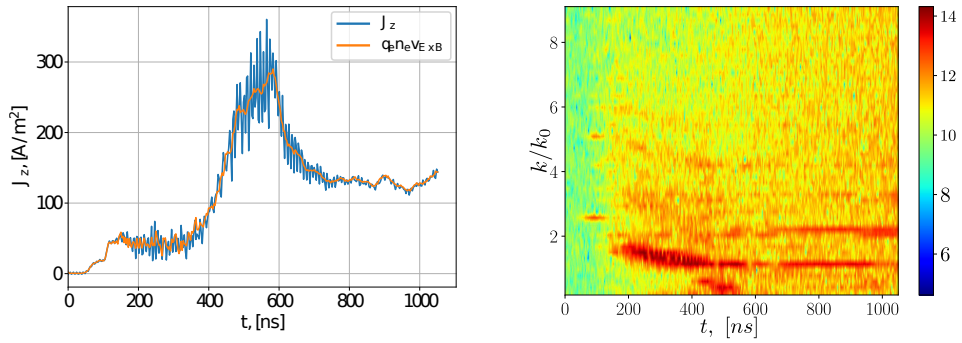

(a) Evolution of J_z and the current due to $\mathbf{E} \times \mathbf{B}$ drift.

(b) Anomalous current k-spectra over time.

Figure 4.39: Evolution of anomalous current; $\mathrm{E} = 400\,\mathrm{V/cm}$.

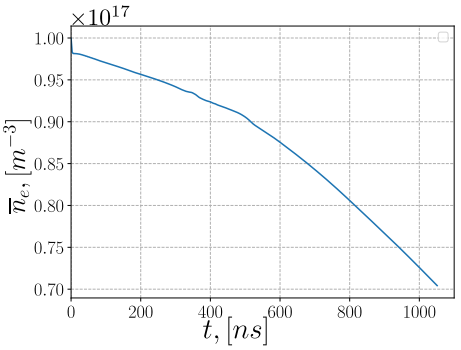

(a) Evolution of the averaged (in space) electron density $\overline{n}_e$.

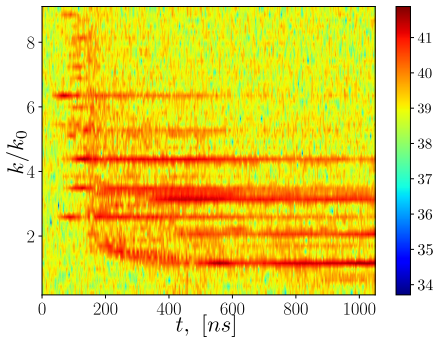

(b) Evolution of azimuthal electron density k-spectra.

Figure 4.40: Evolution of electron density; E = 400 V/cm.

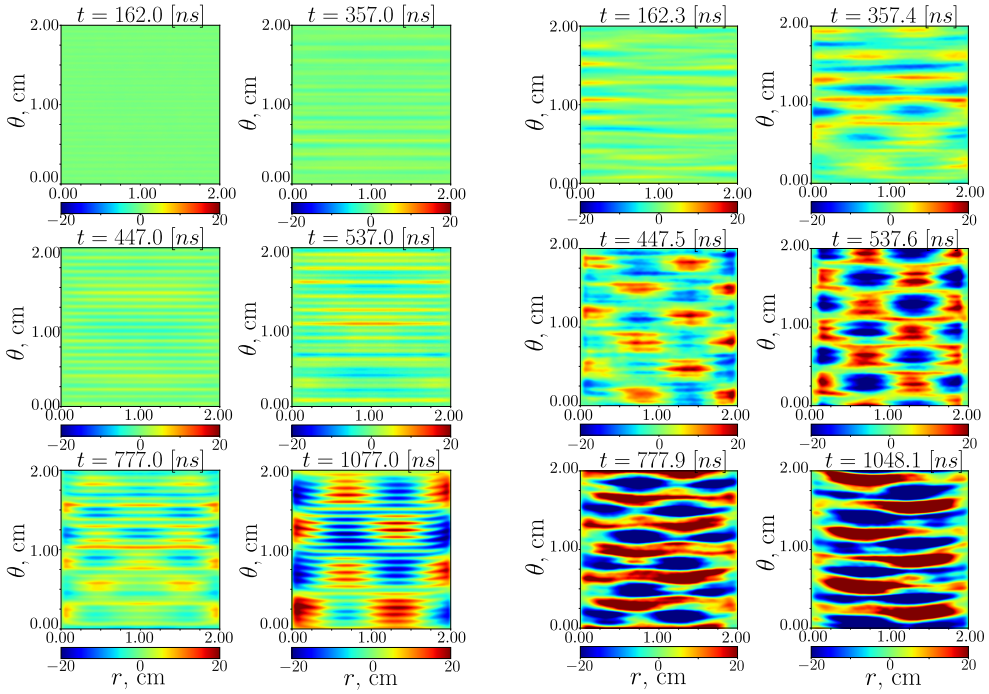

(a) **(b)**

Figure 4.41: Nonlinear evolution of electrostatic potential $\widetilde{\phi}$, E = 100 V/cm (a), E = 400 V/cm (b).

The anomalous current values remains similar to the case previous case (see Fig. 4.39). Fig. 4.41, shows the evolution of the internal electric field, for cases with lower and higher applied electric fields. As a consequence of different drift velocity, the cyclotron wavenumbers in the case of higher electric field are lower, i.e. wavelengths are larger, as can be seen during the linear regime. Also, the radial patterns for the case of higher electric field appear earlier in the simulation than for the case of smaller electric field. These cases are also different in the number of various cyclotron modes that develops during the simulation, for the case E = 100 V/cm only first two cyclotron modes develops, Fig. 4.37b, and for the case E = 400 V/cm up to

~ 8 modes are visible, Fig. 4.40b. Below, in the Section 5.4 the comparison of dispersion equation solutions is given for the cases with changing electric field.

4.1.10 MRUN-D10, scaling magnetic field B $= 0.5$ $B_0 = 100$ G

Next Figs 4.42-4.44, illustrate the anomalous current evolution; the electron density evolution, and the electron temperature components, respectively.

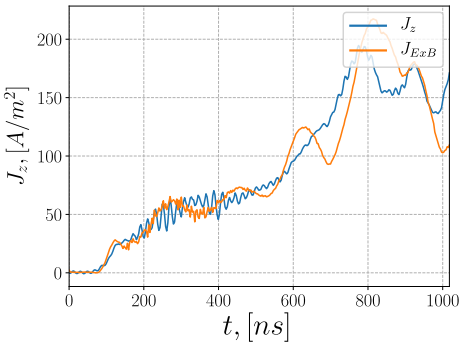

(a) Evolution of J_z and the current due to $\mathbf{E} \times \mathbf{B}$ drift.

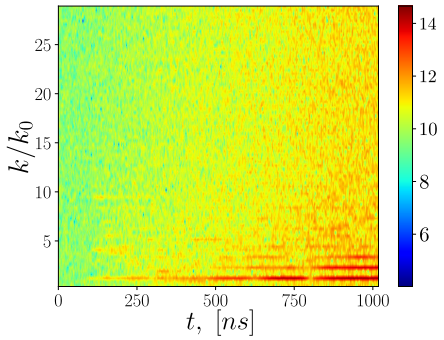

(b) Anomalous current k-spectra over time.

Figure 4.42: Electron anomalous current; $B_0 = 100$ G.

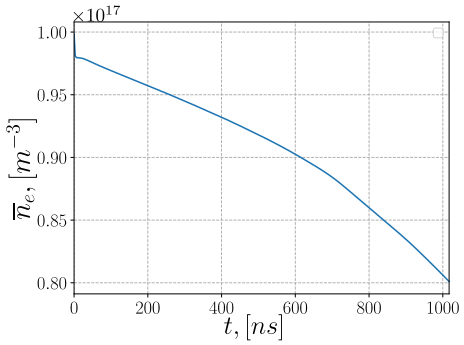

(a) Evolution of the averaged (in space) electron density $\overline{n}_e$.

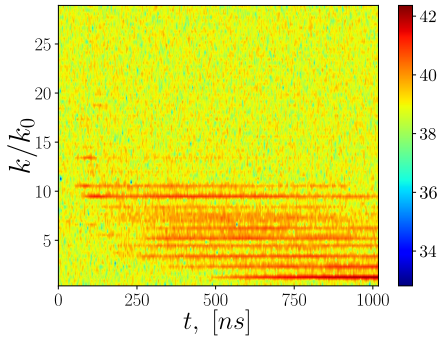

(b) Evolution of azimuthal electron density k-spectra.

Figure 4.43: Electron density.

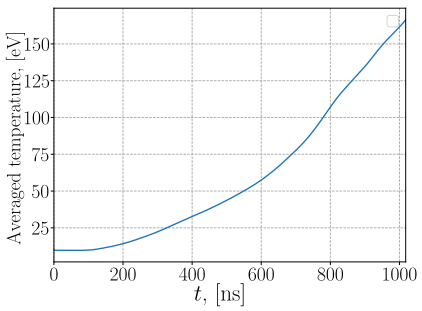

(a)

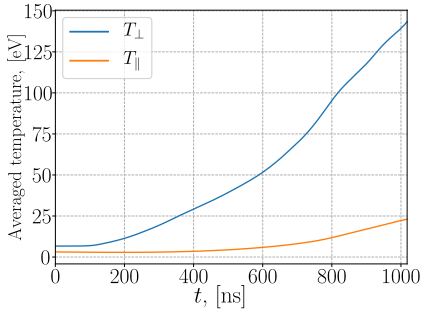

(b)

Figure 4.44: Electron temperature.

4.1.11 MRUN-D11, scaling magnetic field B = 2 B_0 = 400 G

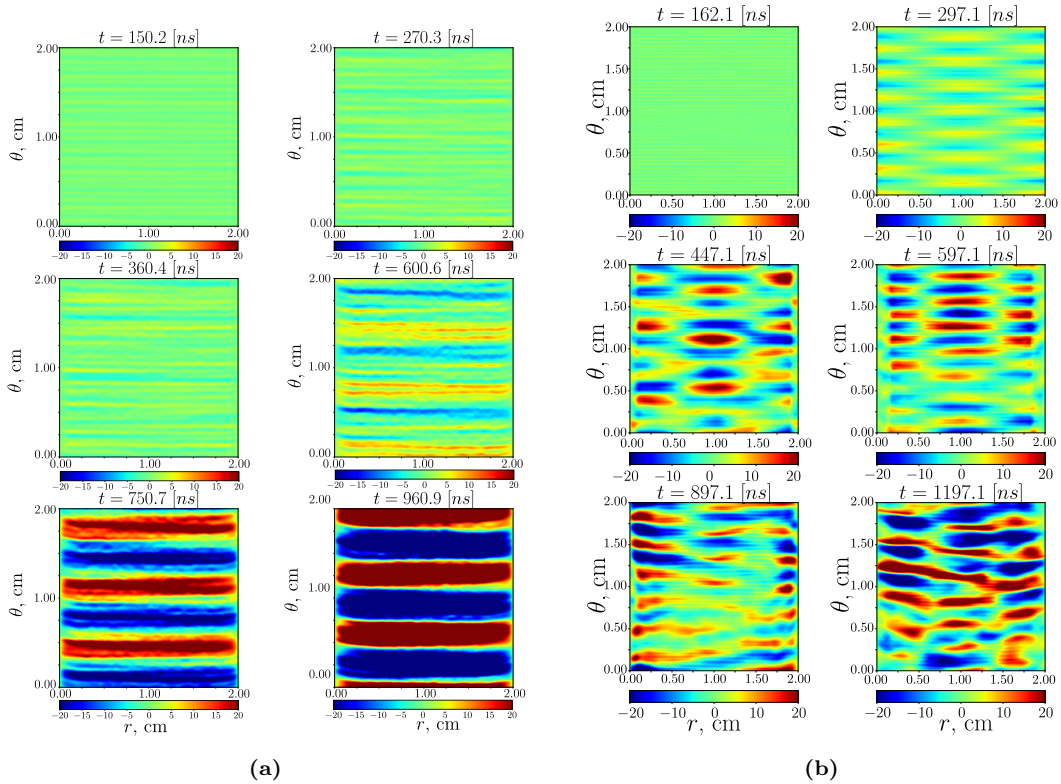

(a) **(b)**

Figure 4.45: Nonlinear evolution of electrostatic potential fluctuations $\widetilde{\phi}$ in time for B = 100 G (a) B = 400 G (b).

It is seen in Fig. 4.45 for the case with higher magnetic field, that in early linear stages clear radial structures appear, while for the case of lower magnetic field no radial patterns are observed. The growth rate values for the dispersion relations show that the MTSI mode is stronger for B = 400 G. For the case of B = 100 G larger wavelengths develop in the nonlinear stage.

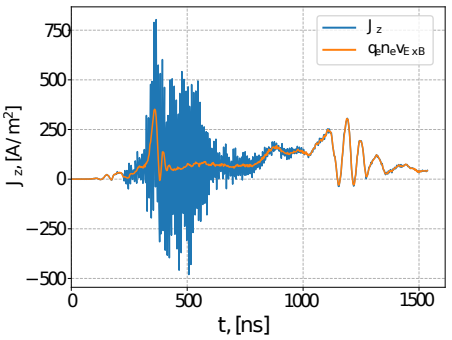

(a) Evolution of J_z and the current due to $\mathbf{E} \times \mathbf{B}$ drift.

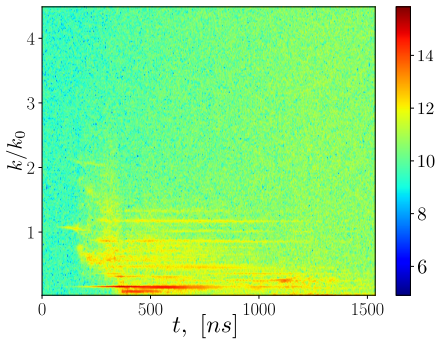

(b) Anomalous current k-spectra over time.

Figure 4.46: Electron anomalous current.

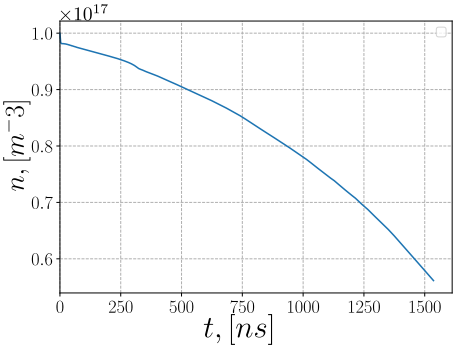

(a) Evolution of averaged electron density $\overline{n}_e$ over simulation time.

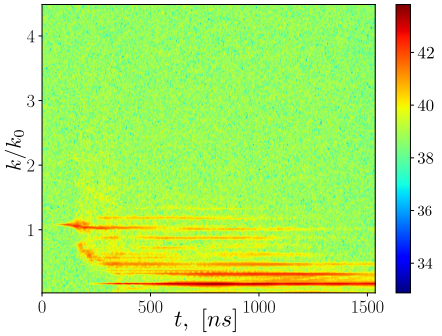

(b) Evolution of azimuthal electron density k-spectra.

Figure 4.47: Evolution of electron density.

The axial electron current value is similar to the general case value (see Fig. 4.46). Fig 4.47 shows that the plasma losses in the wall are similar to those for B = 400 G.

4.1.12 MRUN-E12, magnetic field, B = 0.5 B_0 = 100 G and electric field, E = 0.5 E_0 = 100 V/cm

In the previous cases, only one parameter was changed. Here we vary both E and B fields. The growth rates for the first four cyclotron modes are $\gamma_1 = 0.626$, $\gamma_2 = 0.890$, $\gamma_3 = 1.039$, $\gamma_4 = 0.338$,$\gamma_5 = 1.249$, respectively. Also, we note the growth of the small wavenumber $k = 0.357k_0$, that starts after cyclotron modes saturation, with the growth rate $\gamma_0 = 0.102$; For our system $k_z = \pi/L_r$. $k_z\lambda_{De} = 0.01167$. In Fig. 4.48a it is seen that the 3$^{\text{rd}}$ cyclotron mode dominates up to the end of the simulation. The comparison of the measured growth rates with the kinetic dispersion solution, Fig. 4.48b, reveals a good agreement for the MTSI mode, but discrepancies for ECDI modes are notably higher, up to about 60%. Interestingly, this simulation resulted in the highest value of electron anomalous current, 700 A/m^2, Fig. 4.50a.

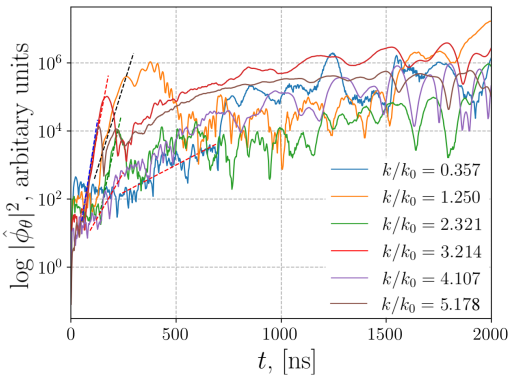

(a) Logarithmic amplitude of the azimuthal electric potential energy $|\phi_\theta|^2$.

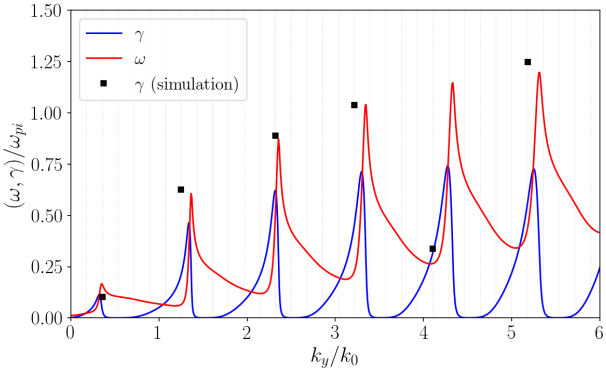

(b) Growth rate and frequencies for $k_z\lambda_{De} = 0.011$.

Figure 4.48: Linear growth and nonlinear saturation of the cyclotron and the MTSI modes.

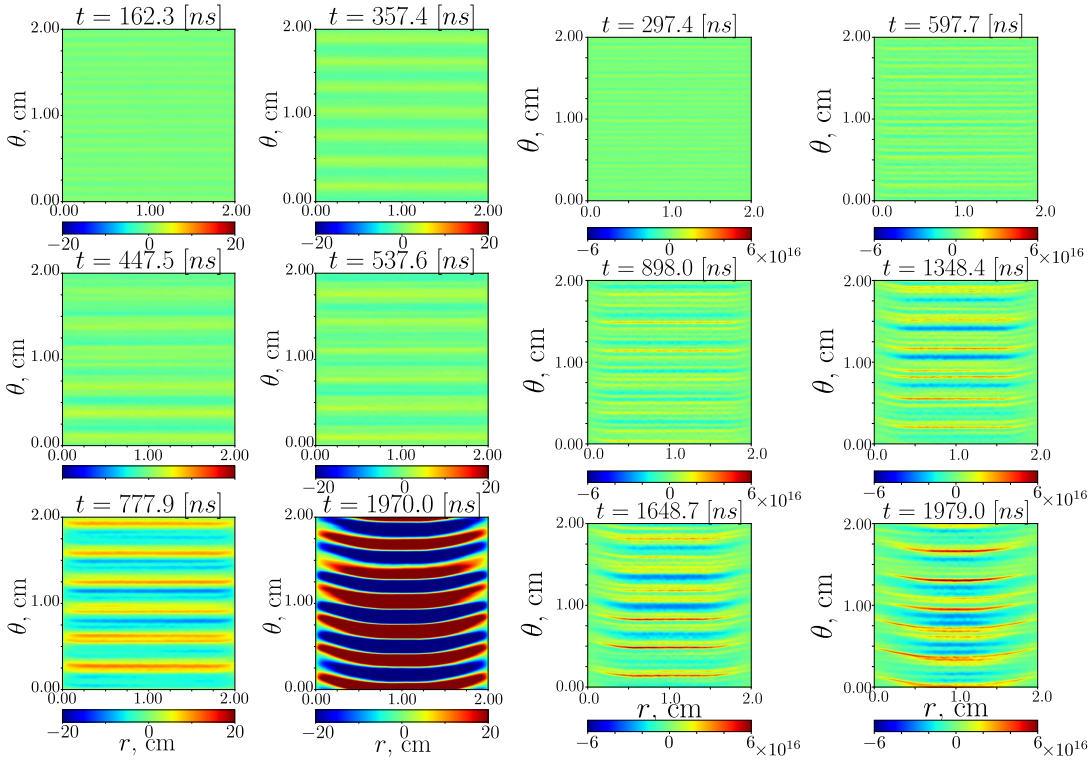

Figure 4.49: Nonlinear evolution of electrostatic potential fluctuations $\widetilde{\phi}$ in time (left) and ion density (right); B = 100 G, E = 100 V/cm.

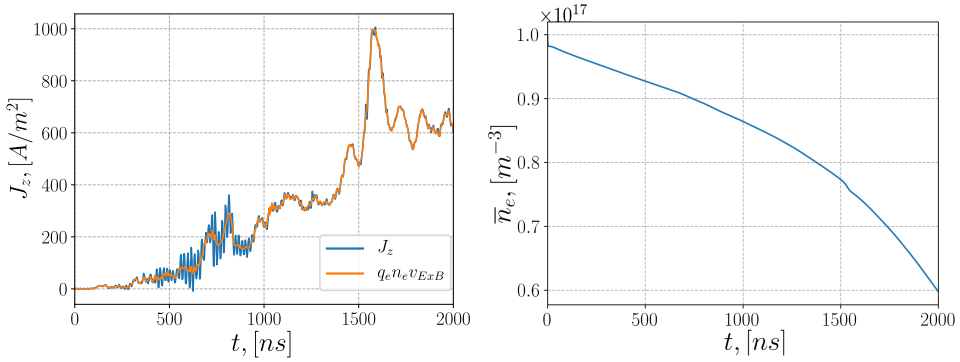

(a) Evolution of mean anomalous current density J_z.

(b) Evolution of the averaged (in space) electron density $\overline{n}_e$.

Figure 4.50: Electron anomalous current; L_θ = 2 cm, L_r = 2 cm, B = 100 G, E = 100 V/cm.

Fig. 4.50 illustrates that the anomalous current values are much higher than those for the general case.

4.1.13 MRUN-E13, magnetic field, B = 2 B_0 = 400 G and electric field, E = 2 E_0 = 400 V/cm

For this case increasing both, the electric and magnetic field the drift velocity remains as in the base case $V_D = 10^6$ m/s. The anomalous current value is similar to the general case (see Fig. 4.53). The

MTSI mode start growing in the same time as the ECDI modes, contrary to the base case where the MTSI start growing after cyclotron modes saturate, see Fig. 4.51a. The MTSI mode is the largest after the linear saturation, and then it mostly dominates in the nonlinear regime, along with the 3$^{\text{rd}}$ cyclotron mode. It can be seen that the growth rate of the MTSI is comparable with the growth rate of the cyclotron modes, Fig. 4.51b, which differs from the base case configuration where its growth rate value was few times smaller compared with the ECDI values.

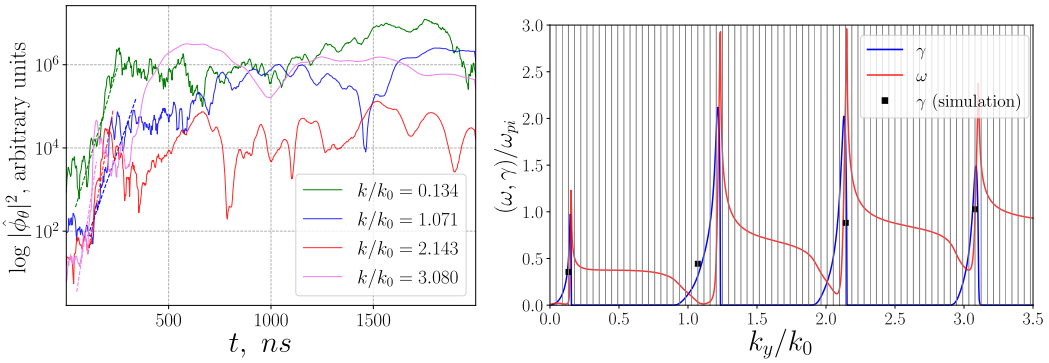

(a) Logarithmic amplitude of the azimuthal electric potential energy $|\phi_\theta|^2$

(b) Growth rate and frequencies for $k_z\lambda_{De} = 0.011$.

Figure 4.51: Linear growth and nonlinear saturation of the cyclotron and the MTSI modes.

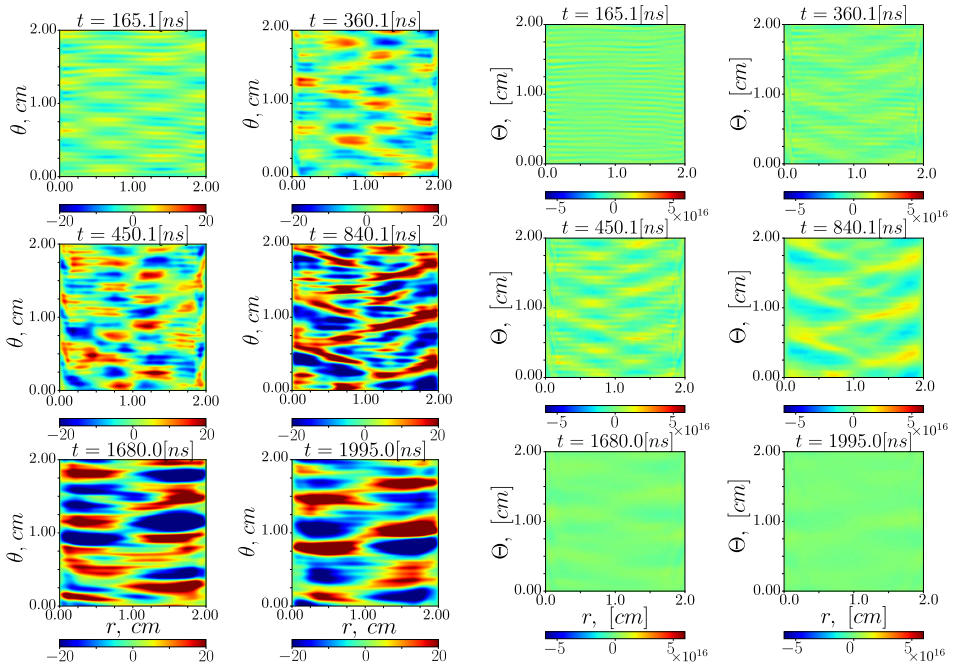

(a) **(b)**

Figure 4.52: Nonlinear evolution of electrostatic potential fluctuations $\widetilde{\phi}$ in time (a) and electron density (b); B = 400 G, E = 400V/cm.

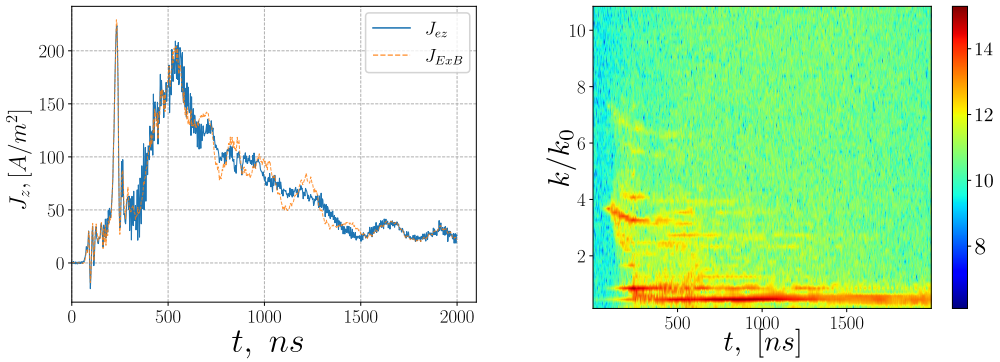

(a) Evolution of J_z and the current due to $\mathbf{E} \times \mathbf{B}$ drift.

(b) Anomalous current k-spectra over time.

Figure 4.53: Electron anomalous current.

The presence of the MTSI mode right from the start is also seen on two-dimensional images of potential, Fig. 4.52a, and the electron density, Fig. 4.52b.

4.2 Azimuthal-radial simulations with dielectric walls

In this section the results for various runs with radial direction bounded with two dielectric walls. On each side these boundaries are modeled as semi-infinite uniform isotropic dielectric, with relative dielectric permittivity ε [31]. The rest of the simulation results and descriptions can be found in the appendices section C. The reference (base) case for this section is the DRUN-14, which is similar to the base case MRUN-1 but differs in the radial boundary conditions. Same absorbing conditions for particles.

4.2.1 DRUN-14, azimuthal length, $L_\theta = 2$ cm, radial length, $L_r = 2$ cm, $\varepsilon = 2$

No significant difference was found in the result of this case in compare to the base case (MRUN-1).

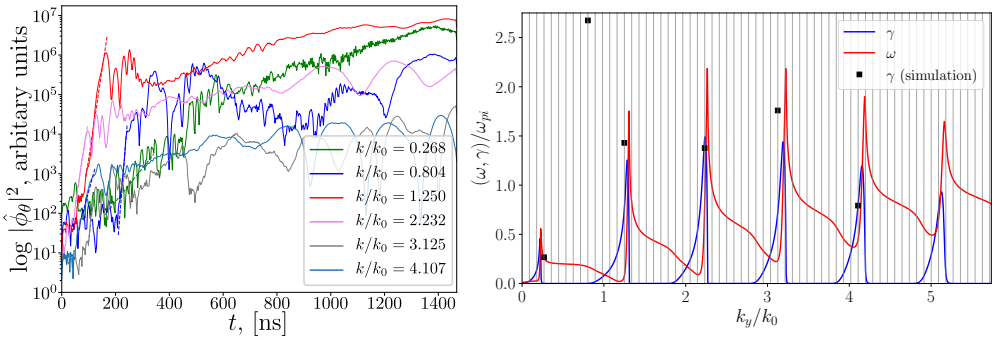

(a) Logarithmic amplitude of the azimuthal electrostatic potential energy $|\phi_\theta|^2$.

(b) Growth rate and frequencies for $k_z\lambda_{De} = 0.00585$.

Figure 4.54: Linear growth and nonlinear saturation of the cyclotron and the MTSI modes.

The observed plasma losses are the same, the values of anomalous current are similar, as shown in Fig. 4.55. The growth rates for the first four cyclotron modes are: $\gamma_1 = 1.430, \gamma_2 = 1.376, \gamma_3 = 1.759, \gamma_4 = 0.792$, and the MTSI mode with $\gamma_0 = 0.268$. These growth rates are also similar to the base case with metal walls (see Fig. 4.54). We also see that the first cyclotron mode dominates during the simulation period in both runs, and that the MTSI mode starts growing after the ECDI mode saturation.

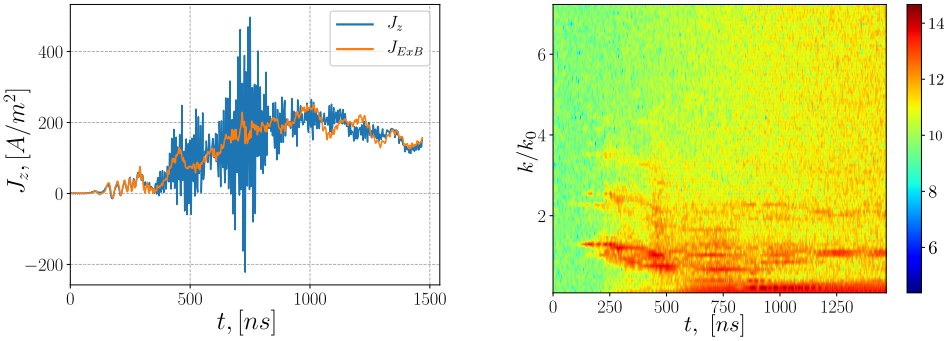

(a) Evolution of J_z and the current due to $\mathbf{E} \times \mathbf{B}$ drift.

(b) Anomalous current k-spectra over time.

Figure 4.55: Evolution of the axial electron current J_z, $\varepsilon = 2$.

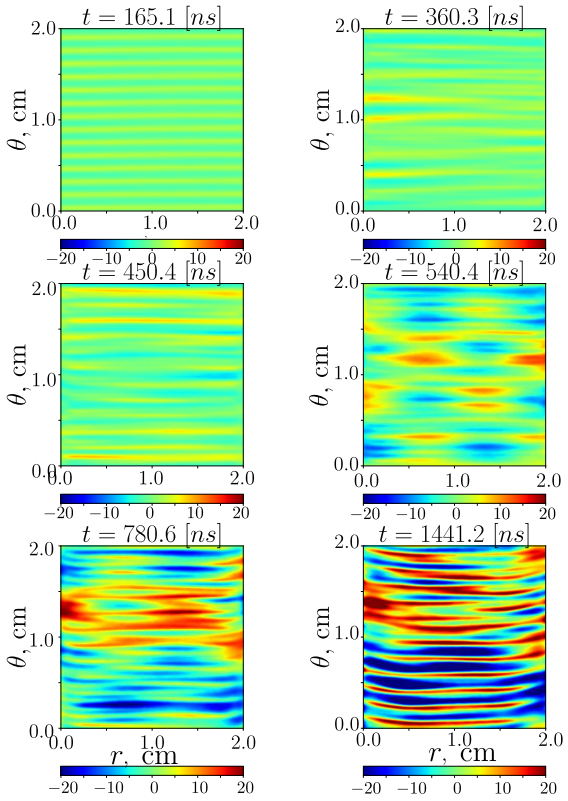

Figure 4.56: Nonlinear evolution of electrostatic potential fluctuations $\widetilde{\phi}$ in time; $\varepsilon = 2$.

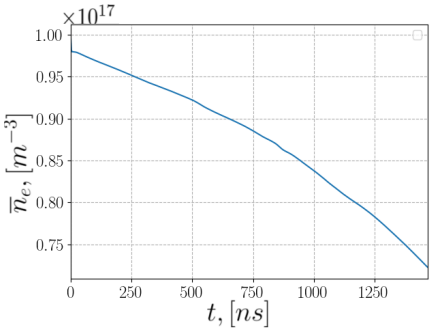

(a) Evolution of averaged electron density $\overline{n}_e$ over simulation time.

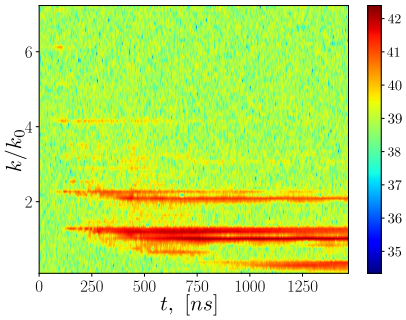

(b) Evolution of azimuthal electron density k-spectra.

Figure 4.57: Evolution of electron density.

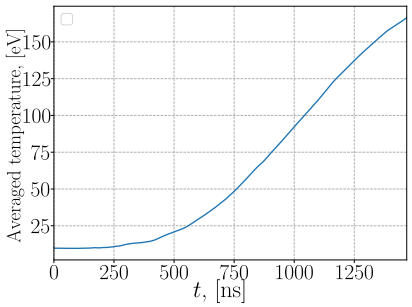

(a) Electron temperature over time.

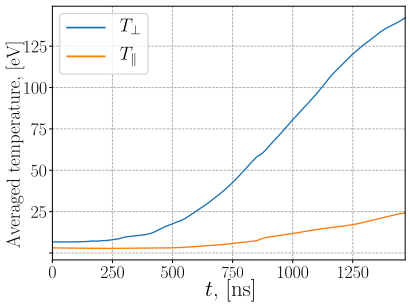

(b) Electron temperature components.

Figure 4.58: Electron temperature; dielectric boundary with $\varepsilon = 2$.

Figs. 4.56-4.58 show the electrostatic potential; electron plasma density and its spectra evolution, and the total electron temperature and its components, respectively.

4.2.2 DRUN-A15, azimuthal length, $L_\theta = 2\,\mathrm{cm}$, radial length, $L_r = 1\,\mathrm{cm}$, $\varepsilon = 2$

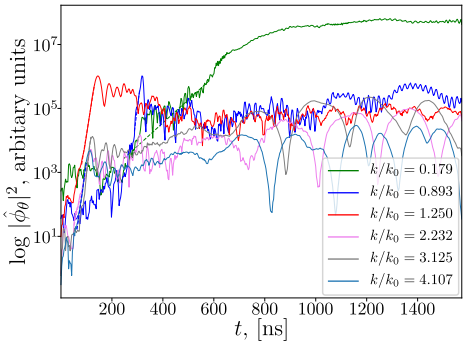

(a) Logarithmic amplitude of the azimuthal electrostatic potential energy $|\phi_\theta|^2$.

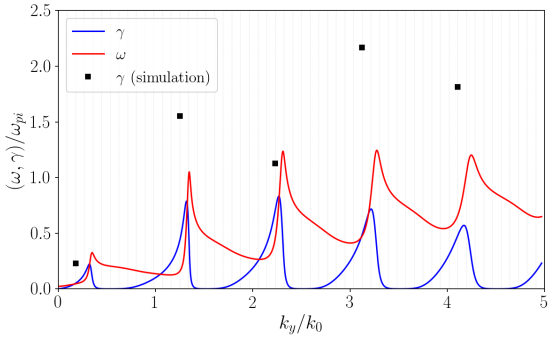

(b) Growth rate and frequencies for $k_z\lambda_{De} = 0.0233$.

Figure 4.59: Linear growth and nonlinear saturation of the cyclotron and the MTSI modes.

Fig. 4.59 shows the growth rates for the first four cyclotron modes are: $\gamma 1 = 1.556, \gamma 2 = 1.128, \gamma 3 = 2.169, \gamma 4 = 1.813$, and the MTSI mode with a $\gamma 0 = 0.229$. Figs. 4.60-4.62 describe the anomalous current value; the electron plasma losses, and the electrostatic potential spectra, respectively.

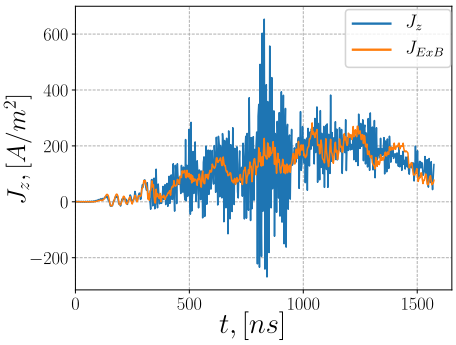

(a) Evolution of J_z and the current due to $\mathbf{E} \times \mathbf{B}$ drift.

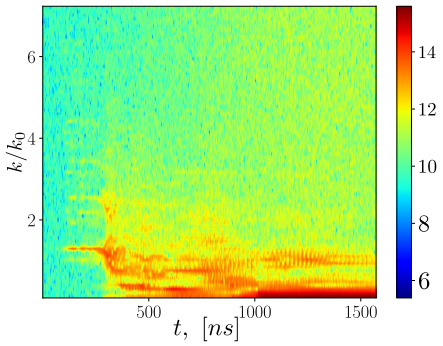

(b) Anomalous current k-spectra over time.

Figure 4.60: Evolution of J_z and due to $\mathbf{E} \times \mathbf{B}$ drift. Radial length, $L_r = 1\,\text{cm}$.

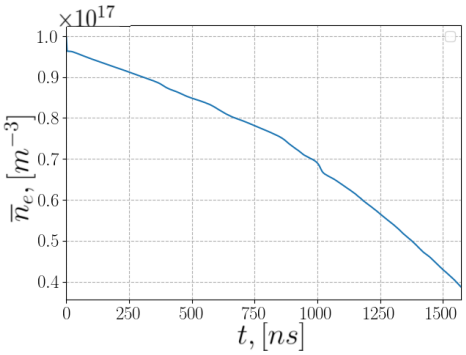

(a) Evolution of the averaged (in space) electron density $\overline{n}_e$.

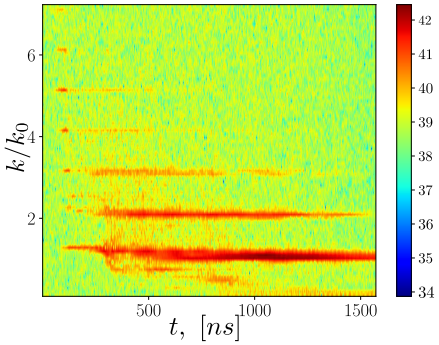

(b) Evolution of azimuthal electron density k-spectra.

Figure 4.61: Evolution of the electron density.

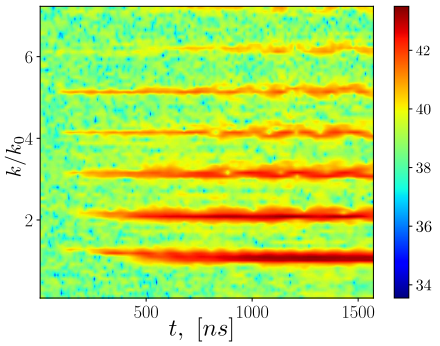

(a)

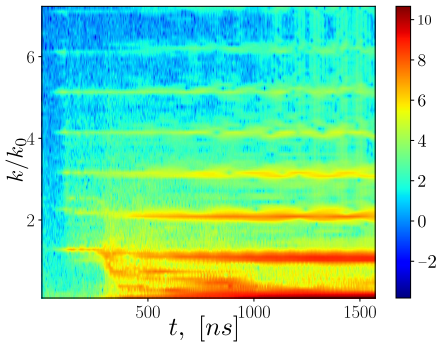

(b)

Figure 4.62: a) Evolution of the azimuthal ion density k-spectra b) electrostatic potential k-spectra.

4.2.3 DRUN-A16, azimuthal length, $L_\theta = 2$ cm, radial length, $L_r = 2$ $L_{r1} = 4$ cm, $\varepsilon = 2$

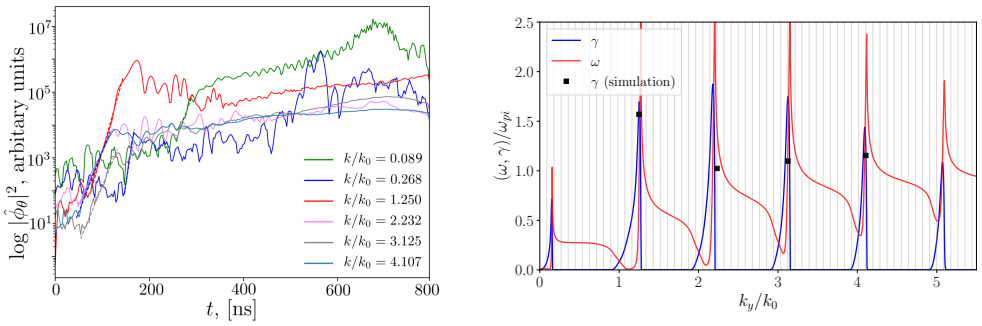

(a) **(b)**

Figure 4.63: Logarithmic amplitude of the azimuthal electric potential energy $|\phi_\theta|^2$. Linear growth and nonlinear saturation of the cyclotron and the MTSI modes.

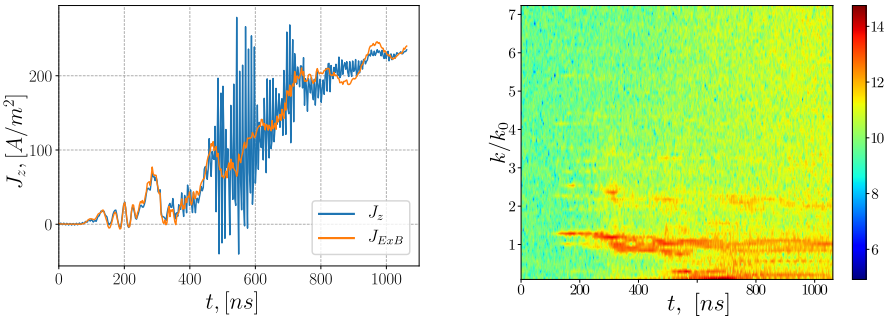

(a) Evolution of J_z and the current due to $\mathbf{E} \times \mathbf{B}$ drift.

(b) Anomalous current k-spectra over time.

Figure 4.64: Evolution of the axial electron current (ε=2).

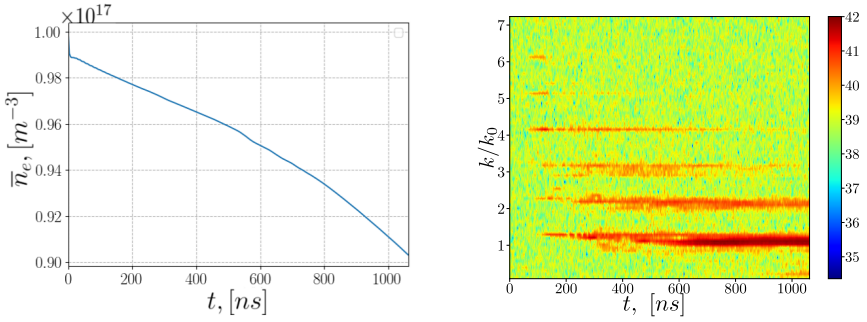

(a) Evolution of the averaged (in space) electron density $\overline{n}_e$.

(b) Azimuthal electron density k-spectra over time.

Figure 4.65: Evolution of electron density.

Figs. 4.63-4.65 show the power spectra of the azimuthal electric field; the anomalous current value, and the electron plasma losses, respectively.

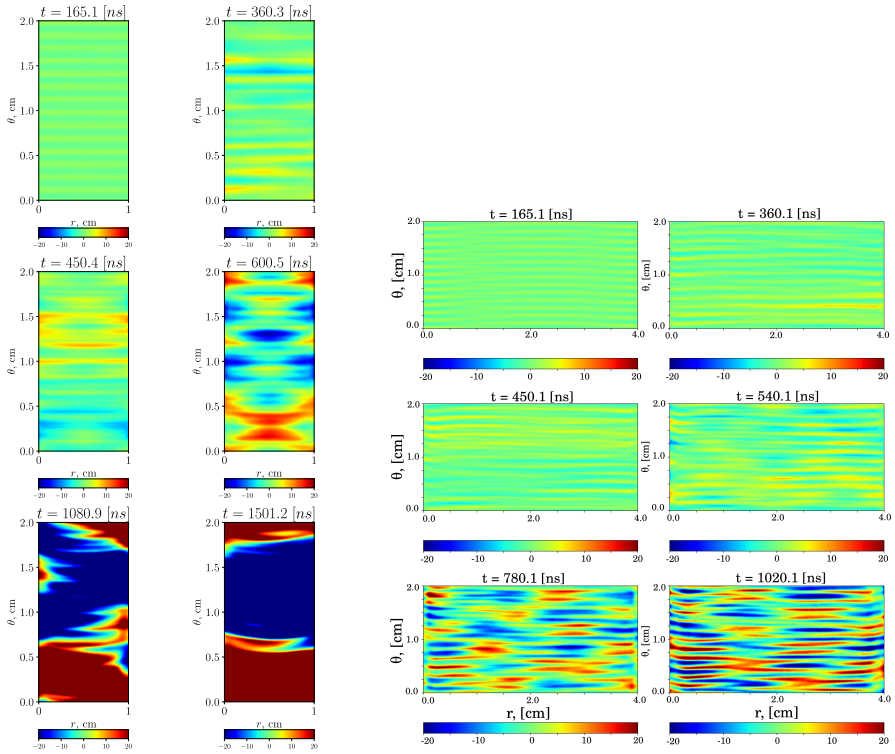

Figure 4.66: Nonlinear evolution of electrostatic potential fluctuations $\widetilde{\phi}$ in time; dielectric $\varepsilon = 2$ (a) $L_r = 1$ cm, (b) $L_r = 4$ cm.

Fig. 4.66 demonstrate the electrostatic potential spatial distribution for the cases with shorter and longer radial system length. The result is similar to the respective cases with metal walls (MRUN-A2, MRUN-A3).

4.3 REF-1, general case with reflecting walls

This simulation is the only case where reflecting boundary conditions are used for particles, but all other parameters were kept the same as in the base case. Reflecting walls refer to the case when particles undergo mirror reflection upon reaching a radial wall, i.e., their velocity component perpendicular to the wall change its sign (number of particles stays the same during the whole simulation). This is, that in all my previous simulations I had particle losses using either metal or dielectric walls with absorbing conditions for particles.

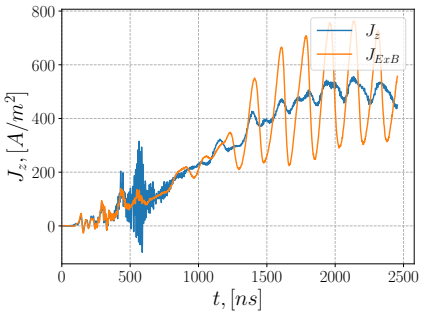

(a) Evolution of J_z and the current due to $\mathbf{E} \times \mathbf{B}$ drift.

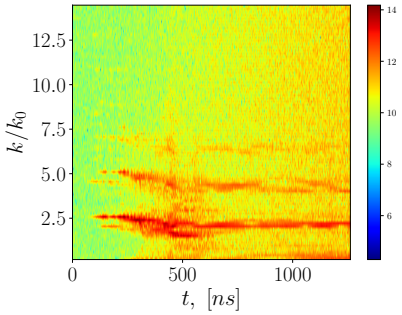

(b) Anomalous current k-spectra over time.

Figure 4.67: Evolution of the axial electron current.

For this case it is expected that the average plasma density will be constant during the whole simulation time as there are no particle losses (see Fig. 4.68). I run this case in order to check the effect of plasma losses on the development/saturation of the anomalous current. The overall result is that the electron anomalous current is higher than the value for the general case as shown in Fig. 4.67.

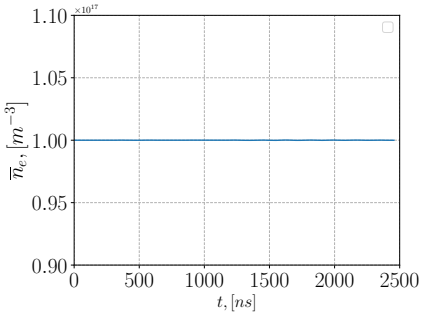

(a) Averaged electron density $\overline{n}_e$ over simulation time.

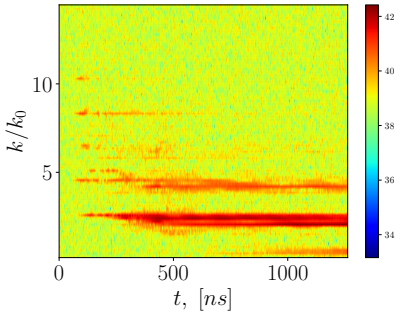

(b) Azimuthal electron density k-spectra over time.

Figure 4.68: Evolution of electron density.

4.4 Scaling PIC discussion and results

A parametric study was carried out for investigating the role of electric and magnetic field magnitudes, the boundary conditions, and finite-length on the mode development and the anomalous electron current. Therefore, forward in this section the insight of these differences will be exposed. PIC simulations were performed for typical parameters of the Hall-effect thruster in 2D azimuthal-radial geometry. The nature of the anomalous current is still not well understood, however, the saturated state of turbulence and resulting anomalous electron current are studied. I would like to re-mention the group name were used to categories the scaling studies:

- Group A – influence of the radial or azimuthal length.
- Group B – influence of the plasma density.

- Group C – influence of the axial electric field E magnitude.
- Group D – influence of the radial magnetic field B magnitude.
- Group E – influence of both the electric field E and the magnetic field B magnitude.

4.4.1 Cases description

General case with metal walls

MRUN-1. Azimuthal length, L_θ= 2 cm. Radial length, L_r= 2 cm. Metal walls boundary condition. B_0 = 200 G and E_0 = 200 V/cm. Numerical and plasma parameters for the general case are summarized in the Table 4.1.

Group A - Length scaling

MRUN-A2. Azimuthal-radial length, L_θ= 2 cm, and L_r= 4 cm. Note change in radial length.

MRUN-A3. Azimuthal-radial length, L_θ= 2 cm, and L_r= 1 cm. Note change in radial length.

MRUN-A4. Azimuthal-radial length, L_θ= 4 cm, and L_r= 2 cm. Note change in azimuthal length.

MRUN-A5. Azimuthal-radial length, L_θ= 1 cm, and L_r= 2 cm. Note change in azimuthal length.

Group B - Density scaling

MRUN-B6. Plasma density N = $N_0/2 = 5 \times 10^{16}\,\mathrm{m}^{-3}$.

MRUN-B7. Plasma density N = $2N_0 = 2 \times 10^{17}\,\mathrm{m}^{-3}$.

Group C - Electric field scaling

MRUN-C8. Electric field E = $E_0/2 = 100\,\mathrm{V/cm}$.

MRUN-C9. Electric field E = $2E_0 = 400\,\mathrm{V/cm}$.

Group D - Magnetic field scaling

MRUN-D10. Magnetic field B = $B_0/2 = 100\,\mathrm{G}$.

MRUN-D11. Magnetic field B = $2B_0 = 400\,\mathrm{G}$.

Group E - Electric and magnetic fields scaling

MRUN-E12. Electric and magnetic magnitudes: B = $B_0/2 = 100\,\mathrm{G}$ and E = $E_0/2 = 100\,\mathrm{V/cm}$.

MRUN-E13. Electric and magnetic magnitudes: B = $2B_0 = 400\,\mathrm{G}$ and E = $2E_0 = 400\,\mathrm{V/cm}$.

General case-dielectric walls

DRUN-14. The second general case has the same length parameters as the first general case.

DRUN-A15. Azimuthal-radial length, L_θ= 2 cm, and L_r= 1 cm. Dielectric walls, $\varepsilon = 2$. Note change in radial length.

DRUN-A16. Azimuthal-radial length, L_θ= 2 cm, and L_r= 4 cm, $\varepsilon = 2$. Note change in radial length.

DRUN-A17. Azimuthal-radial length, L_θ= 2 cm, and L_r= 4 cm, $\varepsilon = 4$. Note change radial length.

DRUN-B18. Plasma density N = $N_0/2 = 5 \times 10^{16}\,\mathrm{m}^{-3}$, $\varepsilon = 2$.

DRUN-B19. Plasma density N = $2N_0 = 2 \times 10^{17}\,\mathrm{m}^{-3}$, $\varepsilon = 2$.

DRUN-C20. Electric field E = $E_0/2 = 100\,\mathrm{V/cm}$, $\varepsilon = 2$.

DRUN-C21. Electric field E = $2E_0 = 400\,\mathrm{V/cm}$, $\varepsilon = 2$.

DRUN-D22. Magnetic field B = $B_0/2 = 100\,\mathrm{G}$, $\varepsilon = 2$.

DRUN-D23. Magnetic field B = $2B_0 = 400\,\mathrm{G}$, $\varepsilon = 2$.

General case-reflecting walls

REF-1. General case using reflecting boundary conditions instead of absorbing for the particles in the simulation.

Table 4.2: Simulation case numbers that correspond to a particular choice of boundary conditions or/and the system length.

Length / Boundary walls	L_θ=$L_r = 2$	$L_\theta = 2, L_r = 4$	$L_\theta = 2, L_r = 1$	$L_\theta = 4, L_r = 2$	$L_\theta = 1, L_r = 2$
$\varepsilon = \infty$	1	2	3	4	5
ε=2	14	16	15		
ε=4		17			

Table 4.3: E and B for $\epsilon = \infty$.

E, V/cm \ B, gauss	100	200	400
100	12	8	
200	10	2	11
400		9	13

Table 4.4: E and B for $\epsilon = 2$.

E, V/cm \ B, gauss	100	200	400
100		20	
200	22	14	23
400		21	

4.4.2 Scaling results

1. Decreasing the radial system length from $\mathrm{L}_r = 2\,\mathrm{cm}$ to $\mathrm{L}_r = 1\,\mathrm{cm}$, or increasing the radial length from $\mathrm{L}_r = 2\,\mathrm{cm}$ to $\mathrm{L}_r = 4\,\mathrm{cm}$, the anomalous current values remain similar. It is expected that plasma losses through the radial walls are larger for shorter radial lengths L_r. Ratio of sheath to system area is larger for shorter L_r. This result is observed in the simulations, see Figs. 4.15a, 4.6a, and 4.17b for the average electron density losses with time. Linear instability differs mostly for $L_r = 1\,\mathrm{cm}$ case, as the smallest k_z value increased, the growth rates values in the dispersion relation (MTSI and ECDI modes) are lower and with larger spread in k_z-values (see Fig. 2.6 for k_z effect).

2. The scaling of the applied external axial electric field, $\mathrm{E} = (100, 200, 400)$ V/cm, effectively changes the drift velocity of magnetized electrons, $V_D = E/B$. For the cases with metal walls, varying the applied electric field does not make notable difference in the anomalous current values.

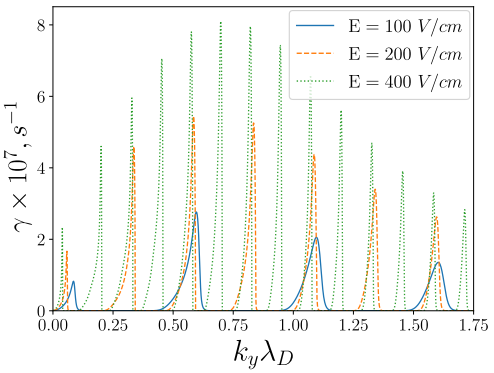

Figure 4.69: Growth rate values for various applied external electric field obtained by solving the dispersion equation (2.48).

For values of E = (100, 200) V/cm some radial structures are visible but the ECDI is the dominant mode. For E = 400 V/cm (or $V_D = 2 \times 10^6$ m/s) the MTSI is expected to have a larger growth rate. As a consequence, it is seen in the electrostatic potential (Fig. 4.41), some large MTSI-mode patterns appear and dominate the nonlinear regime. The electron density k-spectra evolution shows that with an increased applied E-field, more ECDI modes are involved, see Fig. 4.40b.

3. For metal walls, larger system length in the azimuthal direction values corresponds to a higher anomalous current value, smaller system length leads to a lower anomalous current.

4. For the cases with metal walls and varying the external magnetic field: B = (100, 200, 400) G, one can note that both the drift velocity V_D and the electron Larmor radius change with this variation. This affects the solutions of the dispersion equation, depicted in Fig. 4.70. Plasma losses are about the same, with slightly higher losses for the general case. For the case B = 100 G no radial structures are visible, while for B = 200 G these structures appear at the lowest mode $k_z = \pi/l_r$, then for the case B = 400 G we see a clearly radial structures that appear early after linear saturation and they remain in the nonlinear regime. This observation agrees with the solutions of the dispersion equation, Fig. 4.45b, the MTSI mode is the strongest for the case B = 400 G. Contrary to cases with varying E-field, the MTSI values shifts to a higher k-values (azimuthal direction). One can note that for B = 100 G the energy cascade is observed from higher to lower ECDI modes (not to the MTSI mode or lowest). The anomalous current has about the same amplitude in all cases, but for the case B = 400 G, it shows a very fast growth on a short time period, believed to be associated with the MTSI initial growth. Though, after the MTSI saturation the anomalous current drops to low values. A fast radial (parallel) electron heating takes place at this time.

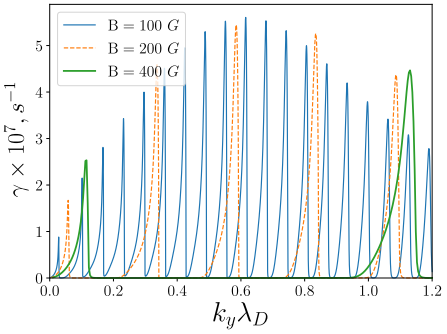

Figure 4.70: Growth rate values for various applied radial magnetic field obtained by solving the dispersion equation (2.48).

5. For metal walls, decreasing both B = 100 G and E = 100 V/cm (i.e. keeping the same drift velocity), the anomalous current becomes higher $J_z = 675$ A/m^2 than for the general case (B = 200 G and E = 200 V/cm which corresponds to $J_z = 200$ A/m^2).

6. There are no structure formations along the radial length when the drift velocity is $V_D = 0.5 \times 10^6$ m/s, but the structures appear when the drift velocity is $V_D = 1 \times 10^6$ m/s.

7. Using dielectric walls and B = 100 G, the anomalous current values are higher than those values using metal walls and B = 100 G.

8. Anomalous current values are higher when decreasing the magnitude of magnetic field. This is, for B = 100 G the anomalous current is higher than those using B = 400 G.

9. Decreasing plasma density N $= N_0/2 = 5 \times 10^{16}$ m^{-3} for both metal and dielectric walls, the value of the anomalous current is lower $J_z = 50$ A/m^2. Increasing plasma density N $= 2N_0 = 2 \times 10^{17}$ m^{-3} for both metal and dielectric walls, the value of the anomalous current becomes higher, $J_z = 1000$ A/m^2. Much higher values of anomalous current are observed when the plasma density is doubled, demonstrating the non-linear growth of J_z. Solutions of the dispersion equation (2.48) show that the ECDI is stronger for larger plasma density (Fig. 4.71), while the MTSI growth rate values stay the same.

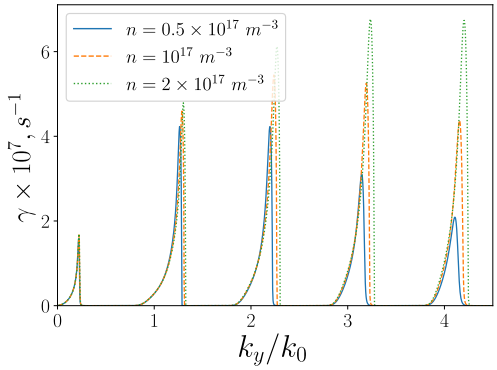

Figure 4.71: Growth rate values for various plasma density obtained by solving the dispersion equation (2.48).

It can be seen in Fig. 4.35a that for low density $N = 0.5 \times 10^{16}$ m^{-3} two modes (MTSI and ECDI) are about equally represented (distorted image) with more visible radial pattern, while in Fig. 4.35b and Fig. 4.4 for the $N = 1 \times 10^{17}$ m^{-3} and $N = 2 \times 10^{17}$ m^{-3} the ECDI mode clearly dominates in the no-linear regime.

5 Benchmark for $\mathbf{E} \times \mathbf{B}$ discharges

During my Master's research, I did participate in a collaborative benchmark work. For this benchmark project, I utilized the same 2D3V code I used for all my previous simulations. As it will be discussed below, this work confirmed the verification of this 2D3V code and consequently, my results from previous chapters are validated.

As a part of the LANDMARK (Low Temperature Magnetized Plasma Benchmarks) project, seven different groups from: Centre Européen de Recherche et de Formation Avancée en Calcul Scientifique, France (CERFACS), Laboratoire de Physique des Plasmas - École Polytechnique, France (LPP), The Laboratoire Plasma et Conversion d'Energie, CNRS and Universite de Toulouse, France (LAPLACE), The Institute for Plasma Science and Technology, Bari, Italy (ISTP), Standford University (USA), Ruhr University Bochum, Germany (RUB), and University of Saskatchewan, Canada (USASK), investigated the same physical phenomena for a radial-azimuthal setup using the same specified simulation parameters. Using independent explicit PIC codes, the results were collected and compared. As was explained in the previous chapters, partially magnetized plasmas immersed in crossed E × B are subject to plasma-wall interaction effects and instabilities. In this project, the idea was to capture the presence of the ECDI and MTSI instabilities for such E × B plasmas configuration, starting with simple cases. It is shown below, that varying the number of particles, the boundary conditions, and adding some features such as a source term and the virtual axial coordinate led to an incremental difficulty for the respective kinetic simulations. The results of this benchmark are presented in the paper published in Plasma Sources and Technology [32]. In this Chapter I will show some of my contributions to that benchmark work.

The Chapter is organized as follows: A brief description of the respective 2D3V PIC codes and the numerical setup for the simulations are presented. A few benchmark results are presented and shown in Section 5.2. Additionally, I have calculated the electron anomalous transport for this model and performed the scaling studies similar to those in Chapter 4.

5.1 Benchmark description

A general characterization for the tasks/progress during this project is as follows:

1. Without particle creation or injection, using metal walls as boundary condition: It was necessary to check if a steady state was reached or not. The azimuthal length L_y was changed as well to see the effect on the instabilities. With a smaller L_y the MTSI looks weaker and often disappears.

2. Without particle creation or injection, using specularly reflective walls. The use of absorbing walls produces a decrease in the plasma density, for this reason, reflecting walls were implemented to see the

wave interaction with the wall without the sheath. For this case, the number of particles was constant and it was needed only to control its energy.

3. Particle creation or injection, with virtual axial axis and metal walls. The virtual axial position in the system and other factors may lead to some numerical instabilities. Different possible values for the virtual axial extent could bring some effects such as, larger particle energy when the virtual axis length was too large. Thus, after a detailed investigation on choosing this value, the length L_z was set to 1 cm for this model.

   The goal for this model was to compensate particle losses at the walls and to control the gain in energy due to the axial electric field. The virtual axis was implemented as following: at the beginning of the simulation every particle had axial coordinate $z = 0$. The z-coordinate was calculated every time step using the forward Euler scheme: $z = z + \Delta t\ v_z$. When the particle coordinate is $|z| > L_z$ the particle (x, y, z) is relocated at $(x, y, z = 0)$. This is, the x, y locations are kept the same but the z-axis is refreshed.

   When a particle is relocated at $z = 0$, the velocities v_x, v_y, and v_z are sampled from a Maxwellian distribution with the respective temperature ($T_e = 10\,\text{eV}$, $T_i = 0.5\,\text{eV}$).
   The respective parameters for this virtual axial model are summarized in the Table 5.1.

Table 5.1: PIC simulations parameters.

Initial parameter	Value	Mesh parameter	Value
Magnetic field, B_0	200 G	Cell size, Δx	50×10^{-6} m
Electric field, E_0	10×10^3 V/m	Time step, Δt	1.5×10^{-11} s
Density, n_0	5×10^{16} m^{-3}	Virtual axis L_z	1 cm
Source, S_0	8.9×10^{22} s^{-1}m^{-3}	Cells in x-direction	256
Azimuthal length, L_θ	1.28 cm		
Radial length, L_r	1.28 cm		
Particles per cell	100, 200, 400		

The ionization profile is described as: the source term is positioned to have higher ionization in the center. The profile is uniform in azimuthal direction with a radial profile. The analytical equation for the source term reads

$$S(y) = S_0\ \cos\left(\pi \frac{y-\omega}{b-a}\right), \tag{5.1}$$

where a is the initial position and b is the end position of the source, $\omega = L_r/2 = a + b/2$. The particle coordinates then are chosen randomly from the ionization profile ($S(y)$ is inverted, x is sampled uniformly)

$$y_i = \arcsin\,(2\alpha - 1)(b - a/\pi) + \omega, \tag{5.2}$$

$$x_i = \beta\ L_\theta, \tag{5.3}$$

where α, β are the randomly sampled numbers on the interval [0,1]. The injected current J_0 is given by

$$J_0 = q \int_0^{L_r} S(y)dy = q\ S_0 \frac{2}{\pi}(b - a). \tag{5.4}$$

At each iteration, the number of macroparticles N_s, pairs of Xe+/e- to be injected in the domain is given by

$$N_s = L_\theta \, dt \int_0^{L_r} S(y) dy. \tag{5.5}$$

Thus, around 95.7 particles are injected at each iteration, that corresponds to $100\,\mathrm{A/m^{-2}}$, for the case of 100 particles per cell. Hence, for the simulation of 200 particles per cell, the injected particles corresponds to the same $100\,\mathrm{A/m^{-2}}$ so the source produced around 191.4 particles. Every simulation saturates with 177 and 414 particles per cell respectively, for 10 μs of simulation time.

5.2 Benchmark results

Among plenty of benchmark data, I will present some important results related with Chapter 4. First, it was checked that the simulations reach a steady state. A comprehensive test comparing the current density exiting the radial walls is shown in Fig. 5.1. A good agreement between three groups is observed, in all cases the average current leaving the system is roughly $100\,\mathrm{A/m^2}$, which is equal to the source influx.

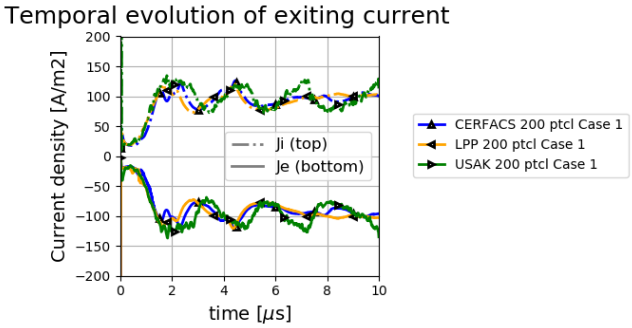

Figure 5.1: Total electron and ion currents exiting the system (via radial walls) as a function of time [Villafana, W., et al. Plasma Sources Science and Technology, 2021].

One of the codes convergence tests is demonstrated in Fig. 5.2, where the average ion plasma density evolution is plotted for a different number of macroparticles per cell: 100, 200, 400. Again, a close agreement between the groups, and also no notable difference in results for various number of macroparticles. This and other tests [32] suggest that the convergence is observed already for $N_p = 100$. Finally, the spectrum of the azimuthal electric field is compared against each other. All results show that ECDI mode in the electric field stays dominant long after the saturation is reached, i.e. deeply in the nonlinear regime.

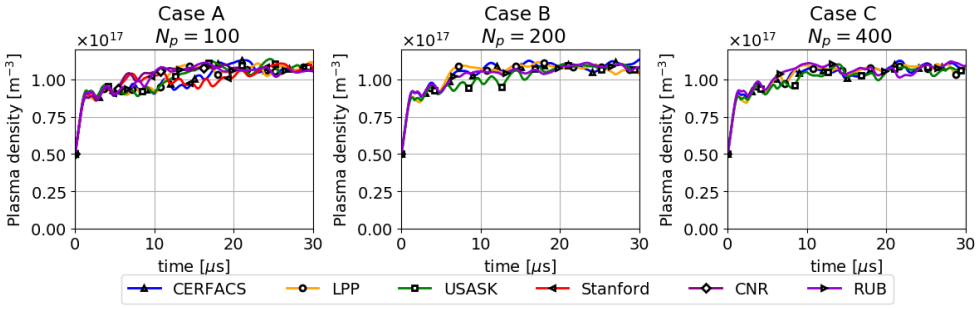

Figure 5.2: Temporal profile of plasma density up to 30 μs for different number of macroparticles N_p [Villafana, W., et al. Plasma Sources Science and Technology, 2021].

Overall few main modes were identified. First, the ion-sound like instability with a small wavelength below 1 mm. Further, in the radial direction a periodic pattern is visible, we identified it as the MTSI like instability. In Fig. 5.3 with the power spectrum over different time intervals, it is shown that up to 5 μs, the MTSI mode is more pronounced, even though both the ECDI and MTSI appear. In Fig. 5.4 one can see yet another good agreement between different groups in terms of the observed radial currents and electron temperature radial profiles.

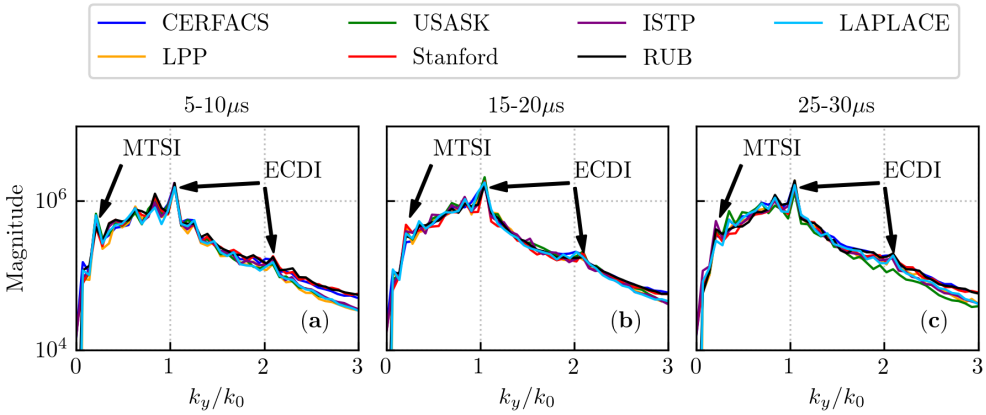

Figure 5.3: 1D azimuthal power spectrum of the azimuthal electric field E_x, averaged over all radial positions and over three temporal intervals: 5-10 μs (on the left), 15-20 μs, and 25-30 μs (on the right) [Villafana, W., et al. Plasma Sources Science and Technology, 2021].

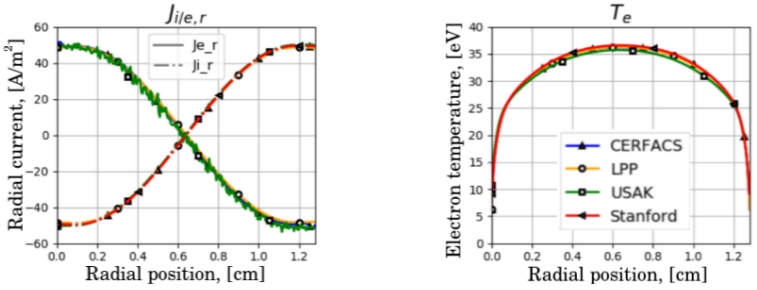

Figure 5.4: Radial profiles for (on the left) the electron/ion current (on the right) electron temperature [Villafana, W., et al. Plasma Sources Science and Technology, 2021].

5.3 Nonlinear development of ECDI, MTSI and anomalous transport

Even though in Chapter 4 I presented an extensive study of the ECDI and MTSI modes in a similar radial-azimuthal configuration, there are some differences with the setup used in this Chapter. The main differences include a virtual axial axis and a particle source term. Thus, the LANDMARK setup results in a stationary state solution due to the presence of the source term (compensating the density losses). Also, the virtual axial coordinate adds a mechanism for a heating saturation, absent in the simulations in Chapter 4 as well.

In this section I will discuss some results for the nonlinear development/saturation of ECDI and MTSI modes and the anomalous current (similarly to what I performed for the previous simulations) in this Chapter. Note that the LANDMARK group did not participate in this section nor in the scaling study in the next section 5.4. The choice of the simulation parameters (such as the azimuthal length and the drift velocity) for this study allows to capture both ECDI and MTSI instabilities development. Recall, that the ECDI mode can develop in one-dimensional setup [25] in azimuthal direction, while the MTSI is two-dimensional and require the parallel (to magnetic field) coordinate. The nonlinear interaction of these modes and its effect on the anomalous current is the main interest of this study. The corresponding power spectrum for the electron axial current density in Fig. 5.5 shows that the MTSI starts growing after the ECDI modes saturate and it grows to larger values (energy transfer to low-k modes), similarly to Chapter 4 results.

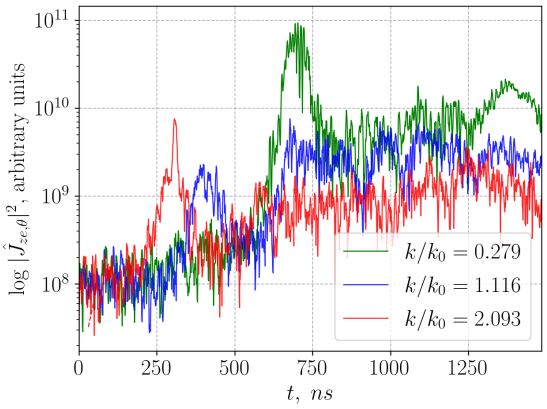

Figure 5.5: 1D power spectrum of the axial electron current (in azimuthal direction, fixed radial point $L_r/4$).

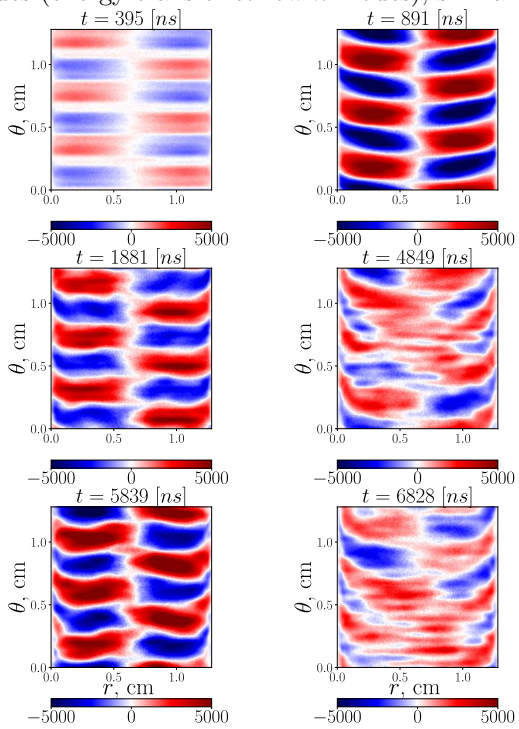

Figure 5.6: Electron axial current in space at various moments in time in the nonlinear regime.

The ECDI modes appear in the linear stage with the 2$^{\text{nd}}$ resonance to be more dominant, but later and in the nonlinear regime both 1$^{\text{st}}$ and 2$^{\text{nd}}$ resonances are about equally presented. It is seen that in the nonlinear regime, the dominant component in the axial electron current is due to the long-wave MTSI mode ($k = 0.140k_0$, where $k_0 = \omega_{ce}/v_0$), Fig. 5.6, also observed in Chapter 4. In the nonlinear stage the MTSI modes continue dominating (later stages will be shown below, where the trend is preserved). Note that the MTSI mode ($k = 0.28k_0$) here is the second lowest mode available in the simulation (for a given system length), suggesting that we do not observe a cascade to the lowest available mode (although a larger system length is required to reaffirm it). Also, a coupling between the MTSI mode and the 2$^{\text{nd}}$ resonance ECDI mode is observed (Fig. 5.10b), and it (MTSI/ECDI coupling) was also noted by S. Janhunen [12]. It explains the periodic distortions shown in the Fig. 5.6, when either both modes are equally presented or one (MTSI) dominates. It is interesting, that maximum values of the electron axial

current are observed (Fig. 5.6) for the moments when the MTSI mode dominates. But it is shown below that the spatially averaged electron axial current (which we call the anomalous electron current) correlates with the peaks of the ECDI mode present in the electric field.

For the azimuthal electric field we observe somehow different picture, the 2$^{\text{nd}}$ resonance ECDI mode dominates even in the nonlinear regime. Similar to the current spectra above, the MTSI mode starts to grow after Fig. 5.7. The spatial evolution of the azimuthal electric field, Fig. 5.8, confirms the ECDI mode dominance. Some weaker (lowest mode) radial dependence appears with time. At the end, I present the result that was not reported in the benchmark paper, which is the anomalous (axial) current $J_z = \langle J_z \rangle_{xy}$, averaged in space, as a function of time, Fig. 5.9.

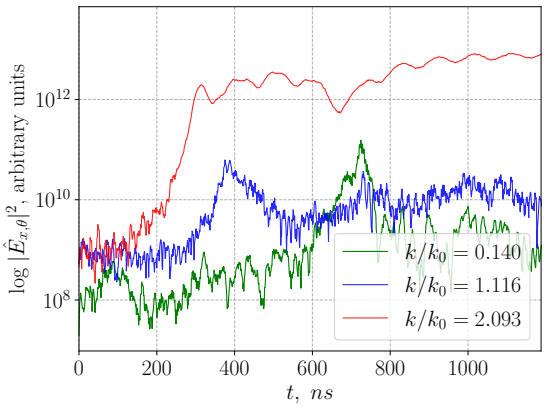

Figure 5.7: 1D power spectrum of the azimuthal electric field (in azimuthal direction, fixed radial point $L_r/2$).

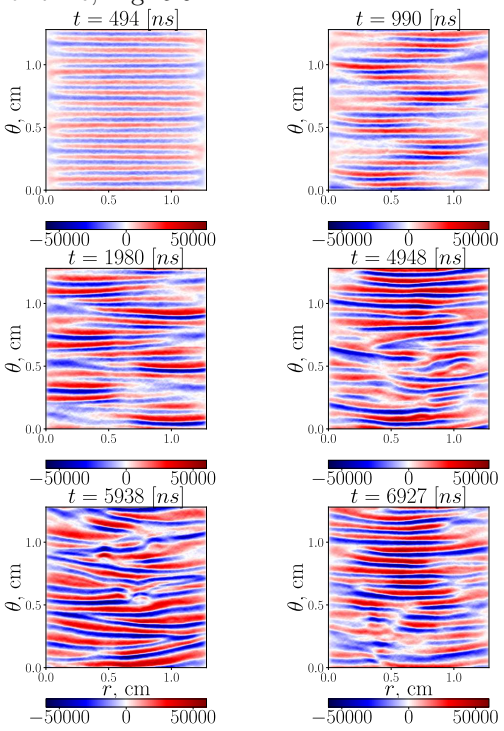

Figure 5.8: Azimuthal electric field in space at various moments in time in the nonlinear regime.

Both currents are in a good agreement, same as in Chapter 4. In simulation in Chapter 4, where the a steady state could not be achieved, the electron axial current appear correlating more with the growth of the MTSI mode in early nonlinear stages. However the results of this Chapter suggests contrary, local maximum of the anomalous current corresponds to the period of time when ECDI mode in the electric field spectra is the highest. It is reasonable as this current is clearly driven by the fluctuating azimuthal electric field $\widetilde{E}_\theta$. This behaviour was qualitatively observed in the results of Chapter 4, but due to plasma losses in time, it was difficult to make a stronger conclusion. Furthermore Fig. 5.9 may give some hints about the anomalous current behaviour with the ECDI/MTSI modes evolution in the non-linear regime Fig. 5.10.

As the axial current is clearly driven by $\widetilde{E} \times B$ force, and azimuthal electric field is mainly defined by the ECDI mode, Fig. 5.7, it is not of surprise that the axial current correlated with the ECDI mode in its spectrum. Note that a steady state for the electron current is observed, as well as a good agreement with the $\widetilde{E} \times B$ current, reinforcing the statement about the nature of this current as explained in Chapter 4.

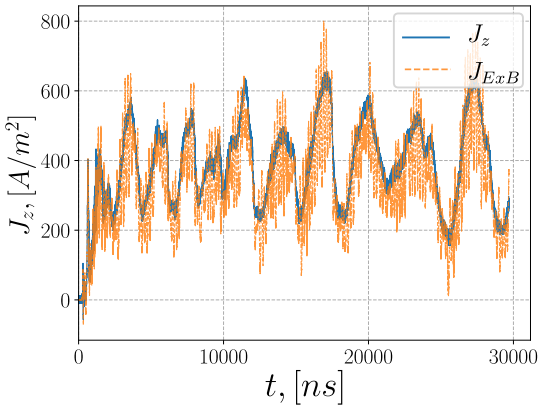

Figure 5.9: Anomalous current (averaged in space) in the LANDMARK configuration.

Like in Chapter 4, the axial electron current is compared against the current formed due to the fluctuating azimuthal electric field, $J_{E\times B} = q_e\langle n_e E\rangle_{xy}/B$.

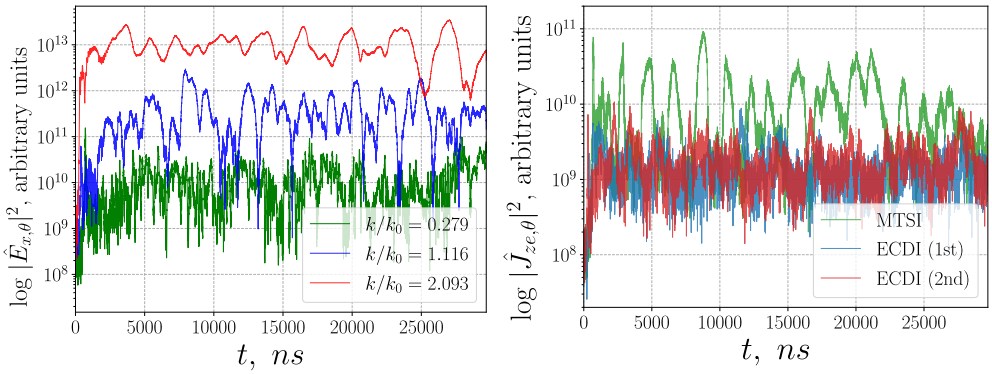

(a) **(b)**

Figure 5.10: Power spectrum of selected modes (MTSI and first two resonances of ECDI) of the azimuthal electric field (azimuthal direction, fixed radial point $L_r/2$) (a) and axial current (azimuthal direction, fixed radial point $L_r/4$), as they evolve in time.

Two features were added in order to reach physical steady state. The particle source with a constant influx (to mimic ionization) and the virtual axial length (to reduce heating). Every group in this benchmark study was able to get similar patterns for these instabilities.

5.4 Scaling studies with virtual axial length and particle source

In this section, I will present scaling studies similar to those in Chapter 4, as mentioned, the difference lies in the setup used, adding the virtual axial length and the particle source. The purpose of this scaling study is to investigate the evolution of the anomalous transport for these steady stage simulations. In the same way, changing some plasma parameters, the magnitude of the applied electric field, and the radial magnetic field. The parameters for the base/general case corresponds to the LANDMARK configuration

used in the previous section 5.1. Recalling these values: initial plasma density $N = 5 \times 10^{16}$ m^{-3}, magnetic field $B_0 = 200$ G, electric field $E_0 = 100$ V/cm, domain radial and azimuthal lengths are 1.28 cm.

5.4.1 Influence of external electric field

In this study the applied electric field was varied, given the following values: $E_0 = (50, 100, 200)$ V/cm; with a fixed applied magnetic field $B_0 = 200$ G. All these runs resulted in the steady-state solutions, i.e. density and other plasma variables fluctuate around their averaged value. The average values of the anomalous current (spatially averaged signal in time) obtained for various values of the applied electric field are shown in Fig. 5.12a. The anomalous current value is the highest for the case with drift velocity $V_D = E_0/B_0 = 0.5 \times 10^6$ m/s, this is for the base case, $E_0 = 100$ V/cm, and it is about the same value for the two other cases. With respect to the average plasma density, the case with the highest drift velocity $V_D = 1 \times 10^6$ m/s has the lowest saturated density $N = 6.5 \times 10^{16}$ m^{-3}, i.e. higher plasma losses through the walls (Fig. 5.12b).

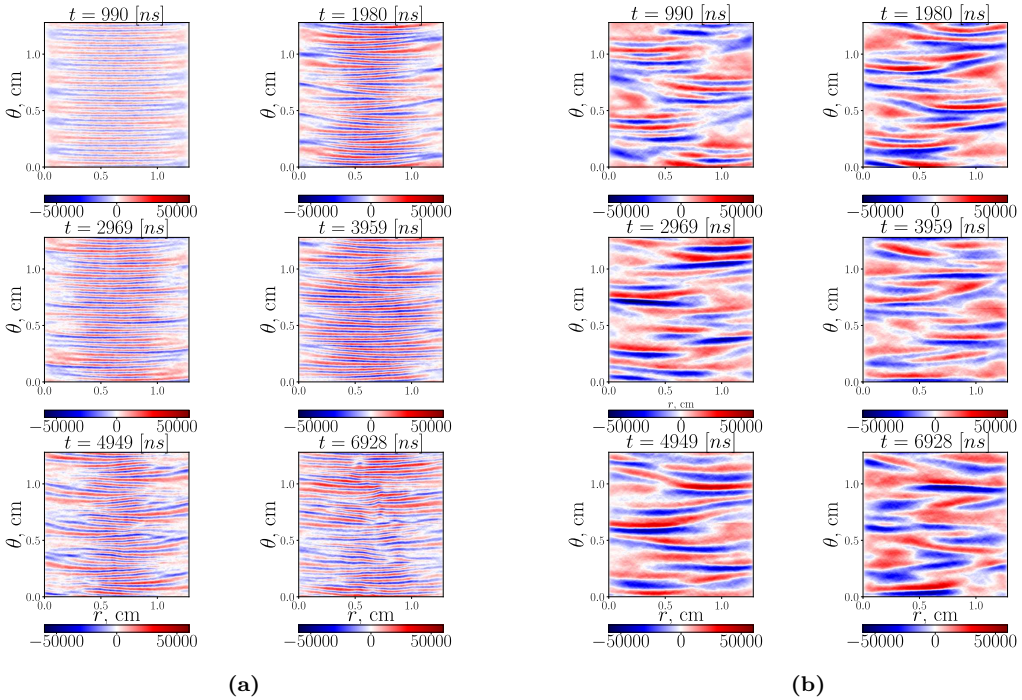

Figure 5.11: Nonlinear evolution of azimuthal electric field, $E_0 = 50$ V/cm (a), $E_0 = 200$ V/cm (b).

In Fig. 5.11 one can see the difference between the nonlinear evolution of the self-consistent azimuthal electric field varying the external electric field. The unstable modes (both ECDI and MTSI) shift to the lower-k region for a larger drift velocity. Hence, we observe larger in size structures for a higher (applied) electric field. This is consistent with the solutions of the kinetic dispersion equation, Fig. 4.69, both the MTSI and ECDI modes have larger growth rate for a larger drift velocity. It is believed that radial heating and thus increased losses are caused mainly by the MTSI mode, which explains Fig. 5.12b where the highest losses are observed for the highest applied E-field.

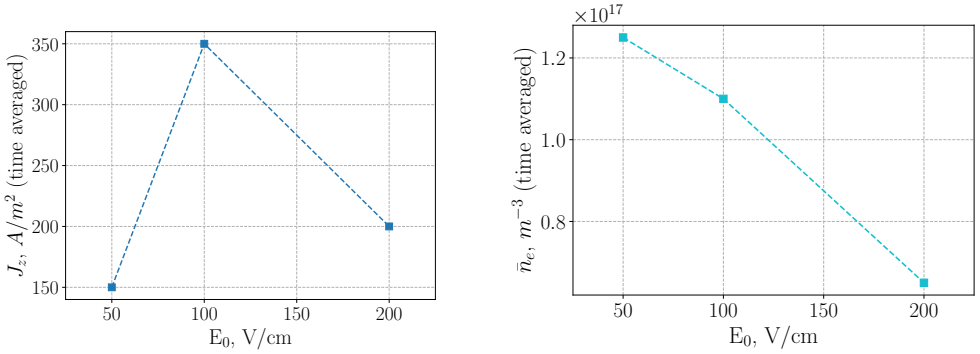

(a) **(b)**

Figure 5.12: Scaling evaluation for the anomalous current (a) and averaged plasma density (b) varying the external electric field. Note that these spatially averaged quantities are averaged over time when simulation saturated.

5.4.2 Influence of the radial magnetic field

In this study the applied magnetic field was varied, given the following values: $B_0 = (100, 200, 300, 400)$ G; with the fixed applied electric field $E_0 = 100\,V/cm$. The time averaged (saturated) anomalous electron current values for these cases are shown in Figs. 5.13a. It is seen that the anomalous current decrease with increasing B_0, with a particularly high value ($2500\,A/m^2$) in the case when $B_0 = 100\,G$, about one order higher than the other cases. Also, higher plasma losses are observed for higher B_0 values, Fig. 5.13b.

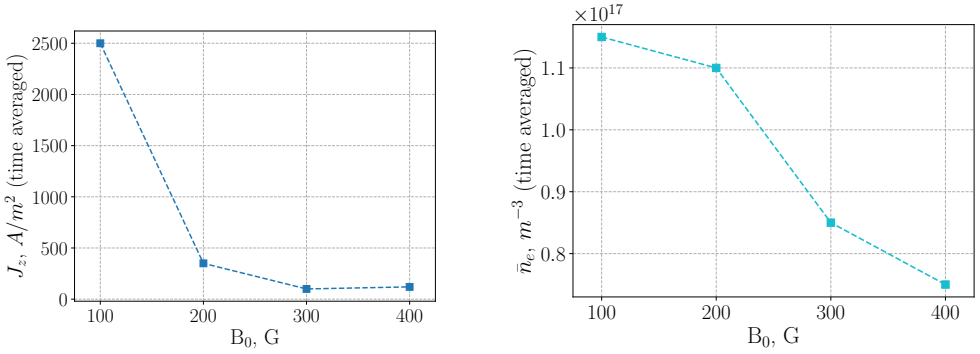

(a) **(b)**

Figure 5.13: Scaling evaluation for the anomalous current (a) and averaged plasma density (b) varying the external magnetic field. Note that these spatially averaged quantities are averaged over time when simulation saturated.

The solution of the kinetic dispersion equation suggests (Fig. 4.70) that for a higher B_0 the MTSI mode is the strongest, which possibly explains higher losses, similar to the electric field scaling study. Two-dimensional azimuthal electric field structures can be seen in Figs. 5.14 for cases with $B_0 = 100\,G$ and

$B_0 = 300\,G$. The case with $B_0 = 100\,G$ shows highly turbulent behaviour in the radial direction (larger k_z modes), which does not appear in the other simulations.

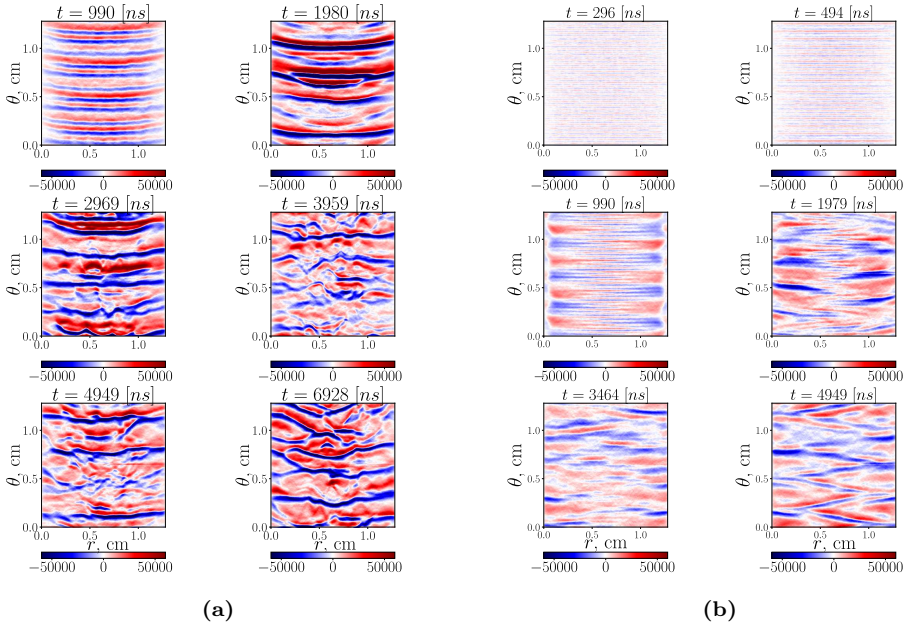

Figure 5.14: Nonlinear evolution of azimuthal electric field, $B_0 = 100\,G$ (a), $B_0 = 300\,G$ (b).

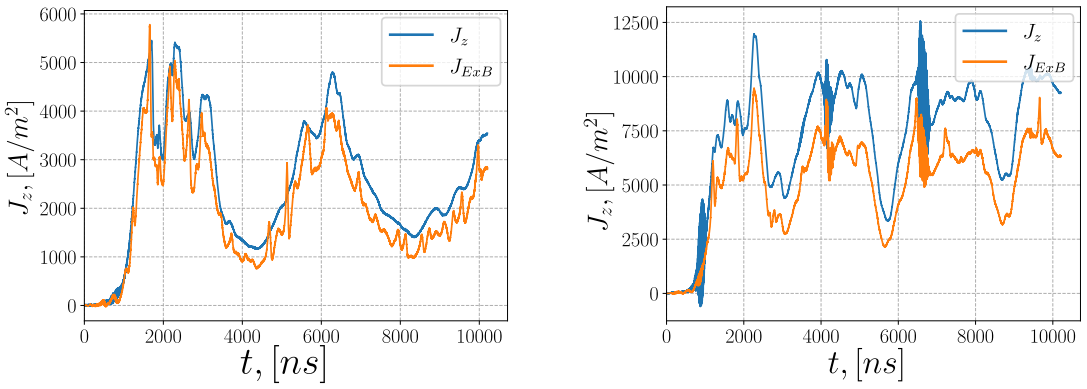

(a) $E_0 = 100\,V/cm, B_0 = 100\,G$ **(b)** $E_0 = 200\,V/cm, B_0 = 100\,G$

Figure 5.15: Effect of partial demagnetization.

Analyzing the electron axial current J_z, for cases in Fig. 5.15, it was noted that the current $J_{E_\theta \times B}$ can not fully explain this axial current, but it still correlates well and represent the most part of the current. I believe this is caused by a partial demagnetization, i.e. due to more turbulent non-linear dynamics (chaotic structures) when $B = 100\,G$. Particles can effectively become demagnetized when the internal electric field structures are of the size smaller than the gyroradius. For example, for the base case the electron average temperature is 30 eV which makes the gyroradius $\rho \approx 1\,mm$. For the case with $E = 100\,V/cm$, $B = 100\,G$

has $\rho \approx 2\,\text{mm}$ and observed electric field structures of the size 1 mm or smaller (third ECDI resonance and higher).

For a larger applied electric field (E = 200 V/cm) one can see even more discrepancy between these currents. The spectral analysis of the azimuthal electric field (2D FFT) shows the development of the MTSI and ECDI modes at nonlinear regime.

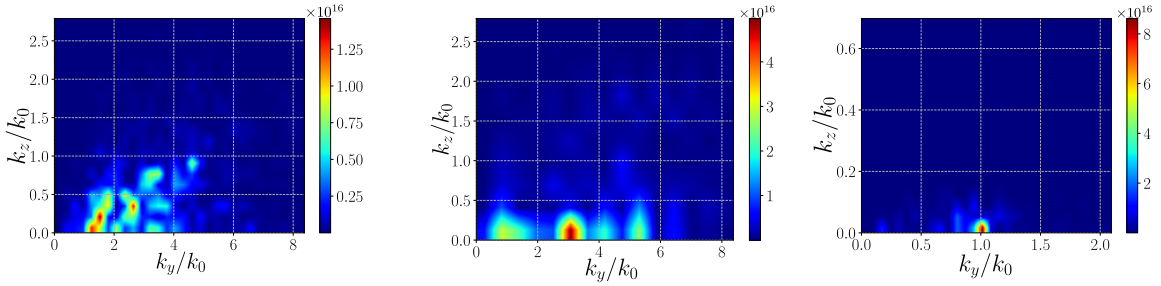

(a) $E_0 = 100$ V/cm, $B_0 = 100$ G

(b) $E_0 = 200$ V/cm, $B_0 = 100$ G

(c) $E_0 = 100$ V/cm, $B_0 = 200$ G(base case)

Figure 5.16: 2D FFT of the azimuthal electric field at time t= 7.5 μs for three cases.

From Fig. 5.16, where the power spectrum for the electric field is shown, one can identify a clearly radial structures in the non-linear regime for two cases: with $E_0 = 100$ V/cm, $B_0 = 100$ G, and with $E_0 = 200$ V/cm, $B_0 = 100$ G. However, for the base case $E_0 = 100$ V/cm, $B_0 = 200$ G, the first cyclotron mode is dominant and no radial structures are significant. I believe this is related to the presence of radial turbulent structures in the azimuthal electric field shown in Fig. 5.14 for a lower radial magnetic field. Note that for the base case the anomalous electron current can be explained due to the $E_\theta \times B$ drift in the axial direction, while it is not fulfilled for a lower magnetic field case, when a partial demagnetization is exposed.

6 Significance of noise in kinetic simulations

This Chapter is devoted to the project conducted by our research group that started as a benchmark study between Vlasov and PIC simulations for the Buneman-type drift instability. Buneman-type instabilities arise in the presence of relative drift velocity between electrons and ions in unmagnetized plasmas. When the drift velocity v_0 is low, of the order of the electron thermal velocity $v_0 \sim v_{th}$ (ion-sound instability), such setup leads to a weak turbulence regime, as it will be shown below with the kinetic dispersion relation. Higher relative drift setup is typically refereed as the Buneman drift instability. The goal of the benchmark work initially was to simulate the low-drift instability with $v_0 = 2v_{Te}$, but we realized that the noise problem heavily affects PIC results in such regime, resulting in an inability to reproduce the linear regime of this instability. Thus, another case with the drift velocity $v_0 = 6v_{Te}$, that belongs to the Buneman regime (stronger instability), was added to this study. The details of this problem and part of my contribution are reflected below. Also, this study is prepared for publication [33].

Statistical noise is a well-known problem for PIC approach in plasma simulations [15]. General approach that allows to reduce the noise is to increase a number of macroparticles and/ or use another type of particle loading (so called quiet start). Pseudo-random number generators typically used to sample a given distribution function (e.g. Maxwellian), and they are known to produce noise levels that are scaled as $\sim 1/\sqrt{N}$ (where N is the number of macroparticles). It means that achieving a low noise initialization can be difficult, requiring enormous number of simulated particles. On the other hand, the quiet start technique utilizes properties of low-discrepancy number sequences. Some reports show that noise levels for a quiet start scales as $\sim 1/N$ [15], and I will demonstrate it below as well. Alternatively to PIC low noise techniques, direct Vlasov solver can be applied to this problem due to its noiseless property. Three codes are exploited here to demonstrate the results: VSim - a proprietary PIC code (developed by Tech-X), XES1 – open-source 1D3V particle-in-cell code developed in "Plasma Theory and Simulation Group at Berkeley" (headed by Prof. C.K. Birdsall); and the direct Vlasov 1D3V solver, implemented in BOUT ++. I used the XES1 code as it has a built-in quiet particle loading. So I will refer to these codes as the PIC with random start, the PIC with quiet start, and the Vlasov code. Simulations and results from the Vlasov code are obtained and shared by O. Chapurin. The simulation setup, besides the drift velocity, will be the same. The system length corresponds to 6 mm, electron and ion temperatures are equal, $T_i = T_e = 2\,\mathrm{eV}$, and Hydrogen ion mass is used. Periodic boundaries are applied in the spatial domain. The electron drift velocity is either $v_0 = 2\ v_{Te}$ (low drift velocity) or $v_0 = 6v_{Te}$ (high drift velocity). Simulation time step was set to dt $= 0.004/\omega_{pe}$. Number of cells in PIC codes is set to 2048. Vlasov simulations used 2048 cells for the spatial domain, and 2000 cells for the velocity domain.

The Chapter is organized as following: I will start with the dispersion equation for the Buneman instability and show solutions for $v_0 = 2v_{Te}$ (low drift velocity) and $v_0 = 6v_{Te}$ (high drift velocity). Then I will present the results form PIC code (initialized with random start) for the high drift velocity, showing its well agreement with linear theory even for relatively low number of simulated particles. Then, for the low drift velocity case it is shown that PIC (random start) simulation results in a very poor agreement with theory. On the other hand, direct Vlasov kinetic solver will give a perfect agreement with linear theory. I will also show that the quiet start (particle loading with low-discrepancy sequences) technique can significantly reduce the statistical noise and also reproduce the linear instability of the low drift velocity case. At the end a quantitative noise estimates are compared for the quiet start and the random start PIC approaches. Thus, we illustrated the significance of the noise in kinetic simulations by examining the weak Buneman-type instability.

6.1 Linear theory

A type of instability caused by counter-streaming charged particles when electrons move relative to ions was first described by O. Buneman [34]. Collisionless plasma is assumed, with electron drift velocity v_0 relative to ions. The linear instability for Buneman-type configuration can be studied with the kinetic electrostatic dispersion equation with two species moving relative to each other

$$1 + \sum_{\alpha=i,e} \frac{1}{k^2 \lambda_{D\alpha}^2} \mathrm{Z}' \left(\frac{\omega - k v_{0\alpha}}{\sqrt{2} k v_{T\alpha}} \right) = 0, \tag{6.1}$$

where $\lambda_{D\alpha} = T_\alpha / 4\pi n q_e^2$, $v_{T\alpha}^2 = T_\alpha / m_\alpha$, and $\alpha = i, e$ stands for ions and electrons, respectively; $v_{0e} = v_0$, $v_{0i} = 0$. Solutions for the two cases of the dispersion equation (6.1) are depicted in Fig. 6.1.

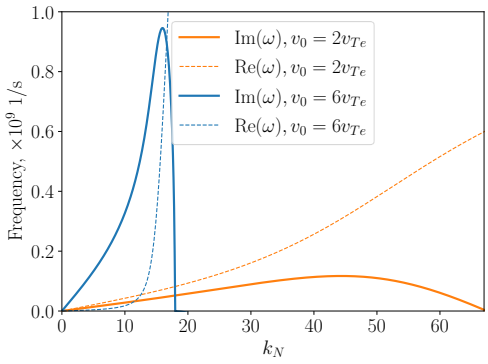

Figure 6.1: Real and imaginary components of the frequency solution of the dispersion equation (6.1) for the low and the high drift velocities. Note that the growth rate for the high drift velocity is about one order higher than for the low drift.

From these solutions the following modes are selected for the calculations of the growth rates:

$kL/2\pi$	$\gamma \times 10^8,\ 1/s$	$\omega \times 10^8,\ 1/s$
30	0.90	1.61
37	1.08	2.24
44	1.17	3.04
51	1.07	3.96

(a)

$kL/2\pi$	$\gamma \times 10^8,\ 1/s$	$\omega \times 10^8,\ 1/s$
14	7.08	1.45
15	8.67	3.20
16	9.46	6.41
17	8.13	10.6

(b)

Table 6.1: Growth rates and frequencies for selected mode numbers for the case of low drift velocity $v_0 = 2v_{Te}$ (a) and high drift velocity $v_0 = 6v_{Te}$ (b).

The growth rates of these modes will be measured in the following simulations for comparison between each other and theory. Note that the most unstable mode number for the low drift velocity case is 44, while for the high drift velocity it is 16 for the given configuration. Fluid limit (high drift velocity) solutions can also be obtained with:

$$1 - \frac{\omega_{pi}}{\omega^2} - \frac{\omega_{pe}}{(\omega - kv_0)^2} = 0, \tag{6.2}$$

where $\omega_{pi}^2/\omega_{pe}^2 = m_e/m_i$ is a small quantity, it can be found that the maximum growth rate [35]:

$$\mathrm{Im}\,(\omega) = \frac{\sqrt{3}}{2}\left(\frac{m_e}{2m_i}\right)^{(1/3)}\omega_{pe}, \tag{6.3}$$

which gives the largest growth rate $10^9\,\mathrm{s}^{-1}$ for our setup, close to the solution from the kinetic dispersion relation ($0.946 \times 10^9\,\mathrm{s}^{-1}$).

6.2 High drift velocity

As it was mentioned above, in the case of high drift velocity ($v_0 = 6v_{Te}$) PIC approach with random particle loader can well reproduce this regime. Fig. 6.2 demonstrates selected modes and their growth rates, the results are summarized in the Table 6.2.

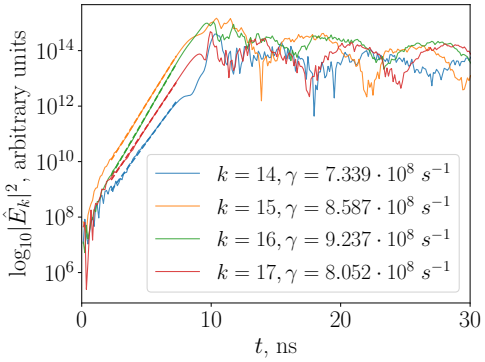

Figure 6.2: The evolution of selected modes of the electric field spectra and respective growth rates for randomly initialized PIC with $v_0 = 6v_{Te}$.

$kL/2\pi$	Theory, $\gamma \times 10^8,\ 1/s$	Simulation, $\gamma \times 10^8,\ 1/s$	Relative error, %
14	7.08	7.339	3.5
15	8.67	8.587	1.0
16	9.46	9.237	2.4
17	8.13	8.052	1.0

Table 6.2: Comparison between theory (predicted by the dispersion equation) and randomly initialized PIC simulation (10 000), the growth rate values for the case of high drift velocity.

Even though 10 000 particles per cell were used here, we used 1000 or below and we still obtained a good results for this regime, implying that the noise level is not very critical for this setup.

6.3 Low drift velocity

The case with low drift velocity ($v_0 = 2v_{Te}$) is the central problem in this Chapter, and it will be tackled with various approaches, random start PIC, quiet start PIC, and also with direct Vlasov solver. First, the results of PIC simulations with random start are presented, with various number of macroparticles per cell: 10 000, 100 000, Fig. 6.3.

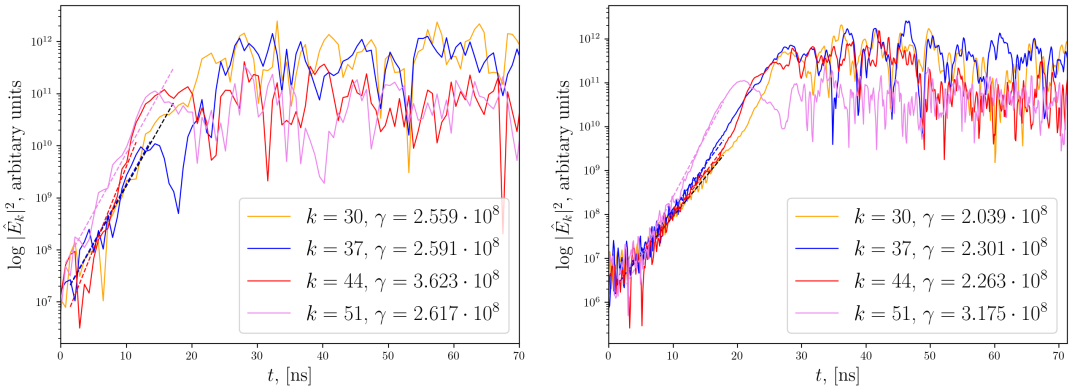

Figure 6.3: The evolution of selected modes of the electric field spectra and respective growth rates with randomly initialized PIC and number of macroparticles per cell: 10 000 (left), 100 000 (right). Note small improvement in the measured values of the growth rates as number of macroparticles increased by one order.

A conclusion at this point is that even with a large number of simulated particles (100 000 macroparticles per cell that corresponds to a total of 0.2 billions) the randomly initialized PIC can not reproduce the linear instability. The comparison table is obviously not needed here, the measured values are off by more than 100% (they are 2-3 times larger than predicted by the linear theory).

Now we discuss the major physical differences between two cases, high and low drift velocities for the

Buneman-type instability. In the case with lower drift velocity, the electron distribution function (EVDF) overlaps with the phase velocity of the main electrostatic mode (most unstable mode) which has the phase velocity $v_{ph} \sim c_s$. Thus, the mechanism of the instability is mainly of the resonance type, due to the inverse Landau interaction. In this case, the shape of the EVDF and any present noise could easily affect the results of the linear instability. On the other hand, in the case of high drift the EVDF is "shifted" further away while the phase velocity is about the same. In this way, this regime can be called the reactive (or fluid) [35], it is when the whole population of electrons is involved in the instability, and so the shape of EVDF plays lesser role (fluid regime). To provide more evidence that the low-drift case instability mechanism is due to the Landau damping, Fig. 6.4a demonstrates the growth rates for various ion masses (Helium, Hydrogen, and artificially small ion with $m_i = 40\ m_e$). Varying the ion mass, the phase velocity shifts to the higher values where $\partial f_0/\partial v$ increases (before the inflection point), and thus the growth rate increases. Phase velocities are calculated as $v_{ph} = \mathrm{Re}(\omega)/k$ from the dispersion relation for the most unstable modes. The corresponding phase velocities are $v_{ph} = 0.018\ v_{Te}$ (Helium), $v_{ph} = 0.035\ v_{Te}$ (Hydrogen), $v_{ph} = 0.223\ v_{Te}$ ($m_i = 40\ m_e$). Also, the PIC (random start) simulation with $m_i = 40 m_e$ and the low drift velocity shows that the observed trapping of electrons is due to this wave-particle interaction, Fig. 6.4b.

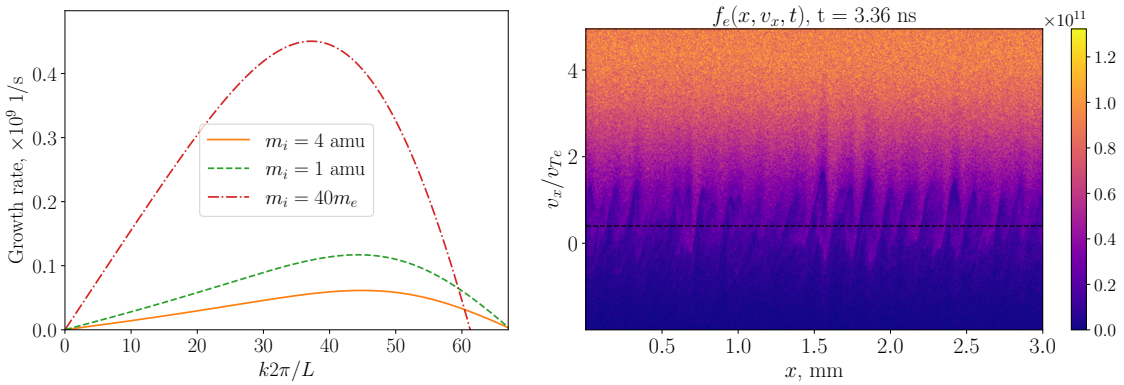

(a) **(b)**

Figure 6.4: Solutions to the dispersion relation (6.1) for the low-drift case and various ion masses (a). Trapped electron structures for the case with $m_i = 40 m_e$ (b); the distribution function f is evaluated from the particle phase space and normalized: $\int \hat{f}_e \mathrm{d}v_x = 1$.

We now continue with the case where the Hydrogen mass is used ($m_i = 1\,\mathrm{amu}$) and demonstrate the PIC with the quiet start and Vlasov simulation results for the low drift case, Fig. 6.5. Quiet start in PIC is generated utilizing the bit-reversed sequence [15]. It is done by sampling the microscopic velocities (by inverting the cumulative distribution function) using the uniform sequence of number instead of random numbers and the bit-reversed sequence is employed to generate positions for each particle. The Vlasov simulation is initiated with a small perturbation to the electron distribution function, $f_e(x, v, t = 0) = (1 + \epsilon \cos(x)) f_M(v)$, with $\epsilon = 10^{-10}$, where $f_M(v)$ is the 1-d Maxwellian distribution. The measured growth

rates are summarized in the Tables 6.3,6.4.

It is seen that the low-noise Vlasov simulation has no problems reproducing the linear regime, and PIC simulations with the quiet start also shows a better values (in compare to randomly initialized PIC) even with lower number of particles per cell. Hence, it is demonstrated that the initial noise in the simulation plays a major role for the low-drift case.

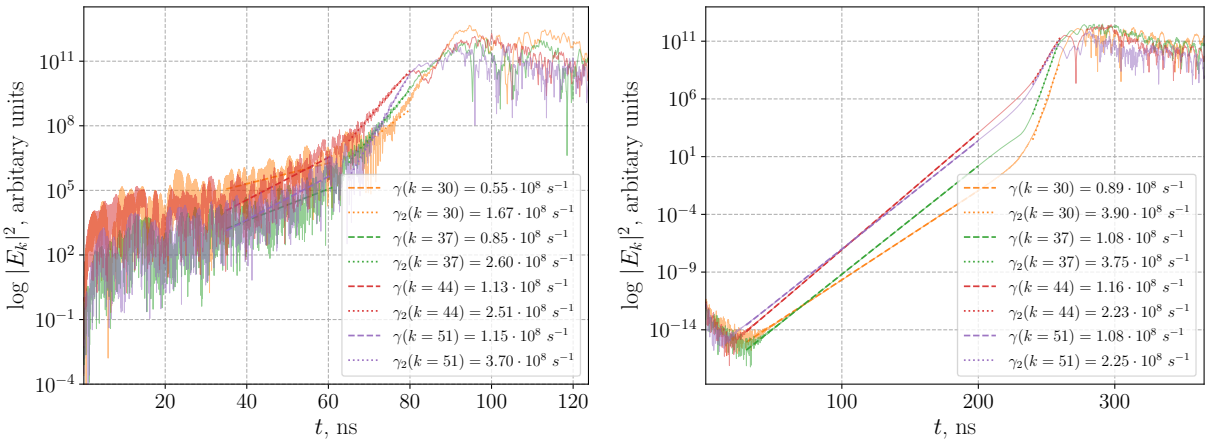

(a) Quiet start PIC with 10k.

(b) Vlasov simulation by O. Chapurin.

Figure 6.5: The evolution of selected modes of the electric field spectra.

The measured growth rates are summarized in the Tables 6.3-6.4 below.

Table 6.3: Comparison between theory (predicted by the dispersion equation) and the quiet start PIC simulation (10 000 particles per cell), values for the case of low drift velocity.

$kL/2\pi$	Theory, $\gamma \times 10^8,\ 1/s$	PIC (quiet start), $\gamma \times 10^8,\ 1/s$	Relative error, %
30	0.90	0.55	38
37	1.08	0.847	22
44	1.17	1.13	3
51	1.07	1.15	7

Table 6.4: Comparison between theory (predicted by the dispersion equation) and the low-noise Vlasov simulation, the growth rate values for the case of low drift velocity.

$kL/2\pi$	Theory, $\gamma \times 10^8,\ 1/s$	Vlasov, $\gamma \times 10^8,\ 1/s$	Relative error, %
30	0.90	0.89	1
37	1.08	1.08	0
44	1.17	1.16	0.8
51	1.07	1.08	0.8

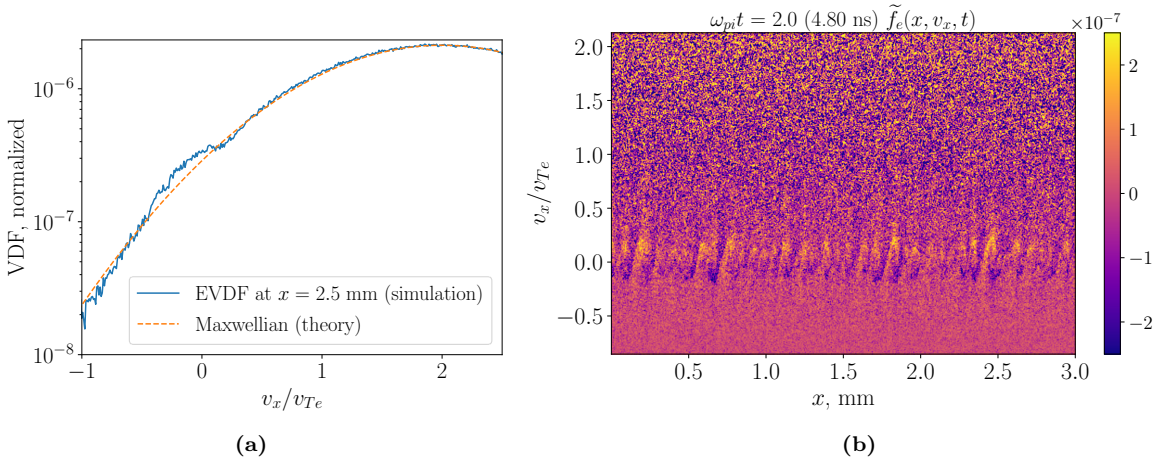

(a) **(b)**

Figure 6.6: Slice of the EVDF at 9.6 ns during the low-drift Buneman instability development as seen in the PIC (random start) (a). Trapped electron structures (b) that arise shortly after simulation starts in the PIC simulation (random start), with 10 000 particles per cell. The distribution function f is evaluated from the particle phase space and its perturbed part is plotted, $\widetilde{f} = f - f_{Maxw}$.

In the case with low drift velocity the flattening of the EVDF occurs due to resonance effects, see the slice of EVDF in Fig. 6.6. In the phase space it is interpreted as electron trapping Fig. 6.6b. Electrons with velocities close to the phase velocity of the wave are captured by the wave. We also observed that right after the EVDF flattening the "accelerated" growth appears, with the growth rate few times higher than that of the linear theory prediction. It can be clearly seen in Vlasov simulations results, Fig. 6.5. Note that a mode growth due to the linear instability in the Vlasov simulation "accelerates" somehow abruptly in time. One can solve the dispersion equation (6.1) with a slightly perturbed Maxwellian (to mimic flattening effect) from which it can be seen that it increases the growth rates almost twice [33]. Qualitatively it explains why the accelerated stage is observed. The randomly initialized PIC is likely to start from this accelerated stage, this is, the electron trapping patterns are typically observed in very early stages of the PIC simulations (with random start), Figs. 6.6b. Also note that these patterns are developing on the mode number $k \approx 44$, the most unstable mode predicted by the linear theory.

Additionally I have performed two standard PIC simulations (with random start) using a very large number of particles per cell (one million and ten millions). For these simulations one-dimensional EDIPIC code was used [36]. As it was exposed and well known, the standard PIC method leads to a high particle noise (noise decreases slowly as the particles per cell increase). Fig. 6.7b shows an excellent agreement of the growth rate for the wavenumber $k = 44$ (from simulation) with theory. Recalling the theoretical value: $\gamma_{44} = 1.17 \times 10^8$, and the experimental value for 10 000 000 particles per cell is $\gamma_{44} = 1.158 \times 10^8$ with the relative error: 1%. In Fig. 6.7a one can see that using 1 000 000 particles per cell, the relative error is much higher and corresponds to: 42%. We see that randomly initialized simulation for this case requires enormous number of particles to achieve a good agreement with the linear theory, which is impractical, especially considering higher dimensional simulations.

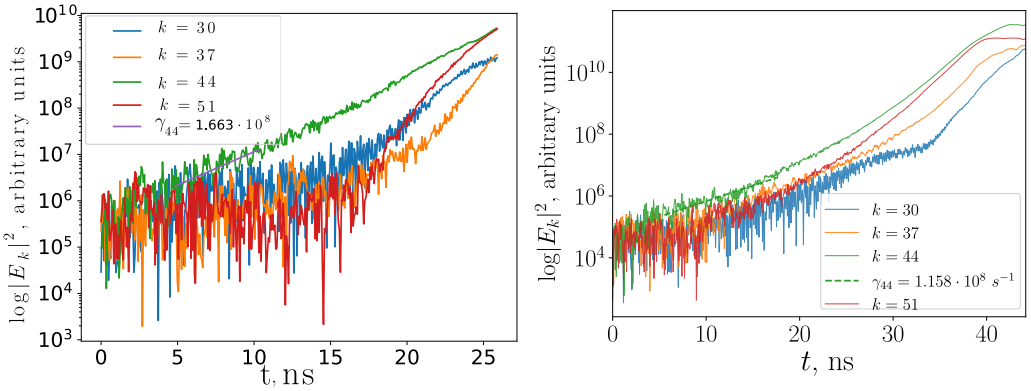

(a) **(b)**

Figure 6.7: PIC simulation with random start using 1 000 000 particles per cell (a) and 10 000 000 particles per cell (b).

6.4 Noise in PIC (random vs quiet loading)

Statistical PIC noise can be interpreted as the artificial collision frequency between particles given by [37]:

$$\nu = \frac{16\omega_{pe}}{N_{de}}, \tag{6.4}$$

where ω_{pe} is the electron plasma frequency, N_{de} is a number of particles in the Debye "cell". It is suggested [38] that this number has to be sufficiently small ($\nu/\omega_{pe} < 10^{-4}$) to keep the collision effect negligible. In our PIC simulations, for the smallest number of particles used (10 000 per grid cell), it estimates as $\nu/\omega_{pe} = 5.5 \times 10^{-6}$. Although this number is sufficiently small (as our simulated plasma is effectively collisionless), the weak instability regime (low drift velocity) was not well reproduced, which might be due to the noise present in the EVDF. It was evident that the quiet loading in PIC generates a lower noise. Here I will show a quantitative difference in the level of noise achieved with quiet and random loading. The idea is to use the initial electrostatic energy (ES) to evaluate the noise level. The ES should be evaluated after a few simulation time starts and thus produced solely by the given initial loading. The electrostatic field energy density U can be calculated as:

$$U = \frac{1}{2}\epsilon_0 \int_L E^2 \, \mathrm{d}x, \tag{6.5}$$

where ϵ_0 is the permittivity of free space. While it is a quadratic quantity, for the noise level we take the square root of the ES value. The comparison between randomly and quietly initiated PIC noise levels is presented in Fig. 6.8. Note that the noise level for randomly initialized particles scales as $1/\sqrt{N}$ as expected. For the quiet start we can see $1/N$ scale which is much faster. It is seen that using quiet start one can achieve the same level of noise using much fewer particles.

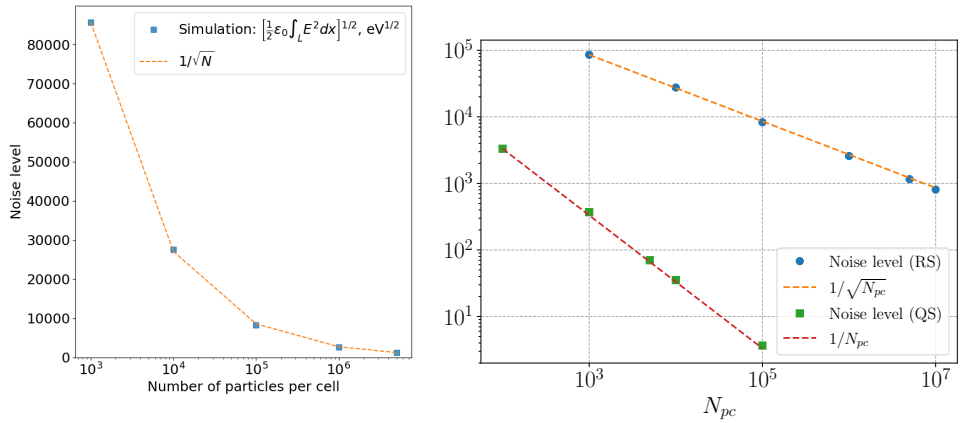

Figure 6.8: Noise level as a function of total number of macro-particles per cell for a random start (on the left). Comparison of noise level for a quiet (QS) and a random start (RM) (on the right).

6.5 Summary

It is shown in this Chapter, that utilizing the particle-in-cell method (standard plasma kinetic simulations tool) without any special methods, may arise noise levels large enough to impede the Buneman instability be consistent with the linear theory. Trapping effects in the EVDF were observed from the very start of a simulation, suggesting that the growth was not linear but corresponds to the accelerated stage. This was demonstrated in the example of the weak Buneman instability. To resolve the issue, we only exploited a quiet start technique here, but there are other methods for noise reduction in PIC codes (e.g., delta-f [39]). We have analyzed the role of noise in PIC simulations, and it is identified that using the PIC (random start), a huge number of macroparticles per cell will be needed (10^7) in order to agree with the growth rate theoretical value, for the case of the Buneman instability.

7 Conclusions

The PIC method is extensively used in plasma physics to solve the Vlasov-Maxwell system of equations. This allows modeling many realistic plasma configurations and thus predict important physical phenomenons. The 2D3V PIC code has been tested in various configurations. Different parts of the code were tested using a single charged particle, such as particle integrator and Poisson's equation solver separately. Furthermore, the code was tested with comprehensive 2D3V plasma simulations of the Electron Cyclotron Drift Instability. I performed more than thirty plasma simulations for a Hall thruster configuration to complete this work. The simulation results reveal linear and nonlinear dynamics of plasma and it agrees with the analytical dispersion equation for the linear instability regime. This is, unstable modes predicted by the solutions of full kinetic dispersion equation for linear waves, are picked up in the simulation and comparing the growth rates well-agreed with the prediction in linear theory, for example see Fig. 2.6.

A few insights are described due to the parametric study: The anomalous electron current is identified as a result of nonlinear development of the ECDI instability. It is shown that the magnitude of the anomalous current can be explained as the $\mathrm{E} \times \mathrm{B}$ drift of magnetized electrons in fluctuating fields. Observed values of the anomalous current may be explained as the current due to $\mathrm{E}_\theta \times \mathrm{B}$ drift, where E_θ are fluctuations of the electric field in azimuthal direction, given the resulting anomalous current $J_z = q_e \langle n \mathrm{E}_\theta \rangle_{x,y} / \mathrm{B}$. Magnitude of the magnetic field is determinant for the values of the anomalous current. Inverse cascade is observed for the anomalous current. Anomalous electron current evolves into the long-wavelength region.

Additionally to the azimuthal-radial simulations in Chapter 4, my participation in the LANDMARK project was presented. Seven different groups used an independent PIC code for the verification and authenticity of each azimuthal-radial simulation. All comprehensive tests showed a very good agreement between the groups and what linear theory predicts. This project validated my results from previous Chapter 4.

Finally, together with these 2D simulations, I have performed and discussed various 1D simulations in order to study the effect of noise in kinetic simulations for the Buneman instability. Although a random start initialization was utilized in the radial-azimuthal simulations of the Hall thruster (Chapter 4,5), the problem of noise was not discussed there. However, the convergence with the number of macroparticles per cell was achieved in the simulations. Also, the agreement with the linear theory was achieved, even where the growth rate measurements were off by 10-20% in few cases, suggesting that the noise possibly played a role in these simulations.

Bibliography

[1] D.R. Nicholson. Introduction to plasma theory. Wiley New York, 1983.

[2] J.A. Binttencourt. Fundamentals of Plasma physics. JA Bittencourt, 2004.

[3] S. Tsikata and T. Minea. Modulated electron cyclotron drift instability in a high-power pulsed magnetron discharge. Phys. Rev. Lett., 114:185001, May 2015.

[4] D. Liu. Two-Dimensional Time-Dependent Plasma Structures of a Hall Effect Thurster. PhD thesis, Air Force Institute of Technology, 2011.

[5] F. Cap. Handbook on Plasma Instabilities. Academic Press, 1976.

[6] D.T. Farley. Two-stream plasma instability as a source of irregularities in the ionosphere. Phys. Rev. Lett., 10:279–282, Apr 1963.

[7] J.B. McBride, E. Ott, J.P. Boris, and J.H. Orens. Theory and simulation of turbulent heating by the modified two-stream instability. The Physics of Fluids, 15(12):2367–2383, 1972.

[8] P. Helander and D.J. Sigmar. Collisional Transport in Magnetized plasmas. Cambridge University Press, 2005.

[9] R.J. Goldston and P.H. Rutherford. Introduction to Plasma Physics. Iop Institute of Physics, 1995.

[10] J. D. Anderson and J. Wendt. Computational fluid dynamics, volume 206. Springer, 1995.

[11] I. B. Bernstein. Waves in a plasma in a magnetic field. Physical Review, 109(1):10, 1958.

[12] S. Janhunen, A.I. Smolyakov, D. Sydorenko, M. Jimenez, I. Kaganovich, and Y. Raitses. Evolution of the electron cyclotron drift instability in two-dimensions. Physics of Plasmas, 25(8):082308, 2018.

[13] O. Buneman. Instability of electrons drifting through ions across a magnetic field. Journal of Nuclear Energy. Part C, Plasma Physics, Accelerators, Thermonuclear Research, 4(2):111–117, 1962.

[14] J. Cavalier, N. Lemoine, G. Bonhomme, S. Tsikata, C. Honoré, and D. Grésillon. Hall thruster plasma fluctuations identified as the ExB electron drift instability: Modeling and fitting on experimental data. Physics of Plasmas, 20(8):082107, 2013.

[15] C.K. Birdsall and A.B. Langdon. Plasma physics via computer simulation. CRC press, 2004.

[16] J.P. Boris and R.A. Shanny. Proceedings: Fourth Conference on Numerical Simulation of Plasmas, November 2, 3, 1970. Naval Research Laboratory, 1972.

[17] W.H. Press, S.A. Teukolsky, and B.P. Flannery. Numerical Recipies in Fortran 77. ISBN 0-521-43064-X, 1992.

[18] D. Young. Iterative methods for solving partial difference equations of elliptic type. Transactions of the American Mathematical Society, 76(1):92–111, 1954.

[19] R. Haberman. Applied partial differential equations with Fourier series and boundary value problems. Pearson Higher Ed, 2012.

[20] P. Pacheco. An introduction to parallel programming. Elsevier, 2011.

[21] D. Sydorenko. Particle-in-cell simulations of electron dynamics in low pressure discharges with magnetic fields. PhD thesis, University of Saskatchewan, 2006.

[22] V. P. Kumar and A. Gupta. Analyzing scalability of parallel algorithms and architectures. Journal of parallel and distributed computing, 22(3):379–391, 1994.

[23] A. Ducrocq, J.C. Adam, A. Héron, and G. Laval. High-frequency electron drift instability in the cross-field configuration of Hall thrusters. Physics of Plasmas, 13(10):102111, 2006.

[24] T. Lafleur, S.D. Baalrud, and P. Chabert. Theory for the anomalous electron transport in Hall effect thrusters. i. Insights from particle-in-cell simulations. Physics of Plasmas, 23(5):053502, 2016.

[25] S. Janhunen, A.I. Smolyakov, O. Chapurin, D. Sydorenko, I. Kaganovich, and Y. Raitses. Nonlinear structures and anomalous transport in partially magnetized plasmas. Physics of Plasmas, 25(1):011608, 2018.

[26] J.C. Adam, A. Héron, and G. Laval. Study of stationary plasma thrusters using two-dimensional fully kinetic simulations. Physics of Plasmas, 11(1):295–305, 2004.

[27] P. Coche and L. Garrigues. A two-dimensional (azimuthal-axial) particle-in-cell model of a Hall thruster. Physics of Plasmas, 21(2):023503, 2014.

[28] V. Croes, T. Lafleur, Z. Bonaventura, A. Bourdon, and P. Chabert. 2D particle-in-cell simulations of the electron drift instability and associated anomalous electron transport in Hall-effect thrusters. Plasma Sources Science and Technology, 26(3):034001, 2017.

[29] A. Héron and J.C. Adam. Anomalous conductivity in Hall thrusters: Effects of the non-linear coupling of the electron-cyclotron drift instability with secondary electron emission of the walls. Physics of Plasmas, 20(8):082313, 2013.

[30] E. Jones, T. Oliphant, P. Peterson, et al. SciPy: Open source scientific tools for Python, 2001–.

[31] A.I. Smolyakov, W. Frias, I.D. Kaganovich, and Y. Raitses. Sheath-induced instabilities in plasmas with E × B drift. Physical review letters, 111(11):115002, 2013.

[32] W. Villafana, F. Petronio, A.C. Denig, M. Jimenez, D. Eremin, L. Garrigues, F. Taccogna, A. Laguna, J. Boeuf, A. Bourdon, P. Chabert, T. Charoy, B. Cuenot, K. Hara, F. Pechereau, A.I. Smolyakov, D. Sydorenko, A. Tavant, and O. Vermorel. 2D radial-azimuthal particle-in-cell benchmark for E×B discharges. Plasma Sources Science and Technology, 30(7):075002, jul 2021.

[33] A. Tavassoli, O. Chapurin, M. Jimenez Jimenez, T. Zintel, M. Papahn Zadeh, M. Shoucri, R. Spiteri, L. Couedel, and A. Smolyakov. The role of noise in PIC and Vlasov simulations of the Buneman instability. 2021. In preparation.

[34] O. Buneman. Instability, turbulence, and conductivity in current-carrying plasma. Phys. Rev. Lett., 1:119–119, Aug 1958.

[35] D.B. Melrose. Instabilities in space and laboratory plasmas. 1986.

[36] D. Sydorenko. EDIPIC. `https://github.com/PrincetonUniversity/EDIPIC`.

[37] H. Okuda and C.K. Birdsall. Collisions in a plasma of finite-size particles. The Physics of Fluids, 13(8):2123–2134, 1970.

[38] M. M. Turner. Kinetic properties of particle-in-cell simulations compromised by monte carlo collisions. Physics of Plasmas, 13(3):033506, 2006.

[39] S. E. Parker and W. W. Lee. A fully nonlinear characteristic method for gyrokinetic simulation. Physics of Fluids B: Plasma Physics, 5(1):77–86, 1993.

A Code structure

The 2D3V code written by Dmytro Sydorenko has been improved for this thesis work, adding new features. Specifically, a virtual axial axis was added in order to mimic the plasma dynamics in axial direction of a real Hall thruster. I added the reflecting boundary condition option and used it for the case REF-1 (described in Chapter 4). Also, the particle source shape function was modified to match the setup in the LANDMARK project (details are given in Chapter 5).

Here, I will comment on some of the input data files, output data files, and some parameters to give an overview for the 2D3V code structure.

Input data files

The user has the following input files to specify the desired parameters:

1. **init-configuration.dat**: The parameters in this file will define the electron time step, the spatial resolution, dimensions of the grid, type of boundary conditions and number of processes. Part of the input data file is provided:

```
---dddd.ddd----- scale electron temperature [eV]
---+d.dddE+dd--- scale electron density [m^3]
---ddd---------- number of cells per scale electron Debye length
---ddd---------- maximal expected velocity [units of scale thermal electron velocity]
---ddd---------- number of blocks (processes) along the X (horizontal) direction
---ddd---------- number of blocks (processes) along the Y (vertical) direction
---ddd---------- number of cells along the X-direction in a block
---ddd---------- number of cells along the Y-direction in a block
--dddd---------- number of macroparticles per cell for the scale density
-----d---------- number of blocks in a cluster along the X-direction
-----d---------- number of blocks in a cluster along the Y-direction
---ddd---------- number of boundary objects
```

For each wall, user must specify its boundary condition type, the potential, and the relative permittivity of the wall. Users have 5 different options for boundary conditions:

⋆ 4 metal electrodes

⋆ 2 metal electrodes at Y-boundaries and 2 periodic pipelines at X-boundaries

⋆ 2 infinitely stick dielectric wall at Y and 2 periodic pipelines at X-boundaries.

⋆ 2 metal electrode at lower Y-boundary, infinitely-dielectric at upper Y-boundary and 2 periodic pipelines at X-boundaries

⋆ 2 periodic pipeline at Y- and 2 periodic pipelines at X-boundaries

Note that in these simulations I used the second and third option, this is metal or dielectric walls along the magnetic field (Y-boundaries) and periodic along the azimuthal direction (X-boundaries).

2. **init-externalfields.dat**: Contains the applied magnetic and electric field values in the configuration.

3. **init-particles.dat**: Contains the initial electron and ion temperature in eV and the initial particle density.

4. **init-setup.dat**: This file is specially for axial-azimuthal simulation in a Hall thruster configuration. Therefore, parameters such as temperature of electron emission from the cathode, anode and cathode position, and number density of the neutral plasma flowing out through the cathode, are some of the required parameters for an axial-azimuthal simulation.

5. **init-simcontrol.dat**: Contains the simulation time parameter and the use of checkpoints to continue the simulation as required.

6. **init-snapshots.dat**: Contains configuration for output data in the form of macroscopic plasma fields (as a function of space), such as density, flow velocity, temperature, etc.

7. **init-probes.dat**

Output data files

→ **Service data files**

→ **Local temporal dependencies**

→ **Spatial profile snapshots**: Here one can find the available macroscopic output variable values, each variable with spatial depending (x, y), two-dimensional arrays. They are:

Table A.1: Variables values output, for plasma and fields

Electric field, E_x, E_y	V/cm
Current density, J_x, J_x, J_z	A/m^2
Electrostatic potential, F	V
Distribution function in file, vdf1d	1D

Table A.2: Variables values output, for ions & electrons

Particle coordinates (x, y)	m
Particle density, n	m^{-3}
Particle temperature, T_x, T_y, T_z	eV
Particle energy, w_x, w_y, w_z	eV
Current density, J_x, J_x, J_z	A/m^2
Particle velocities, v_x, v_y, v_z	m/s

The code output contains three distribution functions: f_x, f_y and f_z, every distribution function is averaged in velocity space, leaving one dimensional dependence in velocity space. Thus, every macroscopic variable is found by taking the moments of the distribution function.

B Plasma Dispersion Function

The plasma dispersion function: Where $\zeta = \omega/kv_T$. If we differentiate $Z(\zeta)$ with respect to ζ we obtain:

$$Z'(\zeta) = -\pi^{-1/2} \int_{-\infty}^{\infty} \frac{2te^{-t^2}}{t-\zeta} dt = -2\left[1 + \zeta Z\right]. \tag{B.1}$$

Two limiting cases of the plasma dispersion function are adiabatic $\zeta \ll 1$ and fluid limit $\zeta \gg 1$. For adiabatic limit:

$$Z(\zeta) = i\pi^{1/2} e^{-\zeta^2} - 2\zeta \left[1 - \frac{2\zeta^2}{3} + \frac{4\zeta^4}{15} - \frac{8\zeta^6}{105} + ..\right]. \tag{B.2}$$

For fluid limit:

$$Z(\zeta) = i\pi^{1/2}\sigma^{-\zeta^2} - \zeta^{-1}\left[1 + \frac{1}{2\zeta^2} + \frac{3}{4\zeta^4} + \frac{15}{8\zeta^6} + ..\right], \tag{B.3}$$

where $\sigma = 0,\ \mathrm{Im}\zeta > 0,\ \sigma = 1,\ \mathrm{Im}\zeta = 0$, and $\sigma = 2,\ \mathrm{Im}\zeta < 0$.

Using relation (B.1), it is easy to obtain the series representation for $\mathrm{Z}^{'}$. In the adiabatic limit:

$$\mathrm{Z}^{'}(\zeta) = -2 - i\pi^{1/2}\zeta e^{-\zeta^2} + 4\zeta^2 - \frac{8}{3}\zeta^4 + ... \tag{B.4}$$

In the fluid limit:

$$\mathrm{Z}^{'}(\zeta) = -2\zeta i\pi^{1/2}\sigma^{-\zeta^2} + \frac{1}{\zeta^2} + \frac{3}{2\zeta^4} + ... \tag{B.5}$$

C Azimuthal-radial simulations with dielectric walls, $\epsilon = 2$

C.0.1 **DRUN-D22** B $= B_0/2 = 100$ G

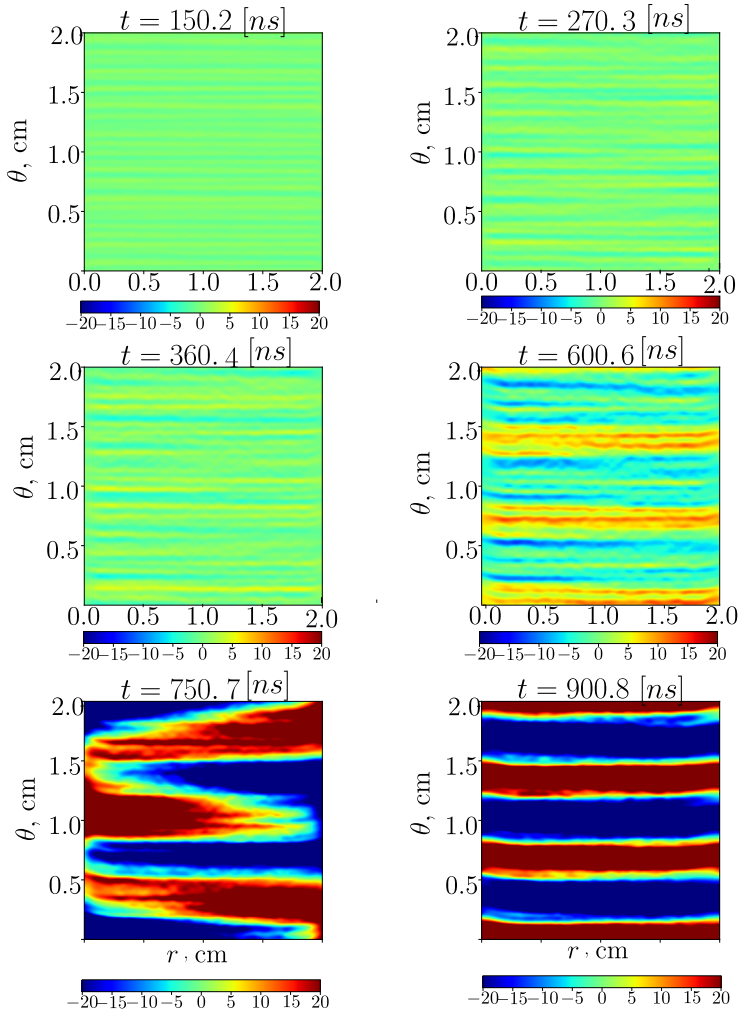

Figure C.1: Nonlinear evolution of electric potential fluctuations $\widetilde{\phi}$ in time; B = 100 G.

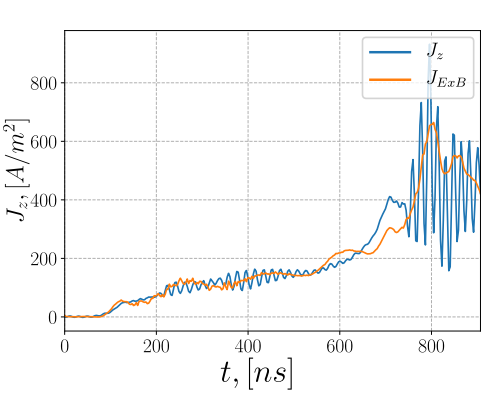

(a) Evolution of J_z and the current due to $\mathbf{E} \times \mathbf{B}$ drift.

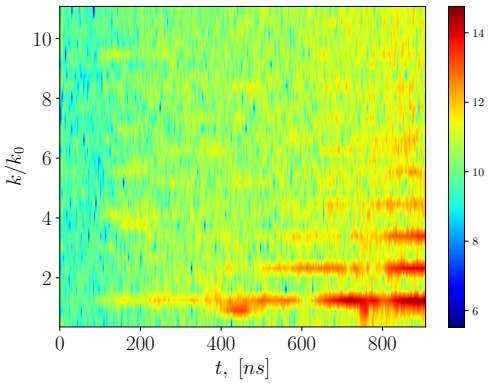

(b) Anomalous current k-spectra over time.

Figure C.2: Evolution of J_z and due to $\mathbf{E} \times \mathbf{B}$ drift; B = 100 G.

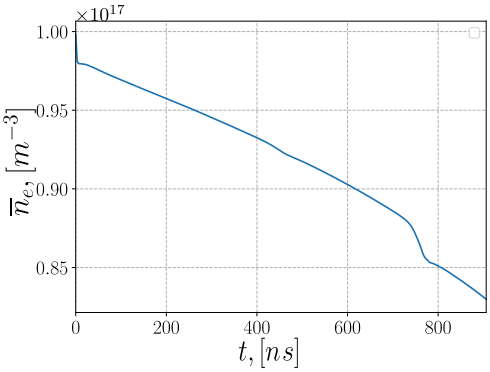

(a) Evolution of of the averaged (in space) electron density $\overline{n}_e$.

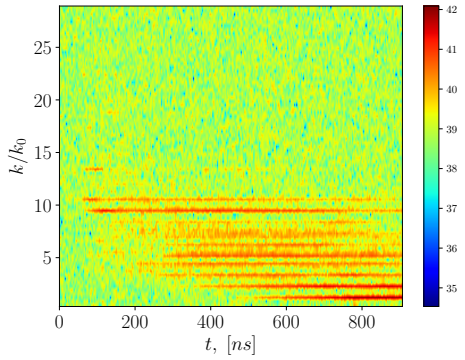

(b) Perturbed density fluctuations over simulation time.

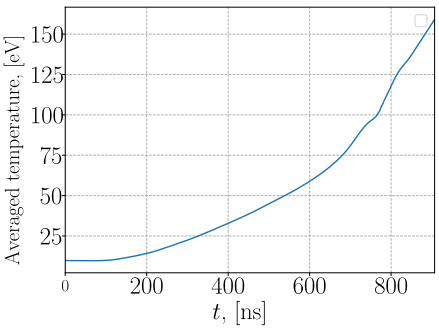

(c) Electron temperature over time.

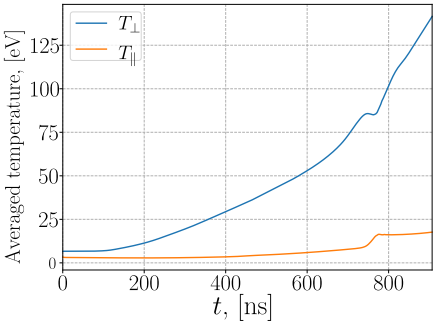

(d) Electron temperature components.

Figure C.3: Evolution of electron density and electron temperature; B = 100 G.

C.0.2 **DRUN-D23** B = 2 $B_0 = 400$ G

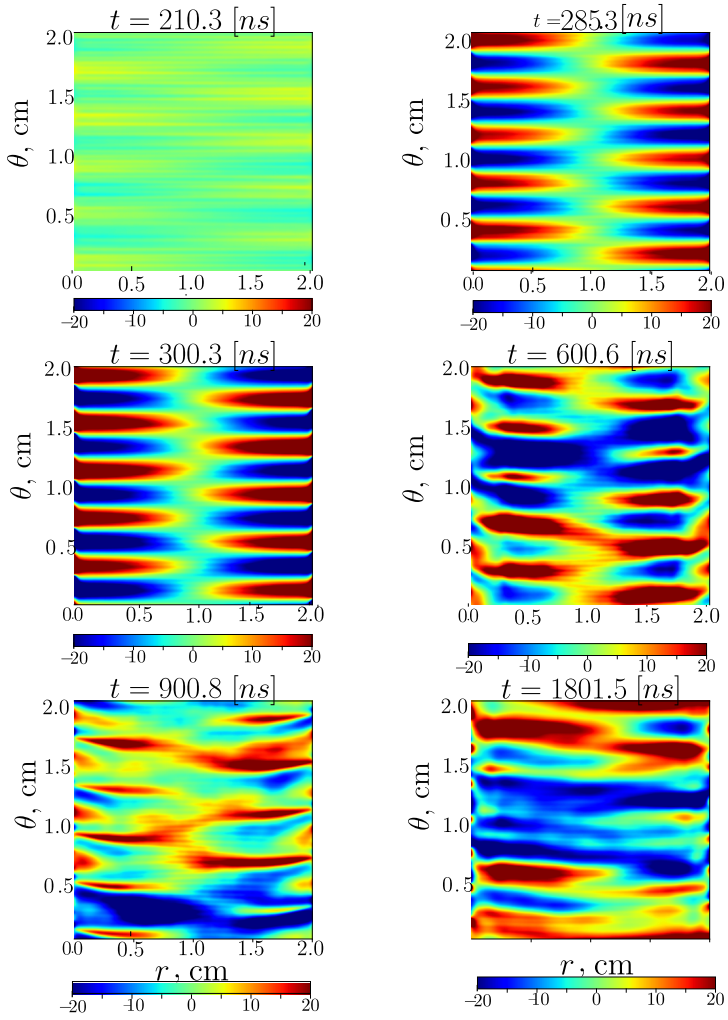

Figure C.4: Nonlinear evolution of electric potential fluctuations $\widetilde{\phi}$ in time; B = 400 G.

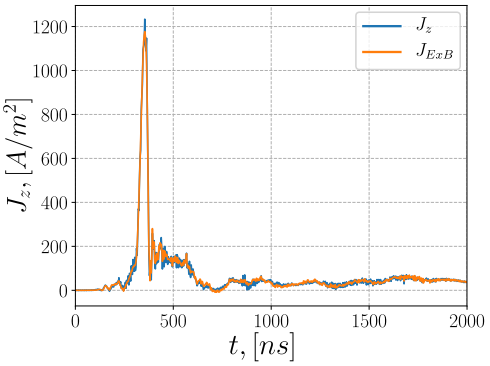

(a) Evolution of J_z and the current due to $\mathbf{E} \times \mathbf{B}$ drift.

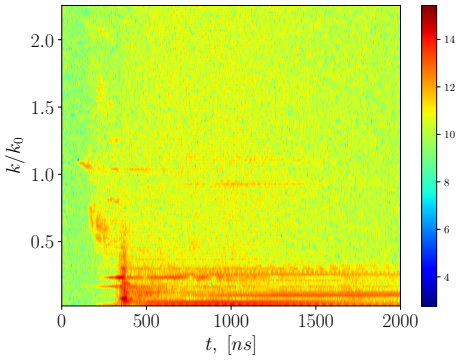

(b) Anomalous current k-spectra over time.

Figure C.5: Evolution of J_z and due to $\mathbf{E} \times \mathbf{B}$ drift; B = 400 G.

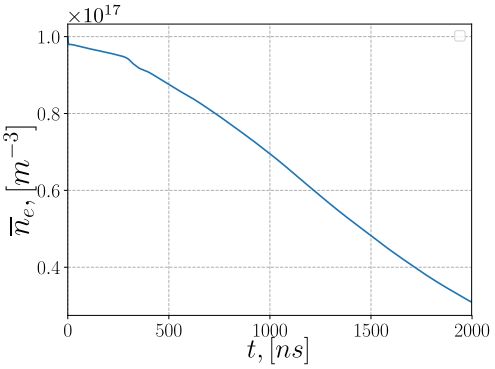

(a) Evolution of the averaged (in space) electron density $\overline{n}_e$.

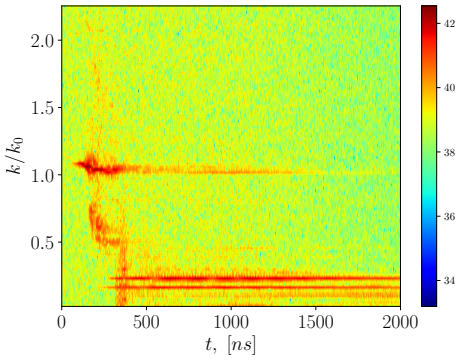

(b) Perturbed density fluctuations over simulation time.

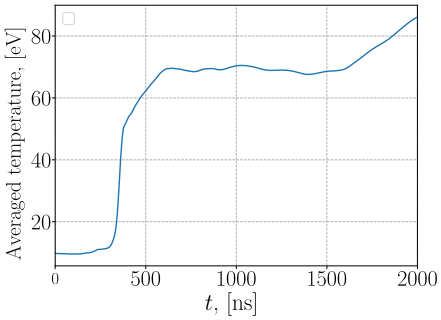

(c) Electron temperature over time.

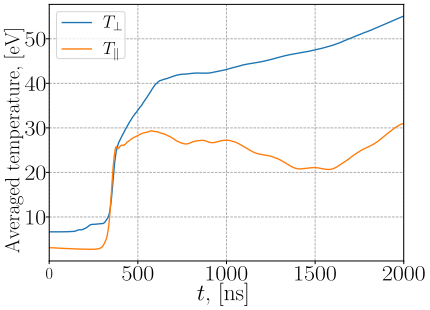

(d) Temperature components time.

Figure C.6: Evolution of the electron density and the electron temperature; B = 400 G.

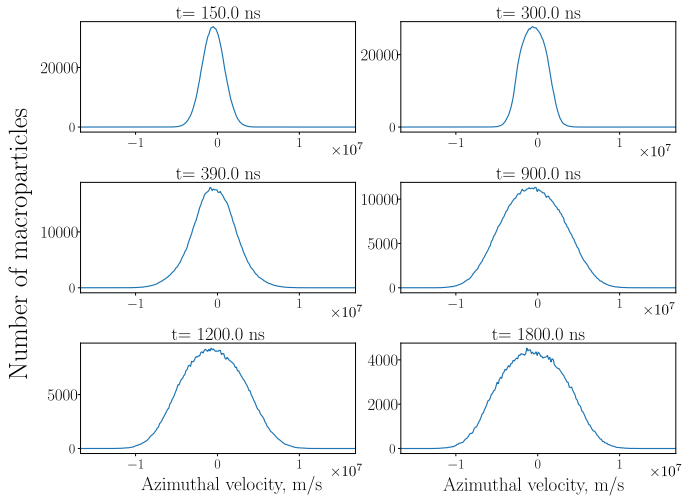

Figure C.7: Evolution of the electron velocity distribution function in azimuthal-direction; $x, y = 1$ cm, 1 cm.

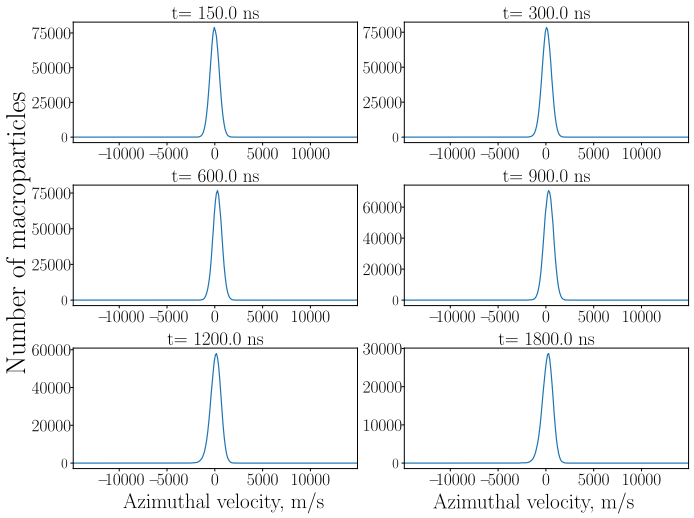

Figure C.8: Evolution of the ion velocity distribution function for $x, y = 1$ cm, 1 cm.

C.0.3 DRUN-C20 E = $E_0/2 = 100$ V/cm

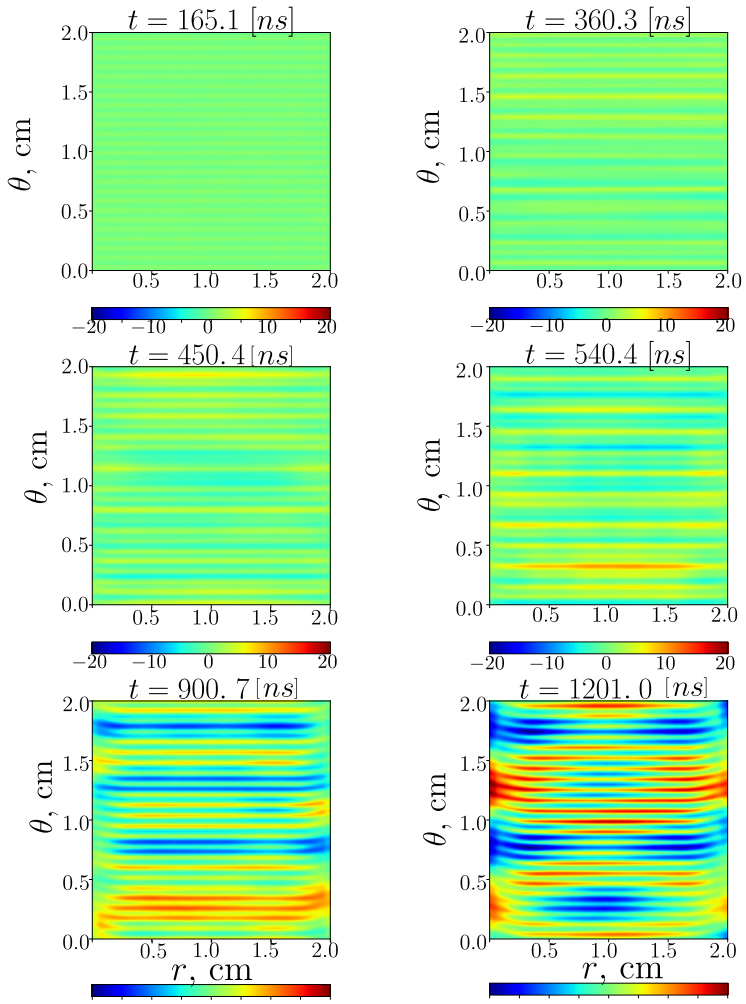

Figure C.9: Nonlinear evolution of electric potential fluctuations $\widetilde{\phi}$ in time; E = 100 V/cm.

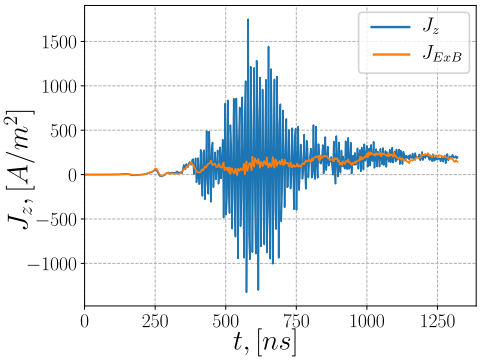

(a) Evolution of J_z and the current due to $\mathbf{E} \times \mathbf{B}$ drift.

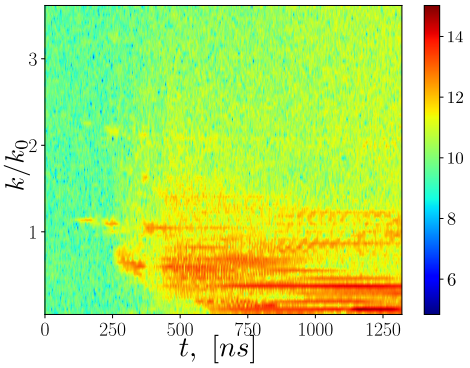

(b) Anomalous current k-spectra over time.

Figure C.10: Evolution of J_z and due to $\mathbf{E} \times \mathbf{B}$ drift; E = 100 V/cm.

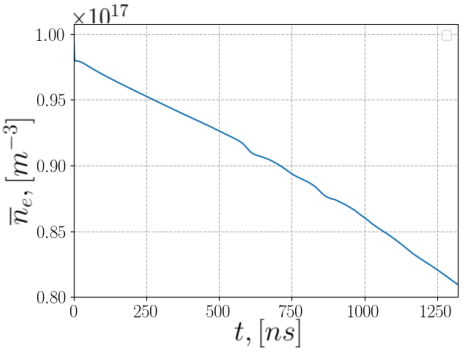

(a) Evolution of the averaged (in space) electron density $\overline{n}_e$.

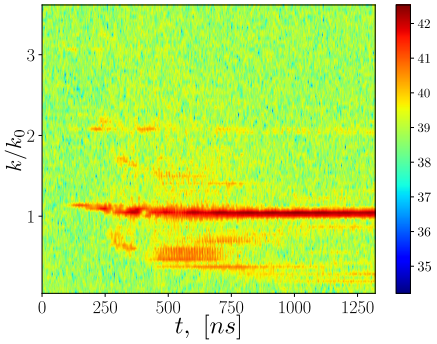

(b) Perturbed density fluctuations over simulation time.

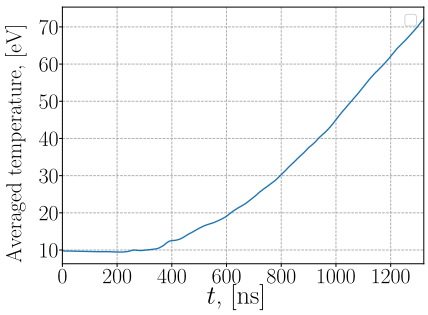

(c) Electron temperature over time.

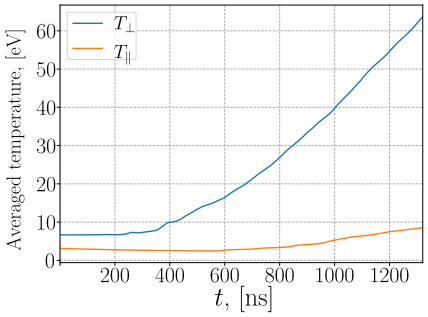

(d) Electron temperature components.

Figure C.11: Evolution of the electron density and the electron temperature; E = 100.

C.0.4 DRUN-C21 E = 2 E_0 = 400 V/cm

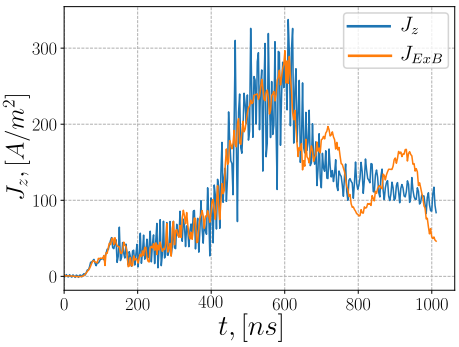

(a) Evolution of J_z and the current due to $\mathbf{E} \times \mathbf{B}$ drift.

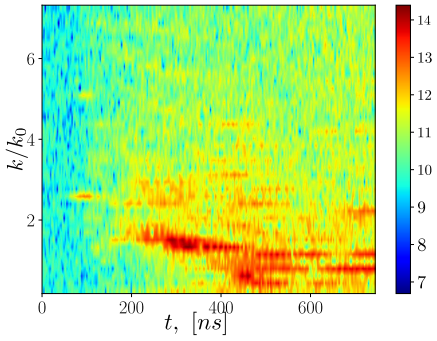

(b) Anomalous current k-spectra over time.

Figure C.12: Evolution of J_z and due to $\mathbf{E} \times \mathbf{B}$ drift; E = 400 V/cm.

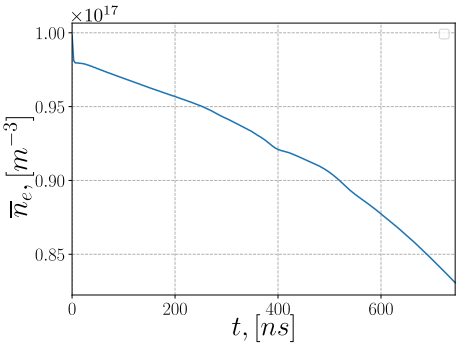

(a) Evolution of the averaged (in space) electron density $\overline{n}_e$.

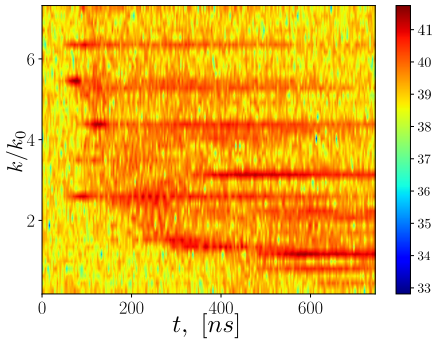

(b) Perturbed electron density fluctuations over simulation time.

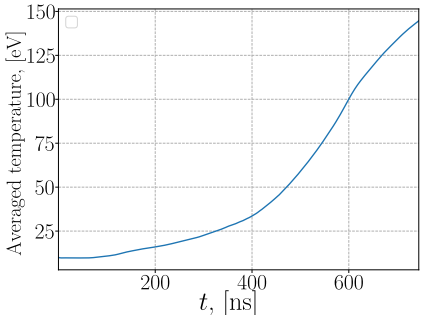

(c) Electron temperature over time.

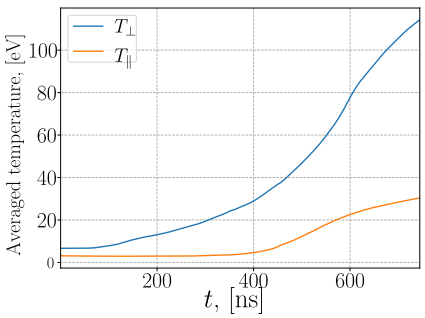

(d) Electron temperature components

Figure C.13: Evolution of electron density and electron temperature; E = 400 V/cm.

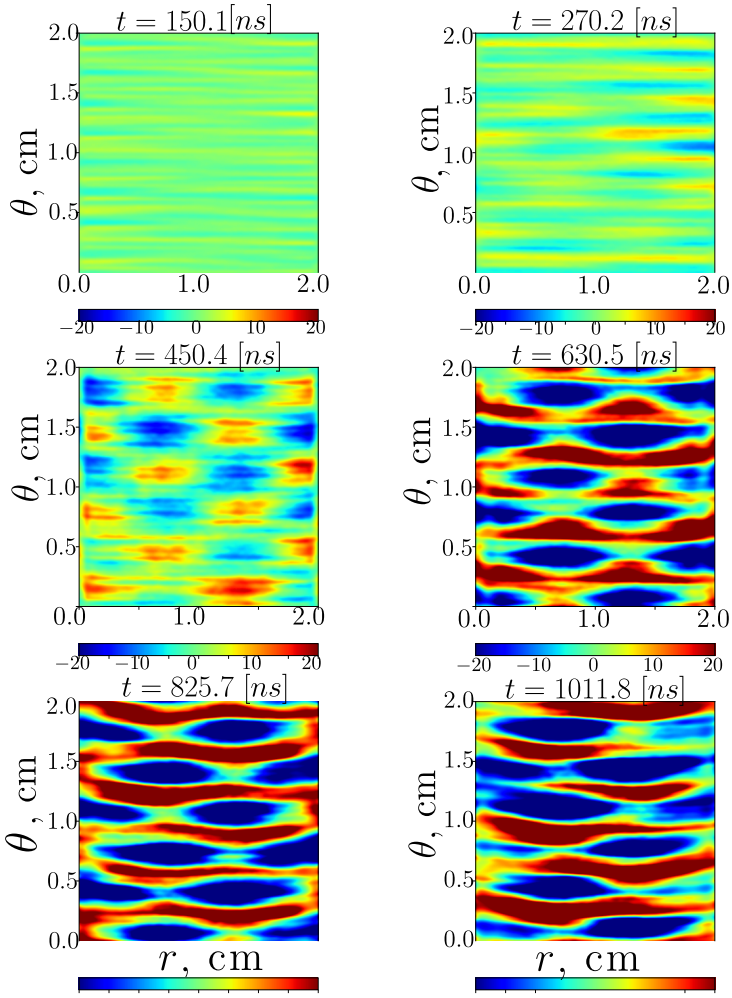

Figure C.14: Nonlinear evolution of electric potential fluctuations $\widetilde{\phi}$ in time; E = 400 V/cm.

C.0.5 DRUN-B18 $\mathrm{N} = N_0/2 = 5 \times 10^{16}\,\mathrm{m}^{-3}$

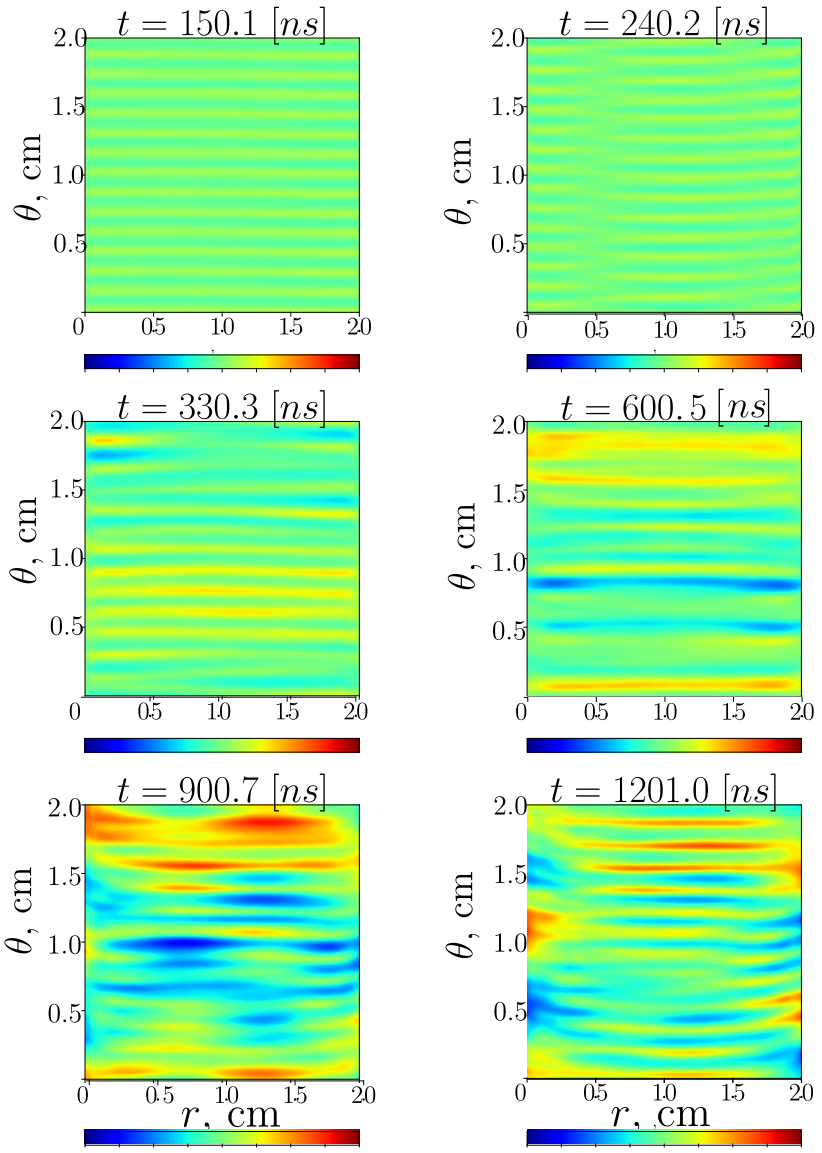

Figure C.15: Nonlinear evolution of electric potential fluctuations $\widetilde{\phi}$; Density $\mathrm{N} = 5 \times 10^{16}\,\mathrm{m}^{-3}$.

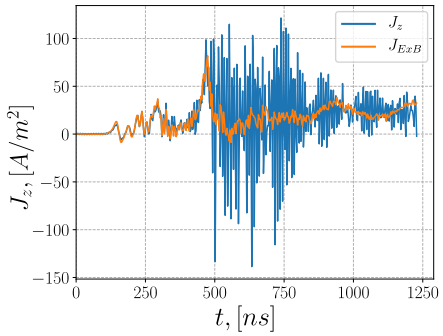

(a) Evolution of J_z and the current due to $\mathbf{E} \times \mathbf{B}$ drift.

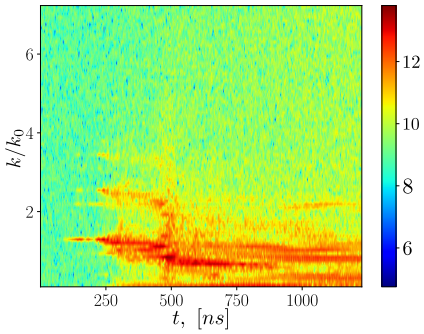

(b) Anomalous current k-spectra over time.

Figure C.16: Evolution of J_z and due to $\mathbf{E} \times \mathbf{B}$ drift; N = $5 \times 10^{16}\,\mathrm{m}^{-3}$.

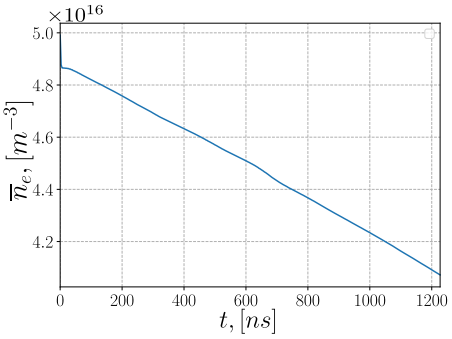

(a) Evolution of the averaged (in space) electron density $\overline{n}_e$.

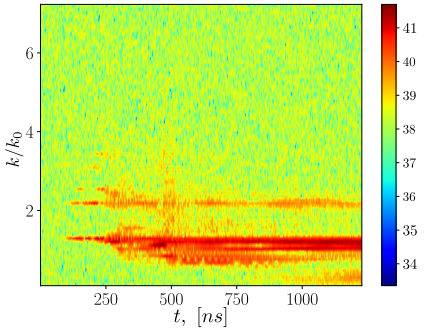

(b) Perturbed electron density fluctuations over simulation time.

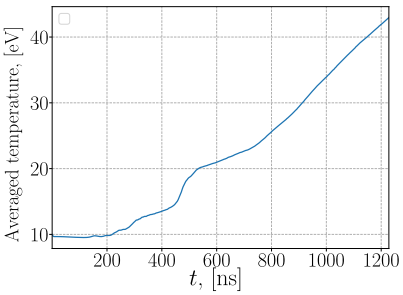

(c) Electron temperature over time.

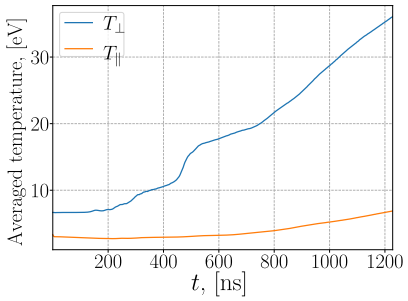

(d) Electron temperature components.

Figure C.17: Evolution of the electron density and the electron temperature; Density N = $5 \times 10^{16}\,\mathrm{m}^{-3}$.

C.0.6 DRUN-B19 N = 2 $N_0 = 2 \times 10^{17}\,\mathrm{m}^{-3}$

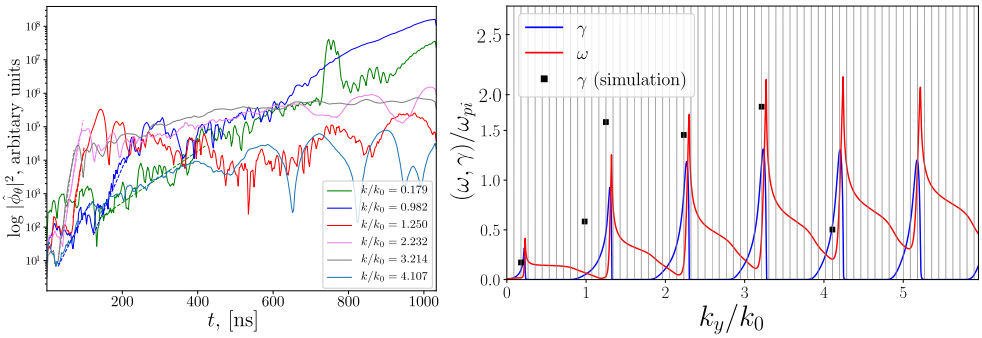

(a) Logarithmic amplitude of the azimuthal electric potential energy $\phi_\theta|^2$.

(b) Growth rate and frequencies for $k_z\lambda_{De} = 0.008$.

Figure C.18: Linear growth and nonlinear saturation of the cyclotron and (MTSI) modes.

The growth rates for the first four cyclotron modes are: $\gamma 1 = 1.584 \gamma 2 = 1.454, \gamma 3 = 1.738, \gamma 4 = 0.503$. The MTSI mode with a $\gamma 0 = 0.172$.

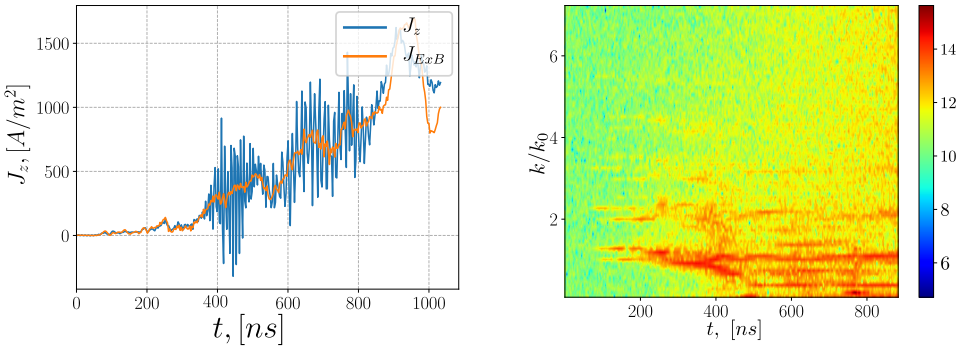

(a) Evolution of J_z and the current due to $\mathbf{E} \times \mathbf{B}$ drift.

(b) Anomalous current k-spectra over time.

Figure C.19: Evolution of J_z and due to $\mathbf{E} \times \mathbf{B}$ drift. Density N = $2 \times 10^{17}\,\mathrm{m}^{-3}$.

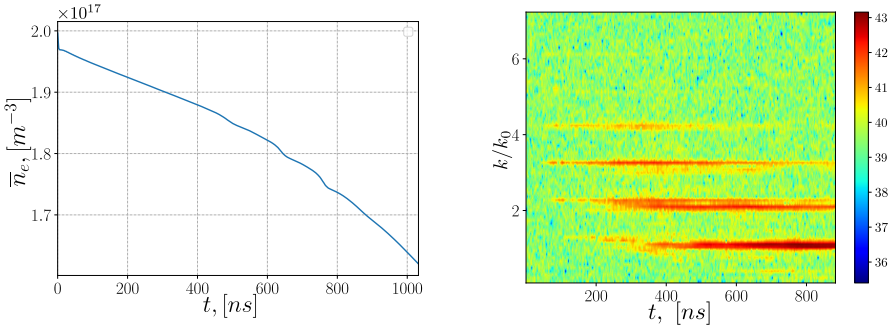

(a) Evolution of the averaged (in space) electron density $\overline{n}_e$.

(b) Perturbed electron density fluctuations over simulation time.

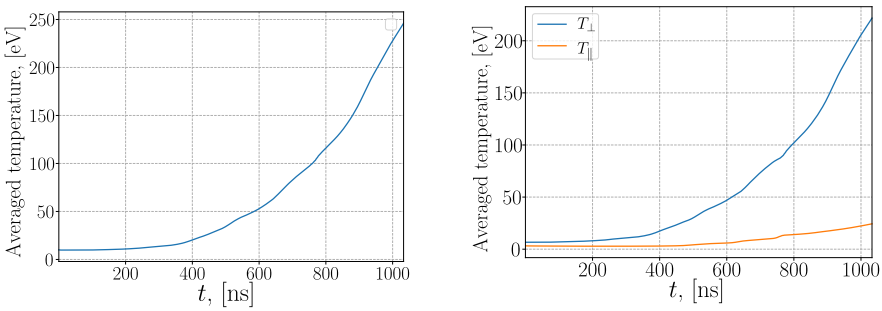

(c) Electron temperature over time.

(d) Temperature components time.

Figure C.20: Evolution of the electron density and the electron temperature. Density N = $2 \times 10^{17}\,\mathrm{m}^{-3}$.

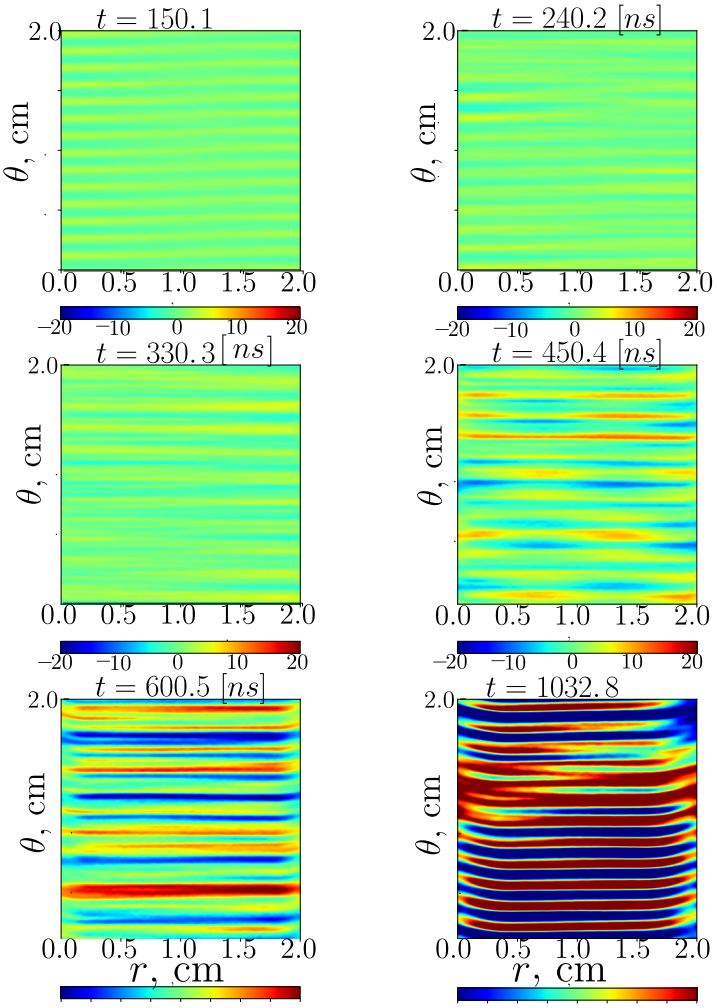

Figure C.21: Nonlinear evolution of electric potential fluctuations $\widetilde{\phi}$. Density N = $2 \times 10^{17}\,\mathrm{m}^{-3}$.

C.0.7 DRUN-A17, azimuthal length, $L_\theta = 2$ cm, radial length, $L_r = 2$ $L_{r1} = 4$ cm, $\varepsilon = 4$

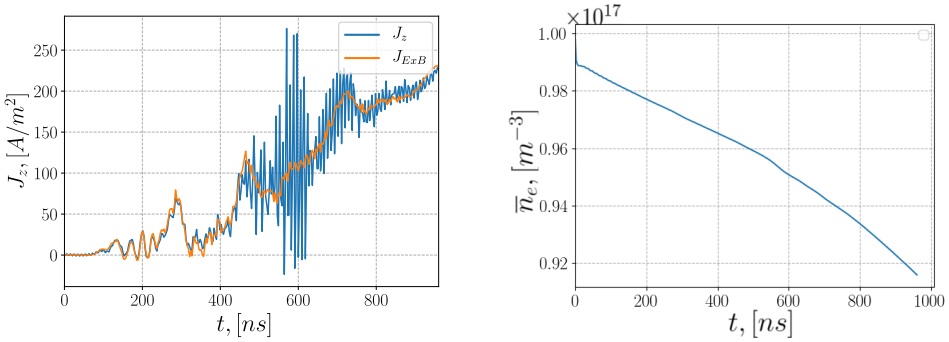

(a) Evolution of mean anomalous current density J_z and the current due to $\mathbf{E} \times \mathbf{B}$ drift.

(b) Evolution of averaged electron density $\overline{n}_e$ over simulation time.

Figure C.22: Evolution of mean anomalous current density J_z and the current due to $\mathbf{E} \times \mathbf{B}$ drift.(ε=4).

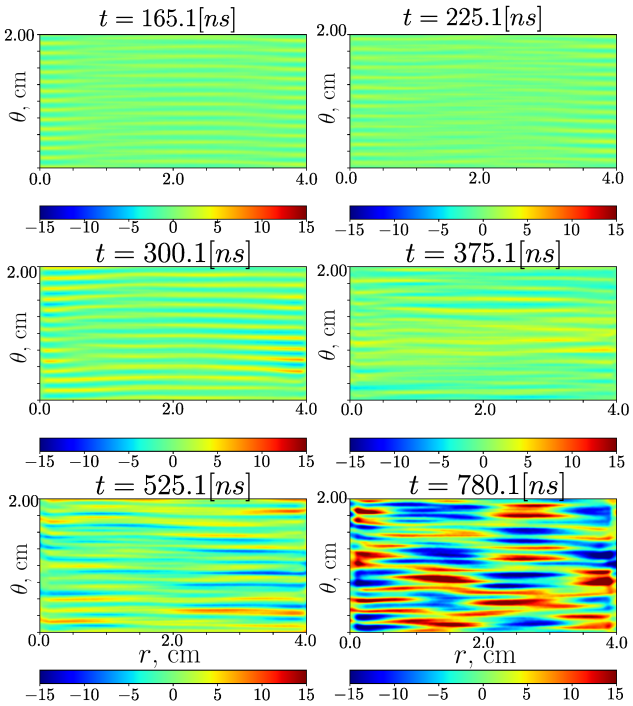

Figure C.23: Nonlinear evolution of electric potential fluctuations $\widetilde{\phi}$ in time. $L_r = 4\,\text{cm}$, $\varepsilon = 4$.

D Wavelength of structures

Values of wave length of large structures and anomalous transport for simulations with metal walls:

MRUN-1.	MRUN-E11.	MRUN-A2.	DRUN-A14.	MRUN-A3.	MRUN-A4.	DRUN- A15.
$\lambda = 0.1428$	1.11×10^{-1}	1.428×10^{-1}	1.728×10^{-1}	1.25×10^{-1}	0.025	1.428×10^{-1}
$\Lambda = 2$ cm	0.33	0.67	2	2	0.5	0.67
J = 250 A/m^2	1000 A/m^2	190, 280 A/m^2	220A/m^2	570 A/m^2	107 A/m^2	230 A/m^2

DRUN-A16.	MRUN-B5.	MRUN-B6.	MRUN-C7.	MRUN- C8.	MRUN-D9.	MRUN-D10.
$\lambda = 0.1428$	1.428×10^{-1}	1.428×10^{-1}	7.142×10^{-2}	2×10^{-1}	7.142×10^{-1}	0.03846
$\Lambda = 0.67$	0.2	0.25	1	0.33, 0.66	0.66	0.29
J = 225	40 A/m^2	1000, 1300 A/m^2	250 A/m^2	280 A/m^2	175 A/m^2	260 A/m^2

Values of wave length of large structures using dielectric walls:

DRUN-13.	DRUN-B17.	DRUN-B18.	DRUN-C19.	DRUN-C20.	DRUN-D21.	DRUN-D22.
1.428×10^{-1}	1.33×10^{-1}	1.428×10^{-1}	7.143×10^{-2}	7.143×10^{-1}	8.33×10^{-1}	4.54×10^{-2}
2	2	2	0.67	0.67	0.67	0.4
200	70,40	1000	240	290	600	1100

Comparison between values from Eq. (D.1) and simulations values:

$$\lambda = 2\pi \frac{E_z m_e}{B_y^2 q_e}. \tag{D.1}$$

Next tables show a comparison using the Eq. (D.1) and the simulation results for the wave length of structures in the linear regime.

MRUN-1.	MRUN-E11.	MRUN-A2.	MRUN-A3.	MRUN-A4.	DRUN-A15.
$\lambda_{form} = 1.786 \times 10^{-1}$	3.57×10^{-1}	1.786×10^{-1}	1.786×10^{-1}	1.786×10^{-1}	1.786×10^{-1}
$\lambda_{sim} = 1.333 \times 10^{-1}$	1.11×10^{-1}	1.428×10^{-1}	1.25×10^{-1}	1.428×10^{-1}	1.428×10^{-1}

DRUN-A16.	MRUN-A5.	MRUN-B6.	MRUN-C7.	MRUN-C8.	MRUN- D9.
$\lambda_{form} = 0.1786$	1.786×10^{-1}	8.93×10^{-2}	3.57×10^{-1}	7.144×10^{-1}	4.465×10^{-2}
$\lambda_{sim} = 1.428 \times 10^{-1}$	1.428×10^{-1}	7.144×10^{-1}	2×10^{-1}	7.142×10^{-1}	3.846×10^{-1}

MRUN-D10.	DRUN-13.	DRUN-B17.	DRUN-B18.	DRUN-C19.	DRUN-C20.	DRUN-D21.
$\lambda_{form} = 0.1786$	0.1786	1.786×10^{-2}	8.93×10^{-1}	3.57×10^{-1}	7.144×10^{-2}	3.85×10^{-1}
$\lambda_{sim} = 0.1428$	1.33×10^{-1}	1.428×10^{-1}	7.143×10^{-2}	7.143×10^{-2}	8.33×10^{-2}	4.5×10^{-2}